A MEASUREMENT OF THE ft-VALUE OF THE BETA DECAY OF O^{14}

Thesis by

R. Keith Bardin

In Partial Fulfillment of the Requirements

for the Degree of

Doctor of Philosophy

California Institute of Technology

Pasadena, California

1961

ABSTRACT

The Kellogg Radiation Laboratory 3.2-Mv electrostatic generator, 90° electrostatic analyzer, and 180° double-focusing magnetic spectrometer have been used to measure the Q-values of the reactions $C^{12}(He^{3}, p)N^{14*}$ (2.311-Mev state), $Q_p = 2468.4 \pm 1.0$ kev, and $C^{12}(He^{3}, n)O^{14}$, $Q_n = -1148.8 \pm 0.6$ kev, relative to the $Li^{7}(p, n)Be^{7}$ threshold energy at 1880.7 ± 0.4 kev (24). These measurements imply an end-point energy for the beta transition $O^{14}(\beta^{+}\nu)N^{14*}$ (2.311-Mev state) of $E_{max}(\beta^{+}) = 1812.6 \pm 1.4$ kev. The half-life of O^{14} has also been measured as $t = 71.00 \pm 0.13$ sec, which implies a partial half-life for the excited state transition of $t^{*} = 71.43 \pm 0.15$ sec. Averaged with the recent half-life measurement of Hendrie and Gerhart (37), the above data lead to an ft-value for the beta transition of ft = 3075 ± 10 sec, corrected for nuclear form factors, electron screening, and competition from K-electron capture (6). With the radiative corrections of Kinoshita and Sirlin (5), the value of the Fermi coupling constant for nuclear beta decay is then calculated from these data as $G_v = (1.4050 \pm 0.0022) \times 10^{-49}$ erg-cm^3, where the error is experimental only. The corresponding value calculated for muon decay is $G_\mu = (1.4312 \pm 0.0011) \times 10^{-49}$ erg-cm^3, differing by $(1.8 \pm 0.2)\%$. While some reservations are still necessary concerning the interpretation of the experimental results, it is felt that the origin of the discrepancy is probably theoretical in nature.

Descriptions are given of the equipment modifications required to achieve the accuracy demanded by the experiment, and an appendix

gives a detailed discussion of the theory of nuclear reaction yields from thick targets as observed by particle spectrometers with finite resolution in energy and angle.

ACKNOWLEDGMENTS

It is a pleasure for the author to acknowledge the contributions to this experiment of the entire staff and personnel of the Kellogg Radiation Laboratory. Of particular assistance were the valuable suggestions and criticisms of Professor Charles A. Barnes, who supervised the experiment from its inception, and of Professor William A. Fowler.

The author is also indebted to Professors Barnes and Fowler and to Mr. Philip A. Seeger for their large contributions of time and effort to the often demanding process of taking data, to Professors Hans A. Weidenmüller, R. F. Christy, and R. P. Feynman for many useful theoretical discussions, to Mr. Jack C. Overley for his collaboration in the rebuilding of the fluxmeter of the magnetic spectrometer, and to Barbara A. Zimmerman for her assistance in the calculation of the f-value. In addition, several stimulating conversations with Professors Ward Whaling and William A. Fowler contributed to the appendix on thick target yield theory, and the kind permission of Mr. James A. McCray to use his scattering data is acknowledged.

Finally, the author would like to express his appreciation for the financial support of Institute tuition scholarships from the beginning of the work. The experiment was supported in part by the joint program of the Office of Naval Research and the U. S. Atomic Energy Commission.

TABLE OF CONTENTS

I. INTRODUCTION

The experimentally observed near equality of the coupling constants in the nuclear beta decay and in muon decay has suggested the attractive idea that all of the so-called "weak interactions" proceed by a universal Fermi interaction (1). However, as the virtual states of the nucleon wherein it has emitted a charged pion would not be expected to undergo beta decay in the simple fashion of the usual theory, the fact that the existence of these virtual states does not produce a considerable reduction in the coupling constant for nuclear beta decay requires an explanation. This explanation is elegantly furnished by the conserved vector current hypothesis of Feynman and Gell-Mann (1, 2).

The proposal of this interesting hypothesis has stimulated further study of the electromagnetic and other small corrections to these decay processes (3-6), and raised considerable interest in establishing the exact degree of equality of the coupling constants G_V for the vector nuclear beta decay and G_μ for the muon decay when these corrections are taken into consideration. Recent measurements of the muon mean life (2.211 ± 0.003 μsec (7), 2.208 ± 0.004 μsec (8)) and muon mass (206.77 ± 0.01 m_e (9)) have considerably improved the precision of our knowledge of G_μ, making desirable a similar improvement in the value of G_V. Of the various experiments yielding a determination of this quantity, a determination of the ft-value of the $0^+ \rightarrow 0^+$ beta transition $O^{14}(\beta^+\nu)N^{14*}$ (2.311-Mev state) seemed the most satisfactory, both from the point of view of the state of the theoretical calculations (6) and because of its accessibility to the equipment

of this laboratory.

Due to the high order dependence of f on the end-point energy of the positron spectrum, and the experimental difficulty of a sufficiently accurate direct determination of this end-point (10, 11), it is desirable to make a somewhat more indirect measurement of the mass difference of O^{14} and N^{14*}, the parent and daughter states of the beta decay. Previous workers have determined this mass difference by measuring the neutron threshold for the reaction $C^{12}(He^3, n)O^{14}$, which gives the mass difference $O^{14} - C^{12}$ in terms of the relatively well known masses of the neutron and He^3 atom,† and combining this result with a determination of the mass difference $N^{14*} - C^{12}$ from various tabulated reaction cycles and mass doublets.

Bromley, et al. (12), have measured the neutron threshold as $E_{th} = 1449.6 \pm 2.8$ kev relative to the $Li^7(p, n)Be^7$ threshold assumed as 1881.6 ± 0.45 kev, which yields a Q-value for the $C^{12}(He^3, n)O^{14}$ reaction of -1158.5 ± 3 kev. Using adjusted Q-values and mass defects tabulated by Mattauch, et al. (13), for the $N^{14} - C^{12}$ mass difference, and the value of Bockelman, et al. (14), for the N^{14*} excitation (2313 ± 5 kev), they calculated $E_{max}(\beta^+) = 1809.7 \pm 7.8$ kev.

The group at the Naval Research Laboratory have obtained threshold values $E_{th} = 1435 \pm 5$ kev (15) and $E_{th} = 1436.2 \pm 0.9$ kev (16,17). The first of these measurements was taken with a 90^o magnetic analyzer calibrated with the $Li^7(p, n)Be^7$ threshold at 1881.1 kev, while the second is an absolute measurement with the NRL 2-meter electrostatic analyzer. Bondelid, et al. (16), combined their Q-value for the

†See, however, the discussion of the He^3 mass below.

$C^{12}(He^3, n)O^{14}$ reaction with values from the tables of Mattauch, et al. (13), and the value 2312 ± 1.2 kev for the excitation of N^{14*} taken from Ajzenberg-Selove and Lauritsen (18) to get $E_{max}(\beta^+)$ = 1800.0 ± 1.2 kev. Since the publication of the preliminary report (19) on the work described in this thesis, Butler and Bondelid (17) have re-analyzed their data using masses from the tables of Everling, et al. (20), which are in much better agreement with the measured Q-values from the present experiment. Their new value of the positron end-point energy is $E_{max}(\beta^+)$ = 1809.7 ± 1.5 kev.

II. CHOICE OF EXPERIMENT

A comparison of the 1960 atomic mass tables (20) with the 1956 tables (13) shows disturbingly large changes in masses important for this experiment. The mass excess of He^3 changed from 15.8144 ± 0.0042 Mev (13) to 15.8190 ± 0.0002 Mev (20) ($O^{16} = 0$), an increase of 4.6 kev. The calculated Q-value for the reaction $C^{12}(He^3, p)N^{14}$ changed by 10.8 kev from 4.7678 Mev (13) to 4.7786 Mev (20). Considering in addition the poor agreement of the various measurements of the $C^{12}(He^3, n)O^{14}$ threshold energy (12, 15-17), we decided to reduce as much as possible the dependence of the positron end-point energy on subsidiary measurements by measuring the mass difference of O^{14} and N^{14*} directly in the reactions,

$$C^{12} + He^3 \rightarrow O^{14} + n + Q_n \qquad (1)$$

$$C^{12} + He^3 \rightarrow N^{14*} + H^1 + Q_p \qquad (2)$$

so that the only masses that need be known to better than kilovolt accuracies are those of the hydrogen atom, the neutron, and the electron:

$$\begin{aligned} E_{max}(\beta^+) &= (O^{14} - N^{14*})c^2 - 2m_e c^2 \\ &= Q_p - Q_n + (H^1 - n)c^2 - 2m_e c^2 \qquad (3) \\ &= Q_p - Q_n - 1804.6 \pm 0.5 \text{ kev} \end{aligned}$$

Here we have used only the hydrogen atom-neutron mass difference from the tables (20) and the electron mass (21). (The errors quoted are standard deviations, here and in all results from this laboratory quoted below.) It should be noted that the value used, $(n - H^1)c^2 = 782.61 \pm 0.40$ kev, has recently been confirmed by the NRL group,

who get 782.9 ± 0.4 kev on the basis of an absolute measurement of the $T^3(p,n)He^3$ threshold energy (22).

To complete the ft-value measurement, it was desired to check the value given by Gerhart (10) for the half-life of O^{14} ($t = 72.1 \pm 0.4$ sec) with smaller error if possible. The value given by Sherr, et al. (23), for the ground state branch of decay (0.60 ± 0.10%) would have required a considerable additional experimental effort to attain any reduction in error; in any case, its contribution to the ft-value is rather small.

The primary energy calibration for the experiment was chosen as the $Li^7(p,n)Be^7$ threshold, assumed at 1880.7 ± 0.4 kev, in accord with the recent recommendation of Marion (24).

III. EXPERIMENTAL ARRANGEMENT

The experiment was carried out using the Kellogg Radiation Laboratory 3.2-Mv electrostatic accelerator, 90^{o} electrostatic analyzer, and 16-inch-radius double-focusing magnetic spectrometer, with modifications to accessory equipment to provide extra accuracy and flexibility. The electrostatic analyzer is that described by Fowler, Lauritsen, and Lauritsen (25), with modifications of power supply and control circuits to extend its range for operation with the 3.2-Mv accelerator; the magnetic spectrometer is described in the thesis of C. W. Li (26).

As will become evident, this experiment was greatly facilitated by the availability of a gas supply system capable of rapid changes of ion source gas. This system, making possible a selection of H, D, He^3, or He^4 beams, was installed in the terminal of the 3.2-Mv generator in 1957, when the availability of He^3 first stimulated consideration of a series of experiments using it as the bombarding particle. The system is constructed around a four-way selector valve with minimal internal volume and a differential-screw-actuated needle valve, both developed by Mr. V. F. Ehrgott from preliminary designs by Prof. C. C. Lauritsen. The system is outlined in figs. 1, 2 and 3. A vacuum line from the top of the accelerating tube removes any small amount of gas leaking past the O-rings of the selector valve, thus eliminating a possible source of contamination of the gas supplies, and at the same time serves as a convenient means of disposal for the gas which necessarily remains in the small-bore tubing leading to the needle

valve when one wishes to change gases. The bell jar over the He^3 bottle was added after the failure of a -30 in. to 15 psig Bourdon gauge on this bottle due to the external pressure of the generator insulating gas. A recovery system for the He^3 was not considered necessary at the \$1.50/cc price then prevailing, and is even less important at the present rate of \$0.15/cc; gas consumption makes a negligible contribution to running costs.

The electrostatic analyzer used in this experiment is an old one, originally constructed for use with the 2-Mv electrostatic generator (25), and required a number of changes to bring it up to the accuracy and reproducibility required by this experiment. It was found that over the years the analyzer suspension system had accumulated additional constraining adjustments until the analyzer was both overconstrained and coupled to the position of the magnetic analyzer which is mounted immediately below it. This arrangement is designed to allow a second experimental station to make use of the beam passing undeflected through a gate in the lower deflection plate. The undesired restraints were removed by rebuilding the electrostatic analyzer suspension, and a somewhat improved system of beam-defining slits was installed. The mass-separating magnet at the exit of the accelerating tube of the generator was replaced because of its tendency to overheat badly when used to deflect high-energy He^{4+} beams, and a transistorized power supply and regulator were built for it.

As the beam in this accelerator shows a tendency to wander with time and ion source conditions, it has been necessary in the past to move the electrostatic analyzer to follow the beam when operating with the

analyzer entrance slits stopped down. This frequently resulted in upsetting the analyzer energy calibration in a most inconvenient fashion. An attempt to stabilize the beam position was therefore made by installing an electrostatic deflection system immediately below the base of the accelerating tube of the generator. The electron loading produced by the presence of this system so close to the main accelerating field in the tube, however, reduced the maximum voltage attainable by the generator by an intolerable amount. It was therefore removed for redesign, and during the period of its absence, sufficient experience was gained in the use of the adjustments to the electrostatic analyzer suspension to enable us to successfully translate the analyzer as a whole to follow a fluctuation in beam position while maintaining the energy calibration quite closely. This was materially aided by the installation of a dial indicator to assist in maintaining a constant entrance angle of the beam.

The measuring voltage divider for the analyzer deflecting voltage is composed of two 37-megohm stacks made up of 1-megohm 1/2% hermetically sealed non-inductively wirewound resistors made by the Westinghouse Electric Corporation about 1941. While searching for the sources of the instabilities in calibration of the electrostatic analyzer which remained at this time, we were led to check these two stacks in a bridge circuit against a stack of spare resistors of the same type. A considerable portion of the earlier erratic behavior of the electrostatic analyzer was traced to resistors with shorted or partially open turns. Replacement of these resistors gave much more reproducible results. The 1-kilohm tap resistors at the bottoms of the two stacks (see fig. 4)

were also changed from 1% deposited carbon resistors to 1% low temperature-coefficient wirewound resistors for reasons of temperature stability.

In investigating a small apparent bistability in the analyzer power supply, we discovered that the regulator amplifier was oscillating at about 20 kc over a large part of its output range. This was eliminated by the installation of plate decoupling filters, grid damping resistors, and shielded cable for the long grid lines in the amplifier. It was also found that the amplifier was being held in saturation most of the time by 60-cycle hum pickup coming through the input filters. This was traced to capacitive pickup of the waveform put out by the high voltage transformer, which has the characteristic square shape of the output of the Sola regulating transformer from which the whole system is run. This waveform appeared in differentiated form on the lower end of the regulator feedback voltage-divider resistors and the leads to the amplifier input (see fig. 4). The installation of shielded input leads and electrostatic shields around the divider stacks removed the difficulty and resulted in a much higher effective amplifier gain and much tighter control over the analyzer plate voltage. There are indications, however, that the control system, although quite serviceable, now has an undesirable amount of overshoot and ringing, and it is recommended that an investigation be made of suitable networks to correct this.

A sizeable and rather erratic interaction of the electrostatic analyzer with the three large magnets near it, which produce highly nonuniform stray fields of the order of 5 gauss, led us to install two

layers of sheet steel over the brass analyzer tube as magnetic shielding. This not only eliminated the interaction, but gave an unexpected dividend in the shape of a spectacular improvement in the stability and beam-handling capabilities of the analyzer, apparently by making the beam orbits much more nearly circular between the deflection plates. This results in greatly reduced electron loading of the plates due to secondary emission from stray beam.

Further modifications to the electrostatic analyzer and incident beam-handling equipment were the transfer of the main beam-control shutter from between the two pairs of regulator pickoff slits on the exit of the analyzer to beyond the second pair, thus eliminating a starting transient due to the shift of control of the accelerator voltage to the final slits at the start of a run, and the installation of a heat-exchanger system to stabilize the temperature in the box which contains both the main analyzer power supply and the measuring voltage dividers in rather undesirable proximity. With the completion of these modifications, the $Li^7(p,n)Be^7$ threshold was found to be reproducible to better than 1 part in 8000.

The changes required in the magnetic spectrometer were confined entirely to its fluxmeter. This fluxmeter, because of the requirement of measuring some reasonably suitable average of a nonuniform field, is a horizontal-axis current-balance type with its coil approximately centered on the midpoint of the central ray of the spectrometer (see fig. 5). It was found to be subject to sudden shifts of as much as 1% in calibration constant. These shifts were attributed to changes in the position of the point of rotation in the inverted cone bearings used, due

to the effects of any slight jar, such as bouncing the fluxmeter balance rod against its stops or accidentally brushing against the housing of the fluxmeter. It was therefore rebuilt as described in Appendix A, using modified point-on-plane bearings which are not subject to change in effective moment arm with position of the point of rotation (see fig. 6). Not only are these bearings not subject to the previous sensitivity to shock, but an occasional tendency to stick on their restraints is customarily cured by a sharp rap with a screwdriver handle on the side of the fluxmeter housing, without apparent effect on the calibration.

It was also found that the thin aluminum coil form originally used was slightly magnetic, producing a variation in the sensitivity of the instrument with the magnetic field and an unknown effect on the calibration. This was therefore replaced with a lucite coil form with copper damping rings.

Also described in Appendix A are a photoelectric indicator circuit of improved sensitivity and stability, an improved fluxmeter coil current supply, and a modified Kelvin bridge resistance thermometer to measure the coil temperature. This last circuit was used in an attempt to measure the temperature coefficient of the calibration constant, but the thermal behavior of the system was too complex to yield any clearcut result.

A. $C^{12}(He^3, p)N^{14*}$ (2.311-Mev state)

The experimental arrangement for this part of the experiment was chosen on the basis of considerations of reaction yield and of the questionable linearity of double-focusing magnetic spectrometers in

comparison with electrostatic analyzers. The low yield of the proton reaction at the threshold for neutron production was felt to rule out the attractive idea of measuring both reactions at the same energy of bombardment. It therefore seemed advisable to look for a scheme which would permit the calibration of the magnetic spectrometer at the field setting and observation angle actually to be used in the reaction energy measurement, thus eliminating the effects of the known spectrometer nonlinearity (26), but with the restriction that the reaction yield at the selected bombarding energy and observation angle should be both reasonable in size and have reasonably small derivatives in energy and angle. This last restriction is necessary to avoid a complicated and rather difficult analysis of the profile shape of the reaction proton yield vs. bombarding energy (see Appendix B). As the angular resolution $\Delta\theta$ of the spectrometer contributes to the width of the rise of the profile in proportion to $(\partial E_2/\partial\theta)\Delta\theta$, where E_2 is the emerging proton energy, the precision with which one can locate the rise is also improved by doing the measurement at an angle as far from 90° in the laboratory as possible, as $\partial E_2/\partial\theta$ has its maximum at that angle (27).

A plot was therefore constructed of the effective energy of the emerging particle as referred to protons in the magnetic spectrometer, $E_{2eff} = M_2E_2/Z_2^2M_p$, vs. bombarding energy and observation angle, E_1 and θ, for various elastic scattering processes on the same axes as a similar plot for the $C^{12}(He^3,p)N^{14*}$ reaction (fig. 7). An inspection of this plot produced the scheme finally used.

After the equipment had warmed for several hours to allow an approach to thermal equilibrium, especially in the magnetic spectro-

meter, the first operation was to calibrate the electrostatic analyzer at the 1880.7-kev $Li^7(p,n)Be^7$ threshold with the proton beam. With the ion source gas switched to D_2, the magnetic spectrometer, which had been allowed to stabilize at the approximate equivalent proton energy of 3.63 Mev and an angle of 150^o in the laboratory, was then calibrated precisely by doing $Au^{197}(d,d)Au^{197}$ elastic scattering from thick gold targets evaporated onto glass or polished quartz. During this calibration the magnetic spectrometer field was held fixed and the electrostatic analyzer setting was varied to find the thick target step, which occurred within a very few kilovolts of the primary calibration point at 1880.7 kev, making the spectrometer calibration essentially independent of analyzer linearity.

Then, with the magnetic spectrometer entirely undisturbed in both magnetic field and angle, we ran the $C^{12}(He^3,p)N^{14*}$ reaction, taking a profile with the electrostatic analyzer near a bombarding energy of 2.69 Mev. To minimize the effects of long-period drifts on the result, the $Au^{197}(d,d)Au^{197}$ and the $Li^7(p,n)Be^7$ calibrations were then repeated in opposite order.

The detector used for the protons at the focus of the magnetic spectrometer was a 0.003-in-thick CsI scintillator mounted on a Dumont 6291 photomultiplier tube. Conventional amplifier and scaler arrangements with an integral discriminator permitted the rejection of the relatively small pulses produced by elastically scattered He^3.

In the $Li^7(p,n)Be^7$ calibration, the detector used was a 2-inch-diameter 92%-enriched B^{10}-plastic ZnS(Ag) scintillator, Nuclear Enterprises, Ltd., Type NE402, mounted by means of a 1/4-inch-thick

conical Lucite light pipe to a 1-1/2-inch Dumont 6291 photomultiplier tube and surrounded by polyethylene moderator. The geometry of the scintillator assembly is shown in fig. 8, and its characteristics are discussed in Part III. D below.

The C targets used for this part of the experiment were polished pieces of graphite spectroscopic electrodes during the earlier runs, and thick films of carbon cracked from a methyl iodide atmosphere for the later runs. The cracked films were substituted for the graphite to eliminate small irregularities in the thick target reaction profile believed to be due to the irregularities in the surface of the graphite. They proved to be quite satisfactory targets, aside from a slight tendency to peel, provided they were thoroughly out-gassed by heating in a vacuum after the cracking process; failure to do so resulted in targets that would emit large quantities of positive ions under the action of the beam for the first few minutes of bombardment on a given spot, giving a strong negative indication on the target current integrator.

The targets used for the $Li^7(p,n)Be^7$ calibration were relatively thick layers of LiF evaporated onto tantalum strips. The excellent gamma-ray rejection of the B^{10} plastic scintillator permitted the use of these targets with essentially zero background below threshold despite the strong flux of gamma rays from $F^{19}(p,\alpha\gamma)O^{16}$ reactions. The largest source of background was believed to be (d, n) reactions from residual deuterium in the accelerator.

Figure 9 shows the overall arrangement of target chamber and detectors for this part of the experiment. The auxiliary, off-axis target rod shown was installed to hold the LiF targets for calibration of the electrostatic analyzer.

B. $C^{12}(He^3, n)O^{14}(\beta^+\nu)N^{14*}(\gamma)N^{14}$

The experimental arrangement for this section of the experiment was chosen almost entirely for reasons of background reduction. As there are almost always two or more experiments going on in rotation during the same period on different experimental stations on the accelerator, neutron background from residual deuterium in the ion source is nearly always a problem. We therefore chose to observe the delayed 2.311-Mev N^{14} gamma radiation following the beta decay of the O^{14} produced in the reaction (see fig. 10). This procedure allows all counting to be done with the generator voltage off, thereby eliminating all generator-associated background, and permits strong discrimination against the longer-half-life positron emitters, C^{11} and N^{13}, which emit no nuclear gamma rays. These two nuclides are produced quite liberally in the reactions $C^{12}(He^3, He^4)C^{11}$, and $C^{12}(d, n)N^{13}$, respectively, the deuterons coming from the small HD^+ contamination in the He^{3+} beam. Discrimination against these undesired activities is of course not possible if one observes either the positrons directly or the resulting annihilation radiation. Another feature of observing the N^{14} gamma ray is that one obtains an excellent determination of the residual background by merely following the 71-sec O^{14} decay for a sufficiently long time.

The arrangement of the apparatus is shown in fig. 11. The target, either deposited carbon film or polished graphite, was placed in a tee-shaped glass target chamber at the end of the extension tube as shown. A 4-inch NaI(Tl) scintillator mounted on a 5-inch Dumont 6364 photo-

multiplier tube was surrounded by a 2-inch lead shield and a thick boric-acid-loaded plastic neutron shield. This assembly was placed with the face of the crystal about 3/4 inch from the center-line of the target, usually at about 80° in the laboratory, and the whole front, including the target chamber, shielded with about two inches of lead.

For the $Li^{7}(p, n)Be^{7}$ calibration, the 4-inch scintillator and its shielding assembly, which is mounted on a wheeled cart, were rolled behind a heavy concrete wall to minimize neutron activation of the crystal, and the B^{10} neutron scintillator and moderator assembly described above was placed with the face of the moderator essentially in contact with the target chamber and centered along the beam axis (see fig. 12). Calibration runs were made, as usual, both before and after each threshold run.

A block diagram of the circuitry used for the O^{14} threshold is shown in fig. 13. Amplified pulses from the photomultiplier were fed to a single-channel differential discriminator which was set to bracket the photo-peak of the 2.31-Mev radiation. The settings of the amplifier gains and the discriminator levels were chosen by observing the relative positions of the 2.31-Mev photo-peak and the output of a pulse generator set at the discriminator window edges on the 100-channel pulse-height analyzer. Checks for drift were made at intervals. The counts from the discriminator output were switched between two alternate scalers by a mechanical timer at 20-sec intervals beginning 4 sec after the end of an activation, which permitted the recording of the counts in one scaler while the other was counting. Timing was

checked throughout by counting 120 cps derived from the power lines in secondary channels in the two scalers which were gated in synchronism with the counting periods. Uniform activation of the target approximately independent of beam current or bombardment time was obtained by connecting a resistor across the integration capacitor in the target current integrator to give a 72-sec half-period, which was the best figure then available for the O^{14} half-life. An effort was also made to keep the bombarding current reasonably uniform.

A measurement of the dead time of the scalers used in this experiment was made in the usual fashion, comparing the counting rates, C_1 and C_2, for two ThC" sources separately with C_T, the counting rate for the two simultaneously. The dead time is then $t \cong (C_1 + C_2 - C_T)/2C_1C_2$, for small percent dead time. The result of the measurement was very close to $10\,\mu$sec for both scalers, which was entirely negligible for the counting rates used, about 20 counts/sec maximum, but resulted in a significant correction when these scalers were used for preliminary measurements of the O^{14} half-life.

C. O^{14} Half-life

In the determination of the O^{14} half-life, the considerations discussed above in connection with the $C^{12}(He^3, n)O^{14}$ threshold apply with even greater force, as here it becomes essential that one be able to follow the 71-sec decay for several half-lives with minimum interference from longer-lived background and other sources of distortion of the counting rate curve. For this reason a similar type of experi-

mental arrangement was used. The energy of bombardment was chosen at about 1800 kev to give adequate yield and a reasonable ratio of the $C^{12}(He^3, n)O^{14}$ cross section to the much larger and more rapidly rising cross section† for $C^{12}(He^3, He^4)C^{11}$. To achieve maximum O^{14} yield relative to competing reactions, the bombarding time was chosen as 100 sec, approximately equal to the mean life. The beam current was the highest value consistent with holding to reasonable levels the loss of O^{14} from the target by overheating or sputtering of the graphite; this value was about 5 μA, which also seemed to represent a practical maximum for beam current through the electrostatic analyzer, at least at the slit apertures used.

To prevent activation of the NaI crystal by the rather considerable neutron flux produced during a bombardment, the scintillation counter was set up in an adjoining room on the other side of a heavy concrete wall. Polished graphite button targets were activated by He^3 bombardment on the central target rod of the main target chamber (see fig. 9), and then removed and placed in a sealed brass capsule for counting to prevent loss of O^{14} during the counting period. The length of time required to let the target chamber down to atmospheric pressure and transfer the source to its position in front of the counter averaged about one minute. A number of targets were used in rotation to allow time for the background of 10-min N^{13} and 20-min C^{11} to decay between runs with the same target.

---

†An exploratory run at about 3.0 Mev produced sufficient positron activity to completely swamp any trace of 2.3-Mev gamma radiation; on the basis of crude estimates of the yield and half-life involved, C^{11} was the most probable source of the activity.

A 3 x 3-inch NaI(Tl) scintillation crystal and photomultiplier assembly made by the Harshaw Chemical Co. was used for this experiment, with shielding very similar to that used in the O^{14} threshold measurements; the only essential difference was that various thicknesses of lead were inserted as an absorber between source and crystal to attenuate the strong 511-kev annihilation-radiation peak. Without this precaution, it was found that the high counting rate for this radiation produced a shift in the gain of the photomultiplier as it decayed over the 20-min length of a run, and also raised the problem of superposed "build-up" pulses in the amplifier and discriminator. Absorber thicknesses of 1 cm and 2 cm were both used, and both were found to be effective; the resulting half-life curves were indistinguishable.

Because of the high initial counting rates involved in this experiment, precautions were necessary to minimize the dead time of the counting system (shown schematically in fig. 14). For this reason, a Fairstein double-delay-line-clipped non-overloading amplifier was used, fed from 93-ohm RG-62/U cable driven by a White cathode follower at the photomultiplier. The output from the internal differential discriminator of the amplifier was used to drive both channels of a fast dual scale of eight. The outputs of the scales of eight were fed to separate scalers of the ordinary variety.

The linear output of the amplifier was also fed to an oscilloscope and, by way of 42 feet of RG-65/U delay cable, to the signal input of the 100-channel analyzer, which could be gated either internally or by the output of the discriminator. This arrangement permitted

examination of the pulse height spectrum of the amplifier output either in toto or in coincidence with those pulses which were actually counted. It was used to set the amplifier gain and discriminator levels, and to monitor the relationship between the photo-peak of the 2.31-Mev radiation and the discriminator levels during the entire course of a run.

The timing for the experiment was provided by gating the two channels of the fast scaler alternately every 20 sec with the mechanical timer described above. Two additional scalers, also gated alternately by the timer, were used as the time monitor by feeding them with the 10-kc output of a multivibrator frequency divider synchronized with a 100-kc quartz crystal oscillator. This oscillator had been checked by comparison with the average of the power line frequency over a number of days.

The dead time of this arrangement was checked with a double pulse generator and by observation of the waveforms put out by the discriminator and amplifier when fed by an intense source; by either method, it was found to be very close to the 2-μsec length of the delay-line-clipped output of the amplifier. The dead time of the fast scalers was less than 1 μsec and did not contribute to the overall dead time of the system. The resultant corrections to the initial counting rate from this source were always less than 1%, and usually of the order of 0.3%.

D. Equipment Check and Calibration Experiments

As the magnetic spectrometer was known to have calibration non-linearities of the order of 1% over its 10-Mev proton range (26), the experimental arrangements were chosen so that it was used only as a null

instrument, with fixed field. However, both the proton reaction and the neutron threshold Q-values depend on the linearity of the electrostatic analyzer in its extrapolation from the 1880.7-kev calibration point to the bombarding energy actually used. An experiment to check the linearity of the analyzer was therefore necessary, particularly as the resistors of the voltage measuring dividers were known to have a positive temperature coefficient, crudely measured as +40 ppm/^{o}C, and the local temperature rise of the resistive elements was not known.

The resistors used in these dividers were designed about 1941, and fall short of the ideal in a number of respects. As mentioned above, they are prone to develop shorted and open turns as a result of the voltage surges to which they are occasionally subjected when the analyzer sparks. In addition to this, they combine a temperature coefficient which is not particularly good by more recent standards with excellent thermal isolation of the resistive element from the ambient air due to their heavy hermetically sealed construction; even the addition of copper fins proved unsuccessful in improving the cooling of the divider stacks. The relatively high internal temperatures resulting from this construction presumably also make their contribution to mechanical deterioration of the insulation and conductors after many temperature cycles. It is therefore recommended that, when these resistors are replaced (hopefully in the near future), the specification be written to include a five-times voltage overload surge test, such as a 1/2-sec capacitor discharge, in addition to the usual specifications of good modern precision resistor design, such as "relaxed winding" techniques and a wire alloy having low temperature and voltage coefficients and

small thermal e. m. f. to copper. When coupled with the use of a capacitive surge-voltage divider network in parallel with the resistor stack, the additional overload specification should eliminate surge failure.

The experiment to check the linearity of the analyzer was based on the comparison of the analyzer voltage settings for bombardment with H^+ and HH^+ beams at three resonances in the $Al^{27}(p, \gamma)Si^{28}$ reaction. Gamma rays from aluminum leaf targets of thickness about 0. 2 mg/cm^2 were observed with a 4 x 4-inch NaI scintillator and photomultiplier feeding an amplifier and integral discriminator. The Al leaf was thick enough to provide a thick-target yield curve without unnecessarily increasing the background due to the integrated yield of lower resonances. After correction for the energy of the extra electron in the HH^+ ion, the theoretical ratio of the energies of the H^+ and HH^+ beams was compared with the ratio of the settings of the electrostatic-analyzer measuring potentiometer for the midpoints of the thick-target steps for the two beams.

The use of this comparison to arrive at an estimate of analyzer nonlinearity is, however, open to question on at least two points. The first and least serious of these is the considerable width of the yield step produced by the HH^+ beam, which results in an undesirable reduction in accuracy. This width is evident in the typical experimental profiles shown in fig. 15. The smearing out of the profile is apparently associated with the nature of the HH^+ ion, and has generally been attributed to the effects of the internal motion of the ion (28).

A more serious objection is that recent workers (29-31) investigating various $Al^{27}(p, \gamma)Si^{28}$ resonances with H^+, HH^+, and HHH^+ beams have found nonlinearities which may be characteristic of the molecular ions themselves. Bondelid, et al. (29), ascribe the effect tentatively to the possible existence of the HH^+ ion as a unit for a short distance inside the target, corresponding to an energy loss of some 0.5 kev or so, resulting in increased yield at the base of the rise in the profile as a result of the decreased stopping power per proton of the ion before dissociation. They also find that the discrepancy in the apparent position of the resonance disappears when a thin target is used, which strongly supports the assumption that the difficulty is due to some poorly understood interaction of the molecular ion with a thick target.

Anderson, et al. (30), working at lower energies and with thick targets only, find that the discrepancy increases rapidly with energy. However, they prefer to ascribe the effect to some unknown nonlinearity in their electrostatic analyzer, perhaps the charging of a thin insulating layer on the surface of the deflecting plates.

In a very recent experiment, Dahl, et al. (31), have obtained profiles which they have succeeded in fitting in considerable detail by using a model in which the electron in the ion is stripped away by the initial impact on the target, whereupon the Coulomb forces between the two protons remaining produce an increasing velocity spread of the beam as it penetrates the target more deeply.

The available data on the discrepancy in HH^+ resonance position

has been collected in fig. 16, which shows the difference ΔE between the theoretically predicted position of the HH^+ step and the experimentally observed position, plotted versus the proton resonance energy E. The points shown as triangles are those taken during the course of the present experiment. The slope of the line drawn on the log-log plot corresponds to proportionality to E^2. The fit of the line to the points is probably fortuitously good. The E^2 dependence of the effect is not understood, as a simple estimation of the energy differences produced in the Coulomb "explosion" of the ion would predict a proportionality to $(E_c E)^{1/2}$, where E_c is the available Coulomb energy of separation and E is the beam energy.

To return to the question of what, if any, correction is necessary to the electrostatic-analyzer linearity in the present experiment, one must conclude that if the fit in fig. 16 is in fact meaningful, the observed nonlinearity is entirely due to the molecular-ion effect to the accuracy of the measurements, and therefore no correction is required. One may, on the other hand, conclude with Anderson, et al. (30), that the effect is in the electrostatic analyzer rather than the molecular ion. This presumption was in fact applied to the values quoted in the preliminary report (19) on this experiment, resulting in corrections to the final Q-values of -1.3 kev and +0.4 kev for Q_p and Q_n, respectively.

On the basis of the consistency of the trend in energy of the measurements taken with this analyzer combined with measurements from several different laboratories, the assumption that the molecular-ion effect is real and produces a nonlinearity as shown in fig. 16 will be

used in the calculations following. Therefore no correction was applied to measurements taken after the completion of the improvements to the electrostatic analyzer described above. Data taken on the HH^+ resonances of the $Al^{27}(p,\gamma)Si^{28}$ reaction before the installation of the heat exchanger in the power-supply box, however, do indicate the presence of an additional effect. When the molecular-ion effect is subtracted out, the remaining behavior is strongly suggestive of a thermal effect with a time constant of the order of hours. An estimate of the magnitude of this remaining nonlinearity was made based on the assumption that it was a thermal drift due to resistive V^2/R heating of the voltage-divider stacks, which leads to the form used for this correction in Appendix C. This resulted in a correction applied to the part of the data for Q_p which was taken before the heat-exchanger installation, amounting to -0.7 ± 0.8 kev in terms of Q_p, where the standard deviation is derived from the dispersion of the measurements of this residual correction. The standard deviation of the measurements of the HH^+ $Al^{27}(p,\gamma)Si^{28}$ resonances after the installation of the heat exchanger contributed ± 0.16 kev to the uncertainty of the remaining data for Q_p, and ± 0.07 kev to the data for Q_n. In addition to the errors above due to the uncertainties in the measurements of the resonance positions, a standard deviation of ± 0.2 kev/Mev^2 was arbitrarily assigned to the coefficient of E^2 in the molecular-ion effect, i.e., to the position of the line shown in fig. 16. This contributed ± 0.28 kev and ± 0.09 kev to the standard deviations of Q_p and Q_n, respectively.

The presence of these experimental and theoretical uncertainties make an alternative method of checking electrostatic-analyzer linearity

desirable. One possible alternative would be the comparison of He^{+} and He^{++} beams in the analyzer. There are a number of ways to do this. One of the simplest would be to insert a gas or carbon-foil stripper in the He^{+} beam above the mass-separating magnet, and use the magnetic spectrometer as a null instrument to examine elastically scattered particles of fixed momentum from a heavy scattering target. The only parameters varied in the comparison would be the electrostatic-analyzer voltage and the mass-separating magnet current. As molecular ions are not involved, the resulting profiles should be sharp and free of both difficulties discussed above. The high yields should permit readings rapid enough to minimize the effects of spectrometer drift, as well as eliminating background problems.

As described above, the neutron detector used for the $Li^{7}(p, n)Be^{7}$ calibration was a 92%-enriched B^{10}-plastic ZnS(Ag) scintillator. This detector is somewhat similar to those described by Sun, et al. (32), but the use of enriched B^{10} permits a somewhat thinner scintillator with higher efficiency and better gamma-ray rejection. As was remarked, thick LiF targets were used for the $Li^{7}(p, n)Be^{7}$ threshold measurements, commonly yielding 20,000 counts at 10 kev above threshold and less than 1 count average background below threshold, despite the very considerable gamma flux from $F^{19}(p,\alpha\gamma)O^{16}$ processes.

The recommended procedure for neutron threshold experiments (24) requires the extrapolation to zero of the 2/3 power of the total neutron yield above background. This is intended to linearize the expected 3/2 power dependence on energy above threshold of the thick-target yield for an s-wave neutron threshold. As center-of-mass motion

projects the neutrons into a narrow cone in the forward direction immediately above threshold, one can perform the experiment using a single counter in the forward direction, provided the solid angle of reasonably constant sensitivity subtended at the target by the counter is large enough to accept all neutrons for a sufficient range of energies above threshold before the neutron cone expands beyond the sensitive angle, destroying the 3/2 power relationship. A large value for this sensitive angle is therefore highly desirable in a counter to be used for precision work.

To take full advantage of the capabilities of the neutron scintillator, the moderator and photomultiplier assembly were designed as shown in fig. 8 to fit inside the 6-inch continuously-variable-angle target chamber, thus giving the maximum possible solid angle of sensitivity. As the body of the target chamber is attached to the rotating frame of the magnetic spectrometer, it was possible to measure the angular sensitivity of the array by moving the spectrometer away from the 90° position in which it normally remains while using this arrangement. A LiF target on the central target rod was bombarded with a proton beam of energy approximately 0.7 kev above the threshold, at which energy the half-width of the emergent cone of neutrons is calculated to be about 8°. Moving the detector through this relatively narrow beam, we found that the counting rate held approximately constant until the axis of the detector was 50° from the beam axis, falling to about half its central value at 60°. As this experiment was carried out before the improvements to the electrostatic analyzer were com-

pleted, instabilities in the beam energy prevented anything more than a rough estimate of the constancy of the yield, but, since a neutron cone angle of 50° for the $Li^{7}(p, n)Be^{7}$ threshold corresponds to an energy of 22 kev above threshold, the available solid angle is evidently quite adequate in size.

The excellent linearity of 2/3 power plots of the yield for the first 4 or 5 kev (see fig. 17) is apparently fortuitous, however, as a calculation based on the results of detailed investigations of the threshold (33, 34) predicts that this plot should fall 30% below linear at 5 kev above the threshold. It is possible that a compensating increase in detector sensitivity with increasing energy above threshold could be produced by the following mechanism in this region. As is well known, the fraction of the neutrons which is emitted in the backward direction in the center-of-mass system decreases in energy with increasing bombarding energy in the laboratory system for a short interval immediately above threshold. In view of the rather thin (5/8-inch) polyethylene moderator in front of the scintillator and the 1/v cross section of the B^{10}, this reduction in energy could easily result in a higher detection efficiency for this component of the neutron yield. It is also possible that the sensitivity of the detector with angle could contribute to the effect, but as the half-angle of the neutron cone is only a little over 20° at 5 kev above the threshold, this effect, while not excluded by the measurements above, is believed to be small. In any case, as is evident from fig. 17, the effect of such variations in shape on the extrapolation of the yield curve to the threshold is very small.

Figure 17 also shows a comparison of the profiles resulting from the $Li^7(p, n)Be^7$ threshold measurement in each of the three different geometries (see figs. 8, 9, and 12) in which this detector was used. The close similarity of shape is taken as an indication of the reliability of the assumption that linearly extrapolated intercepts yield the same absolute calibration in each configuration; the relation of the absolute calibration to the readings on the electrostatic-analyzer measuring potentiometer is of course a function of the particular conditions of analyzer alignment prevailing.

As is shown in Appendix C, the Q-value for the $C^{12}(He^3, p)N^{14*}$ reaction is quite sensitive to the value of the angle of observation; calculation shows that $\partial Q_p/\partial\theta = 6.0$ kev/degree. It is therefore important that the angular position of the magnetic spectrometer relative to the beam axis be accurately known. To determine this angle, at the end of each series of runs of the proton reaction, before any disturbance whatever of analyzer or spectrometer settings was permitted, the experimental arrangement shown in fig. 18 was used to measure directly the angle between the entering beam and the centroid of the solid angle of acceptance of the magnetic spectrometer. Using a thick target of evaporated gold, we obtained the yield of elastically scattered protons as a function of the position of a 0.040-inch vertical slit mask on the end of a 2.00-inch radius arm as the mask was swept across both the beam and the spectrometer aperture, the target position being held fixed. The position of the mask was read on the vernier protractor shown, which could be set to considerably better than 0.1°. A

plot of the resulting yield vs. mask angle is given in fig. 19 for both $Au^{197}(p, p)Au^{197}$ scattering and also for $Au^{197}(He^{4+}, He^{4++})Au^{197}$ scattering with a bombarding energy of 1.90 Mev and the same laboratory angle of approximately 150°.

The angles of the centroids of the yield distributions across the beam and across the spectrometer aperture were then calculated, and their difference taken as the actual angle of observation in the laboratory. The He^4 scattering, as it involves incoming and outgoing particles of widely differing magnetic rigidity, was used here to help estimate the effects of stray magnetic fields from the spectrometer on the entrance and exit angles. By subtracting the proton results and the He^4 results, the entrance angles were found to differ by 0.06°, the exit angles by 0.04°, and their difference, θ_{lab}, by 0.03°. These results were also felt to give an indication of the reproducibility of the technique of measuring the angle.

Three additional effects on this measurement must also be considered. The first of these is the variation of the Rutherford scattering yield across the $3\text{-}1/2^{\circ}$-wide aperture of the spectrometer, which produces a small systematic shift in the location of the centroid of the yield distribution. This variation is calculated to be of the order of 0.007 per degree, producing a shift in centroid of the order of 0.007°, and is therefore negligible. The second possible error in the measurement is due to failure of the beam to intersect the axis of rotation of the mask. However, as shown in fig. 20(a), this error vanishes in first order since the target normal was set to bisect the angle being

being measured. The third effect is the failure of the target plane to pass through the mask axis during the exit angle measurement. As illustrated in fig. 20(b), this produces a displacement of the target spot along the beam axis and a corresponding error in the exit angle found. A considerable effort was therefore made to reduce the eccentricities in the target rod assembly as much as possible. As measured with a traveling microscope, the target plane of the rod finally used passed very closely through the axis of the inner rod, but rotation of the mask and outer tube of the assembly displaced the inner axis around a circle of approximately 0.004-inch radius, resulting in an error in the exit angle of slightly over 0.05° in the worst position. The contribution of this effect to the standard deviation of the measurement was therefore taken as $\pm 0.05^{\circ}$. This was combined with an additional error, chosen rather arbitrarily as $\pm 0.1^{\circ}$, which was assigned to the measurement on the presumption that the errors of calibration of the 0.1° vernier protractor used are of this order. The total of protractor calibration and target eccentricity errors is then $\pm 0.11^{\circ}$.

Figure 21 shows a two-dimensional map of the acceptance aperture of the magnetic spectrometer taken by a similar technique to the above, with a 0.040-inch circular hole substituted for the 0.040-inch slit, and vertical as well as angular motion introduced into the sweep across the spectrometer aperture. The pronounced dip in yield in the center of the aperture is the shadow of the fluxmeter coil (see fig. 5), which is inserted directly into the center of the spectrometer vacuum box.

In analogy to the corrections to the angle measurement above due to the variations of the Rutherford scattering yield with energy and angle, a complete treatment of the theory of yields from thick targets as measured by spectrometers with finite resolution in energy and angle shows that there are small corrections to the usual practice of taking the half-way point on the rise of the thick-target step as corresponding to the energy of the entering particle as it would be measured with an ideal spectrometer of infinite resolution (27, 35). These corrections make themselves evident in a curvature of the rising face of the profile due to the variation in energy and angle of both the reaction cross section and the effective stopping power. The theory of the thick-target profile is treated in detail in Appendix B, and a calculation made of the magnitude of the correction involved in the energy of the entering particle in the case of the $C^{12}(He^3, p)N^{14*}$ reaction as performed in this experiment.

The parameters required for this calculation are the spectrometer resolution in energy and angle, which were taken from the calculations of Li (26) and the solid-angle measurements above, respectively, and the variations of the thick target yield some known energy back of the step with variations of emergent energy and angle, which it was necessary to measure. These measurements were carried out at the bombarding energy used in the Q-value experiment by varying the setting of the magnetic spectrometer in energy and angle.

It must be pointed out that, due to an oversight, the orientation

of the target was held fixed relative to the spectrometer rather than relative to the incident beam, and the additional calculations necessary to estimate the effects of this procedure seriously reduce the accuracy of the final result. The calculated correction to Q_p resulting from this effect is 0.004% with an estimated standard deviation of the same order as the correction, or perhaps somewhat larger. Considering this relatively large error, the small size of the correction, and the fact that the energy of the entering particle was obtained from the mid-points of straight lines drawn through the faces of the profiles rather than from the curves to which the correction is strictly applicable, we felt that the curvature correction could be neglected.

IV. EXPERIMENTAL RESULTS AND ANALYSIS OF DATA

A. $C^{12}(He^3, p)N^{14*}$ (2.311-Mev state)

Typical profiles resulting from the $C^{12}(He^3, p)N^{14*}$ experiment are shown in figs. 22, 23, and 17(b). Figure 22 shows the yield of protons of energy 3.633 Mev at approximately 150° laboratory angle from the $C^{12}(He^3, p)N^{14*}$ reaction near a bombarding He^3 energy of 2.69 Mev, and fig. 23 shows the deuteron yield from $Au^{197}(d, d)Au^{197}$ elastic scattering with the same spectrometer field and angle, near a bombarding energy of 1.88 Mev. Figure 17(b) shows the $Li^7(p, n)Be^7$ neutron threshold, the primary calibration point, as taken with the experimental arrangement for this reaction (see fig. 9).

Values were taken from the two spectrometer profiles by drawing a straight line through the points on the face of each profile and reading the electrostatic analyzer setting corresponding to the point on this line midway between background and maximum yield levels (see figs. 22 and 23). The neutron threshold was obtained from the usual linear extrapolation of the 2/3 power of the yield above background. It should be noted that, due to the 2/3 power plot, the position of the intercept with the axis is quite insensitive to the amount of background actually subtracted before taking the 2/3 power. In fact, for the small background generally prevailing in these measurements, generally less than two counts, but occasionally reaching 6 to 8 counts, the correction was quite negligible. This is because the subtraction of a small constant affects the position of only low-lying points to any appreciable degree, and these points are mostly in the fillet resulting from beam

resolution and are therefore ignored in the extrapolation.

The three values resulting from the above graphical analysis were then inserted in a combined Q-value equation derived from the usual kinematics of the various reactions involved. This equation is shown with its derivation in Appendix C, and includes all the small corrections to the Q-value, such as the relativistic corrections to the analyzer and spectrometer, etc., in the form of expansions about the energy and angle of the actual experimental case.

Sixteen runs of the proton reaction were made, and the resultant values of Q_p were divided into two groups of eight according to whether the corresponding run was made before or after the installation of the heat exchanger on the electrostatic-analyzer power supply as described above. This installation was the last improvement made in the equipment, and made a noticeable change in the reproducibility of the results. Because of this change and the fact that the two sets of data were taken with separate and independent measurements of the spectrometer angle, a separate analysis of the errors in each of the two sets was made. These analyses are summarized for the two sets, labelled I and II, respectively, in Table I.

The values shown in Table I are standard deviations given in terms of the effect of the uncertainty in question on the value of Q_p in kev. The errors which affect each set of data independently are the angle-measurement reproducibility, estimated from the experiment described above where the same angle was measured twice using protons and He^4 respectively, the estimated experimental error in the $Al^{27}(p,\gamma)Si^{28}$ linearity-check experiment, and the experimental error in performing

the actual $C^{12}(He^3, p)N^{14*}$ reaction experiment. The $Al^{27}(p, \gamma)Si^{28}$ experimental error quoted for Set I is the result of three runs of this reaction, and shows the effects of the thermal drifts still present in the electrostatic analyzer at that time. The value for Set II, from one run, illustrates the improvement in stability of calibration resulting from the stabilization of the analyzer power-supply box temperature.

One value of Q_p in each set was found to be far outside the limits of the others, and was accordingly discarded. The dispersion of the remaining seven points in each set was then used to calculate the statistical standard deviation of the mean of the set; again the improved stability of Set II is evident. Combining the experimental errors above with the standard deviations of the means, we arrive at standard deviations for each set, the weighting for a weighted mean of the two sets, and the standard deviation of that mean. With a weighting in the ratio of 1:5.4 favoring Set II, this internal standard deviation is $\pm$ 0.34 kev. Calculating the external standard deviation from the dispersion of the means of the two sets, we get $\pm$ 0.44 kev, in reasonable agreement.

To arrive at the final standard deviation for Q_p, we must combine this last value with the errors which affect the two sets of data coherently. These include the uncertainties in observation angle due to protractor calibration errors and target eccentricities, estimated at $\pm 0.11^{\circ}$, the uncertainty mentioned above in the coefficient of E^2 in the molecular-ion effect, taken as $\pm$ 0.2 kev/Mev^2, and the uncertainty in the primary energy scale as set by the $Li^7(p, n)Be^7$ threshold at 1880.7 $\pm$ 0.4 kev. The final result is

$$Q_p = 2468.4 \pm 1.0 \text{ kev.}$$

A point of caution is noteworthy in connection with this rather small standard deviation. The procedure used above for calculating the standard deviation of the mean of a set of data from the dispersion of the points in that set assumes that the observations in the set are independent and normally distributed. Both of these assumptions are to some degree questionable in the present case, particularly as the data in the two sets above were in many cases taken in as rapid succession as possible, introducing strong possibilities of correlations with time or such uncontrolled variables as ambient temperature. Such correlations, of course, have the effect of raising the true standard deviation of the mean towards the standard deviation of the points in the set, which in this case is a factor of $\sqrt{7}$ larger. However, as the seven points in each set are obviously much too few to give any hope of analyzing and eliminating such correlations, there is little one can do other than to note that the weighted mean of the two sets of data above, while quoted with a standard deviation of $\pm$ 0.34 kev, was derived from data the better set of which had a dispersion of $\pm$ 0.74 kev.

B. $C^{12}(He^3, n)O^{14}(\beta^+\nu)N^{14*}(\gamma)N^{14}$

As many experimenters have discovered in the past, the exponential character of a radioactive decay furnishes a very convenient means of checking the performance of a measurement in which such a decay is involved. To take advantage of this possibility in the O^{14} threshold measurement, the O^{14} activity of the target was allowed to

die away to well below the background level at intervals during the course of the experiment. Plots were then constructed of the logarithm of the delayed 2.31-Mev gamma-ray yield as a function of time following the activation. Figure 26, which is a similar curve obtained during the O^{14} half-life measurement, will serve to illustrate the essential features of these curves. The linearity of the initial portions of these decays shows that the dead time correction to the counting rate was indeed negligible for the O^{14} threshold experiment, as indicated by the direct measurements of this quantity, and that there was no evidence for other effects which might be expected to produce distortion of the decay curve, such as the loss of O^{14} from the target due to the heating action of the beam. The tail of the curve permits an evaluation of the background in both magnitude and time dependence; this evaluation may be improved by using the information on the initial activity present obtained from the beginning of the curve to subtract out the expected residual O^{14} activity from the tail. At no time during either of the two runs made of this experiment was there any evidence of 10-min or 20-min half-life contamination from C^{11} or N^{13} annihilation radiation. The background was therefore treated as a constant for each run, slightly over 50 counts/min.

Figure 24 shows the 2/3 power of the delayed gamma-ray yield in excess of background plotted versus energy of bombardment near threshold. The value plotted is the sum of the counts for the first 120 sec of each decay curve, corrected for 102 counts average background, and corrected for the remaining activity from the previous bombardment. In order to minimize this last correction, the readings were taken in

order of increasing bombarding energy. This curve is a striking example of the classic s-wave neutron threshold behavior. Note that the points where the yield was negative after background subtraction are plotted below zero on the 2/3 power plot in the interests of better display.

Least-squares fitted intercepts were calculated for both runs using uniform weighting of the points. As can be seen from the error bars in the figure, this weighting is a fairly good approximation in this case. This is because the usual counting statistics when transformed to the 2/3 power plot give errors which vary only as the fourth root of the ordinate, which is modified in the usual fashion by the background subtraction to give the distribution shown.

Each of the least-squares fittings gave a standard deviation of $\pm$ 0.2 kev in the value of Q_n; however, the external error calculated from the spread of the two values was $\pm$ 0.5 kev in Q_n. Combining this value with an almost negligible contribution of $\pm$ 0.1 kev from the linearity measurements on the electrostatic analyzer, and with the uncertainty in the $Li^7(p,n)Be^7$ energy scale, we arrive at the final values

$$Q_n = -1148.8 \pm 0.6 \text{ kev}$$

$$E_{th} = 1437.5 \pm 0.7 \text{ kev.}$$

The Q-value formula and the details of the corrections to these values are shown in Appendix C.

C. O^{14} Half-life

The results of the O^{14} half-life experiment are illustrated by figs. 25 and 26. Figure 25 is a semilogarithmic plot of typical delayed

gamma-ray pulse-height spectra taken during this experiment, showing (a) the full spectrum of the target without the lead absorber which was used during the actual measurement, and (b) the spectrum as run, with a 2-cm Pb absorber between target and scintillator to attenuate the annihilation radiation. In both cases the spectrum of the pulses coincident with the output of the differential discriminator is shown superimposed on the full spectrum. Note the annihilation-radiation pileup at points A, B, and C without the lead in contrast to the greatly reduced pileup at D and the increased resolution for the N^{14} gamma ray with the lead. The 2-cm absorber was used for four of the five runs made of this experiment; the fifth, using a 1-cm absorber, gave very similar spectra and an indistinguishably similar decay curve in comparison with the other runs. Figure 26 shows a semilogarithmic plot of the yield from the discriminator versus time as corrected for dead time. The result of subtracting background, taken as a constant, is also shown.

The five runs were analyzed by least-squares fittings of straight lines to the natural logarithms of the counts corrected for dead time and background, taken as a function of time in 20-sec counting intervals. The value for each time channel was weighted according to the square of the corrected counts divided by the raw counts. This weighting was used to take into account the effect on the standard deviations of the logarithmic counts of the addition of the relatively well-known dead time and background corrections to the raw counts.

The decay curves for the various runs were investigated for time-dependent background, faults in the dead-time correction, and other possible distortion mechanisms by comparing half-lives fitted to various

portions of each curve, and also by inspection of the time dependence of the background remaining after subtracting the least-squares fitted decay from the raw counts plus dead-time correction. No evidence of such distortion of the decay curve was found.

Inspection of the record of pulse-height distribution in coincidence with the discriminator output during the first two runs of the experiment showed a small gain shift during the run. Corrections to the half-life of + 0.05 sec and + 0.2 sec were estimated from the pulse-height spectrum and applied to the results of the least-squares analysis, with a corresponding increase in standard deviation. For the last three runs, the amplifier was shifted to a regulated power line, and no significant shifts appeared.

The final weighted average of the five runs of the O^{14} half-life experiment is

$$t = 71.00 \pm 0.13 \text{ sec.}$$

The standard deviation quoted is the external standard deviation derived from the scatter of the values from the five runs. The internal standard deviation was ± 0.09 sec, indicating the possibility that errors other than those associated with counting statistics and with the corrections above were present.

The above value differs from the value 71.1 ± 0.2 sec quoted in the preliminary report (19) on this experiment by the inclusion of two additional runs for which the analysis was not completed in time for publication.

D. Summary of Results: The ft-Value of the Transition

Table II summarizes the various results of the experiment. The value of $E_{max}(\beta^+) = 1812.6 \pm 1.4$ kev was calculated from equation 3; the standard deviation quoted is slightly increased by the fact that the uncertainties in the $Li^7(p,n)Be^7$ threshold and in the coefficient of the molecular-ion effect apply to the whole energy scale of the experiment, and hence their contributions to the standard deviations of Q_n and Q_p must be combined coherently. The value of f was found by numerical integration from the National Bureau of Standards Tables for the Analysis of Beta Spectra (36). A small correction (-0.065%) was applied to the result to take into account the more recent value (21) of the electron mass ($m_e c^2 = 0.510976$ Mev).

Our value for the half-life of O^{14}, $t = 71.00 \pm 0.13$ sec, when corrected for the ground state branch of the decay, $0.6 \pm 0.1\%$ (23), gives $t^* = 71.43 \pm 0.15$ sec for the half-life of the transition to the N^{14*} excited state. This gives an uncorrected ft-value of 3069 ± 12 sec. This half-life has also been carefully measured recently by Hendrie and Gerhart (37), who give the weighted mean of 40 runs as $t = 70.91 \pm 0.04$ sec, in quite satisfactory agreement. This leads to values of the partial half-life and ft-value $t^* = 71.34 \pm 0.08$ sec and $ft = 3065 \pm 10$ sec, respectively, using the f-value from Table II. If the two total half-life measurements are averaged with weights inversely as the quoted standard deviations, we find $t^* = 71.36 \pm 0.09$ sec and $ft = 3066 \pm 10$ sec.

The corrections which must be made to the O^{14} ft-value before calculating the vector coupling constant G_V fall into two classes. The

first group, which will be applied immediately, are relatively free of theoretical uncertainties. Totalling + 0.289% correction to f as listed by Durand, et al. (6), they include the effects on the electronic wave functions in the beta decay of nuclear electromagnetic form factors and electron screening, and the effects of competition from K-electron capture. As they are all related to the electronic wave functions involved, they will be termed the electronic corrections to the ft-value. The remaining group of corrections are nuclear and radiative in character, and will be discussed below.

Applying the electronic corrections, we arrive at the value ft = 3075 ± 10 sec for the transition $O^{14}(\beta^{+}\nu)N^{14*}$ (2.31-Mev state), excluding only the nuclear and radiative corrections.

V. DISCUSSION AND CONCLUSIONS

It will be noted that the experimental Q-value for the $C^{12}(He^3, p)N^{14*}$ reaction given in Table II differs somewhat from that quoted in the preliminary report on this experiment (19). The sources of this difference are a more sophisticated treatment of the experimental error calculations, resulting in a slightly different weighting of the data, and a completely new analysis of the electrostatic-analyzer linearity-check experiment. The inclusion of the effects of the HH^+ molecular-ion beam as discussed above resulted in removing a -1.3 kev correction to the $C^{12}(He^3, p)N^{14*}$ Q-value which had previously been applied.

In order to compare the Q-value resulting from the $C^{12}(He^3, p)N^{14*}$ experiment with the values calculated from the mass tables, we will use the result of Sanders (38) for the excitation of N^{14*}. Corrected for the new value of the $Li^7(p, n)Be^7$ threshold (24), this is 2311.4 ± 1.2 kev, which yields a Q-value for the $C^{12}(He^3, p)N^{14}$ ground-state reaction of 4779.8 ± 1.5 kev when combined with our result. This is in good agreement with the value 4778.6 kev calculated from the mass tables of Everling, et al. (20), but definitely disagrees with the value 4767.8 ± 3.9 kev from the older tables of Mattauch, et al. (13).

The agreement of our $C^{12}(He^3, p)N^{14*}$ Q-value with the later mass tables is satisfactory, but the present lack of direct experimental confirmation is undesirable in a measurement which bears so directly on the question of the universality of the Fermi interaction. It is to be hoped that this lack will be remedied in the near future.

The predictions of the mass tables for the Q-value of the $C^{12}(He^3, n)O^{14}$ reaction are not nearly as precise; the tables of Mattauch, et al. (13), give $Q_n = -1166 \pm 39$ kev, while those of Everling, et al. (20), predict $Q_n = -1152 \pm 5$ kev. From Table II, our experimental value is $Q_n = -1148.8 \pm 0.6$ kev, consistent with either set of tables. This value again differs from that in our preliminary report (19) by the inclusion of the HH^+ molecular-ion effect, producing a difference of 0.4 kev in this case.

The experimental situation for the $C^{12}(He^3, n)O^{14}$ threshold is considerably better. Our value for $Q_n = -1148.8 \pm 0.6$ kev differs but slightly from the latest of the series of measurements made by the NRL group (15-17), which gives $Q_n = -1147.7 \pm 0.7$ kev. Both of these measurements are in clear disagreement with that of Bromley, et al. (12), $Q_n = 1158.5 \pm 3$ kev, for reasons which are not at all evident. It is felt that further experimental work on this threshold would be desirable, both because of this disagreement and in view of the unnecessary complications (such as the molecular-ion effect) in some of the present procedures.

The predictions of the mass tables for the end-point energy of the beta transition are also rather imprecise. Using the N^{14*} excitation measurement of Sanders (38), the masses tabulated by Mattauch, et al. (13), give $E_{max}(\beta^+) = 1818 \pm 40$ kev, while those of Everling, et al. (20), predict $E_{max}(\beta^+) = 1815 \pm 5$ kev. The value calculated from the present experiment is $E_{max}(\beta^+) = 1812.6 \pm 1.4$ kev, and is consistent with both tables.

Aside from the direct measurements of Penning and Schmidt (11),

and of Gerhart (10), who gives $E_{max}(\beta^+) = 1835 \pm 8$ kev, in rather poor agreement with the present values, previous experimental determinations of the end-point energy have necessarily depended on the mass tables for a value of Q_p. The large change in this value between the 1956 tables (13) and the 1960 tables (20) points up the desirability of further measurements of the end-point energy which do not require the use of the tables.

The half-life of the transition, like the $C^{12}(He^3, n)O^{14}$ threshold, has a considerable experimental history (10, 23, 37, 39). The earlier experiments, however, seem to have suffered from the ease with which longer-lived positron emitters are produced along with the O^{14}. The result of the present experiment, $t = 71.00 \pm 0.13$ sec, disagrees with Gerhart's earlier result, $t = 72.1 \pm 0.4$ sec (10), but is nicely supported by the more recent measurement of Hendrie and Gerhart, $t = 70.91 \pm 0.04$ sec (37).

The ft-value resulting from the weighted mean of our half-life measurement and that of Hendrie and Gerhart (37) was corrected by $+ 0.289\%$ for electronic effects using the corrections listed by Durand, et al. (6). The remaining corrections which must be applied before calculating values of the coupling constant from the ft-value and the experimental muon life-time are the radiative or electromagnetic corrections to both the muon decay and the O^{14} decay, and a series of corrections to the nuclear matrix element of the O^{14} decay (6, 40). These remaining corrections are all subject to varying amounts of theoretical uncertainty. The Coulomb corrections to the nuclear matrix element, in particular, which were taken by Durand, et al. (6), from the work of

MacDonald (40), are model dependent, and vary strongly with the choice of energy denominators. As the radiative corrections are also subject to some theoretical controversy, the effects of these various corrections will be shown in detail in Table III.

The first column of results in Table III includes only the +0.289% electronic correction to the O^{14} ft-value. The Fermi coupling constant G_v is then calculated from the relation*

$$G_v^2 ft = \frac{\pi^3 \hbar^7 \ln 2}{m_e^5 c^4}$$

G_v is also given in theoretical units ($\hbar = c = 1$) by multiplying by $M_p^2 c/\hbar^3 = 0.7153 \times 10^{44}/\text{erg-cm}^3$. The relation

$$G_\mu^2 \tau_\mu = \frac{192 \pi^3 \hbar^7}{m_\mu^5 c^4}$$

together with the means of the recent experimental measurements of the muon mean life, $\tau_\mu = 2.210 \pm 0.003$ μsec (7, 8), and muon mass, $m_\mu = 206.77 \pm 0.01\ m_e$ (9), gives us the value of G_μ. The percentage discrepancy between G_μ and G_v is then calculated both directly and in terms of the corresponding discrepancy in lifetimes, yielding $1.0 \pm 0.2\%$ and $2.0 \pm 0.3\%$, respectively.

The second column of Table III shows the effects of adding the nuclear corrections as listed by Durand, et al. (6). These corrections include -0.35% for the Coulomb corrections and -0.024% for second forbidden matrix elements.

*For a discussion of this relation and the one following, see, for example, the review article of Konopinski (41).

The third and fourth columns of the table include in addition the radiative corrections to both the O^{14} ft-value and the muon mean life, as calculated by Kinoshita and Sirlin (5) (K and S) and Durand, et al. (6), (DLM), respectively. It should be pointed out that the calculations of Durand, et al., are based on a quite different theoretical approach from that of Kinoshita and Sirlin, resulting in a different definition of the coupling constant. Hence neither the values of G_V nor the values of the corrections are expected to be comparable in the two cases. Note also that the O^{14} radiative correction of Kinoshita and Sirlin includes a contribution from the anomalous magnetic moments of the neutron and proton which they have estimated at +0.2% from the work of Berman (4).

The above calculations have been made on the assumption that the Fermi interaction is a contact interaction between the four fermions involved in the decay. It is interesting to note the effects of the suggestion which has recently attracted some attention (1, 42, 43) that the interaction in fact involves two vertices connected by the exchange of an intermediary heavy charged vector meson. Oneda and Pati (43) have calculated this nonlocal effect on the decay rate of the muon finding that $W = W_o(1 + 0.6(m_\mu/m_B)^2)$, where W_o is the decay rate for the contact interaction, and m_μ and m_B are the masses of the muon and the intermediate meson, respectively. Due to the much lower momenta involved, the effect on nuclear beta decay is completely negligible. As the mass m_B must be at least that of the K meson to forbid the decay of the K meson into the intermediate meson, the maximum possible correction to the muon lifetime from this source must be very close to

$+ 0.6(m_\mu/m_K)^2 \approx + 2.8\%$. This corresponds to a correction to G_μ of $- 1.4\%$. If the corresponding nonlocal effects on the radiative corrections can be neglected, it is seen from Table III that this effect could give considerable assistance in removing the present discrepancy between theory and experiment.

In conclusion, while it seems likely that the experimental ft-value could be further improved by additional work, the values quoted in the first column of Table III are regarded as reasonably reliable, subject to some reservations on the validity of the interpretation of the molecular-ion effect discussed above. On the other hand, it is felt that on closer examination the nuclear corrections in the second column could quite possibly change enough to account fully for the present discrepancy between theory and experiment; the radiative corrections, too, present their difficulties. One would conclude, then, that the question of the universality of the Fermi interaction at present depends primarily on further theoretical clarification of these problems.

Table I: Errors Contributing to Q_p. The various sources of error contributing to the standard deviation of Q_p are itemized in terms of their effects on Q_p in kev. Sets I and II each contain seven runs, and are analyzed separately because of the installation of temperature stabilization in the analyzer power supply between the two sets. See text pp. 35 ff.

Table I: Errors Contributing to Q_p

Source	Set I	Set II	
Analyzer Linearity Measurement	± 0.76	± 0.16	kev
Angle Measurement: ± 0.03°	± 0.18	± 0.18	kev
Dispersion of Measured Values	± 0.36	± 0.28	kev
Resultant Standard Deviations	± 0.86	± 0.37	kev
Resultant Weights	1.0	5.4	
Standard Deviation of Weighted Mean	± 0.34		kev
External Error	± 0.44		kev
Protractor Calibration, etc.: ± 0.11°	± 0.66		kev
Energy Scale Uncertainty	± 0.53		kev
Molecular Ion Correction: ± 0.2 kev/Mev^2	± 0.28		kev
Final Standard Deviation of Q_p	± 0.99		kev

Table II: Summary of Experimental Results. The various experimental results of the present work are tabulated, and the effect of including the half-life measurement of Hendrie and Gerhart (37) in a weighted mean is shown. See text pp. 42 f. and 46 ff.

[a] Half-life measurements weighted inversely as the quoted error.

[b] Including electronic but excluding radiative and nuclear corrections; see text.

Table II: Summary of Experimental Results

$C^{12}(He^3, p)N^{14*}$	Q_p =	2468.4 ± 1.0	kev
$C^{12}(He^3, n)O^{14}$	Q_n =	-1148.8 ± 0.6	kev
	E_{th} =	1437.5 ± 0.7	kev
End-point Energy	$E_{max}(\beta^+)$ =	1812.6 ± 1.4	kev
	$W_{max}(\beta^+)$ =	2323.6 ± 1.4	kev
f-Value	f =	42.97 ± 0.13	
Half-life of O^{14}	t =	71.00 ± 0.13	sec
Half-life Corrected for Ground State Branch	t^* =	71.43 ± 0.15	sec
Uncorrected ft-Value	ft^* =	3069 ± 12	sec
	Weighted Mean Values[a]		
Corrected Half-life	t^* =	71.36 ± 0.09	sec
Uncorrected ft-Value	ft^* =	3066 ± 10	sec
Corrected ft-Value[b]	ft =	3075 ± 10	sec

Table III: A tabulation of the results of applying the various theoretical corrections to the experimental result is shown, and comparisons are made between the values of the vector coupling constant and the muon lifetime as predicted from the present experiment and from the data on muon decay. The corrections included in each column are indicated by the headings: Column E: Electronic corrections only. Column E and N: Electronic and nuclear corrections only. Column K and S: The radiative corrections to both muon and O^{14} decay are included as calculated by Kinoshita and Sirlin (5). Column DLM: The radiative corrections as calculated by Durand, Landowitz, and Marr (6) are applied. The electronic and nuclear corrections are taken from the summary of Durand, et al. (6), in all cases. See text pp. 42 f and 46 ff.

Table III

Quantity	Corrections Included	E	E and N	K and S	DLM	Units
ft		3075 ± 10	3063	3116	3032	sec
	Electronic:	+0.289	+0.289	+0.289	+0.289	%
	Nuclear:	-----	-0.374	-0.374	-0.374	%
	Radiative:	-----	-----	+1.7	-1.03	%
G_v		1.4143 ± 0.0022	1.4170	1.4050	1.4243	$\times 10^{-49}$ erg-cm^3
		1.0116 ± 0.0016	1.0135	1.0049	1.0187	$\times 10^{-5}/M_p^2$ ($\hbar = c = 1$)
τ_μ		2.210 ± 0.003	2.210	2.201	2.181	μsec
	Radiative:	-----	----	-0.42	-1.32	%
G_μ		1.4282 ± 0.0011	1.4282	1.4312	1.4377	$\times 10^{-49}$ erg-cm^3
		1.0215 ± 0.0008	1.0215	1.0237	1.0284	$\times 10^{-5}/M_p^2$ ($\hbar = c = 1$)
$(G_\mu - G_v)/G_\mu$		1.0 ± 0.2	0.8	1.8	0.95	%
$(\tau_\mu - \tau_v)/\tau_\mu$		-2.0 ± 0.3	-1.6	-3.8	-1.9	%

APPENDIX A

1. Fluxmeter Modifications

Figure 27 is an overall diagram of the fluxmeter current-balance assembly after modification; the original assembly was identical in principle except for the bearings, but was constructed almost entirely of brass, with a thin aluminum coil form, and a much lighter main supporting bar (26). The improved assembly was made of aluminum assembled with Eastman 910 pressure-setting cement. The 7/8-inch-diameter lucite coil form was wound with 40 turns of No. 32 magnet wire to which was soldered a twisted pair of heavier gauge wire secured along the balance rod with spots of shellac. Light copper damping rings were cemented to the interior of the coil. Four short lengths of copper galvanometer suspension serve as current leads to the balance rod. As these leads are brought out of the vacuum chamber separately through a small glass-to-metal seal, it is possible to use a Kelvin bridge circuit to measure the resistance of the fluxmeter coil itself, independent of the quite comparable resistance of the flexible leads. This permits monitoring the temperature of the coil.

The entire balance-rod assembly, which weighs slightly over 10 gm, is designed so that its center of gravity exclusive of the counter-weight lies as closely as possible along the axis of rotation. The counter-weight is a brass cylinder weighing about 600 mg mounted on a thin quartz rod. Its horizontal offset of about 1.5 inch and its vertical offset in the balanced position of about 0.2 inch below the bearing axis then produce the principal moments contributing to the calibration and sensitivity of

the fluxmeter. The total center of gravity of the balance rod is consequently about 2 mm from the bearing axis and slightly below it.

By far the most important change made in the system was the change in bearings. Figure 6 shows both types of bearing in section as viewed along the axis of rotation. The old form (fig. 6(a), (b)) consisted of a glass cup bearing riding on a ground tungsten needle. As is evident from the figure, the effective radius from the axis of rotation to the center of mass of the balance rod depended on the position the needle happened to assume inside the cup. It was judged that the range of positions available inside the cup was of the order of 1% of the 2-mm effective radius arm of the balance, and hence would account for the observed 1% changes in calibration. The situation was further complicated by the difficulty of adjusting the two needles to exactly the correct distance between the two bearings.

The new bearings (fig. 6(c)-(e)) were constructed from sapphire phonograph styli riding on flat glass plates. The geometry of sphere rolling on plane removes the dependence of the moment arm on the position of the stylus on the plate. This liberty must not be allowed to become license, however, as the requirement of an accuracy of 1 in 10^4 in spectrometer calibration sets a limit of movement on the coil of 0.003 inch in the direction of the field gradient in the spectrometer, which is the axial direction for the fluxmeter. As it was felt that a caging mechanism would be unnecessarily elaborate, this limitation was accomplished by putting up fences, with the idea that a stylus resting against one of its fences could be recentered in its proper position by merely rocking the fluxmeter rod back and forth with the coil current

or field controls (see fig. 6(e)).

The detailed construction of the bearings is shown in fig. 28. The styli were taken from standard 0.003-inch-radius sapphire replacement phonograph styli of a type which looked reasonably easy to take apart (such as Walco type W-104S). After the sapphire was removed from its mounting and washed free of cement, it was shellacked point first onto the end of a 1/16-inch wooden rod. Working under a microscope, we then dipped the butt end of the sapphire into a drop of Eastman 910 cement and mounted it in the end of an 0-80 brass machine screw which had previously been drilled out to receive it. Either undue hesitation in the performance of this step or too close a fit between the sapphire and its mounting hole will result in setting of the cement before the stylus is properly seated. Polymerization of the cement was essentially complete within ten seconds, and the shellac joint then broke away easily from the mounted sapphire. After being cleaned of all excess cement and the remaining shellac, the assembly was screwed into place with a lock-nut on the balance rod.

The mating bearings were made from small round pieces cut from glass microscope slides. The mounting studs and retaining caps were machined from brass. The dimensions for machining the slot and hole that served as fences for the two bearings were taken from comparison-microscope measurements of the dimensions of the sapphires. The bearings were assembled by applying a drop of Eastman 910 cement to the end of the stud, and then inserting it with decision into the cap containing the bearing plate.

The complete fluxmeter assembly also includes a mirror made from an aluminized 1-inch-square microscope cover glass cemented to the balance rod, and a set of adjustable stops that restrain the opposite end of the quartz rod carrying the counterweight. The stops were made from heavy busbar stock covered with Teflon sleeving to minimize the possibility of sticking of the balance on the stops.

The final design has been found to eliminate most of the difficulties encountered in the previous system. The energy calibration of the spectrometer is much more stable, and the installation and adjustment of the system is much easier, as the screw mounting of the sapphires provides an easy adjustment of the sensitivity of the balance, and the use of a slot fence for the second bearing makes accurate adjustment of the bearing separation unnecessary. When the bearings were inspected after nearly a year of service, no significant indications of wear were visible. The primary source of annoyance occasioned by the system is the tendency of the balance rod to "walk" up against its fences, resulting in a sharp drop in sensitivity and a shift in calibration. This tendency is believed to be a result of the slight inclination of the fluxmeter axis to the horizontal. Due to the fringing field of the spectrometer, its total deflection angle is slightly over 180° (26), and it is therefore slightly tilted backward in its carriage to put the effective entrance aperture in the horizontal plane, producing a corresponding tilt in the axis of the fluxmeter. This "walking" tendency is easily counteracted, however, by an occasional sharp rap with a screwdriver handle on the side of the fluxmeter housing.

These modifications to the fluxmeter were carried out in collab-

oration with Mr. Jack C. Overley.

2. Accessory Modifications

The photoelectric indicator system for the fluxmeter presents many possibilities for improvement; the optical system in particular may with some justice be termed astonishing in a precision instrument. The stability of the associated amplifier, however, bears more directly on the reproducibility of the spectrometer calibration. At the usual sensitivity setting of the fluxmeter current balance, a change in the spectrometer field of about 0.2% is required to swing the light beam from one plate of the pickoff phototube to the other, producing the maximum output swing of the indicator circuit. Instabilities in the amplifier therefore produce corresponding changes in the spectrometer field within this range. To limit this possible source of calibration drift, the amplifier was rebuilt using an AC-coupled circuit with inherently good zero stability. Figure 29 shows the resulting design.

Several points are worthy of note in this circuit. There are two main sources of error currents in an AC-operated phototube: the usual dark current, which is a strong function of applied voltage for the tube used, and a fairly sizeable capacitive feedthrough current. The dark current is stabilized by using the stabilized B+ supply to limit the anode voltage swing on the phototube. As this voltage is clamped to ground during the negative swing of the power transformer, the resulting waveform is nearly a positive-going square wave with a stabilized peak value. The effectiveness of the arrangement is enhanced because the dark current depends primarily on this stabilized peak voltage.

The capacitive feedthrough current, which has proven rather difficult to handle in many previous AC-operated phototube circuits, is in phase in the two halves of the present circuit, and is therefore strongly rejected by the difference amplifier. The remaining fraction, mainly due to uncompensated asymmetries in the phototube, is 90^{o} out of phase with the desired signal current, and is removed by the excellent quadrature rejection of the ring demodulator. To maintain this quadrature rejection, stray phase shifts in the system must be minimized. Immunity to phase shifts in the power transformer due to varying line and load conditions is guaranteed by using the same winding to drive all synchronous elements in the system, and the amplifier is designed for small phase shift.

In operation, the balance control in the demodulator circuit is set for minimum AC current in the meter circuit, and the zero control is set with the fluxmeter light turned off. The resulting settings are quite stable with line voltage, and after a brief warmup period, seem to drift principally with the aging of the components.

A considerable increase in the convenience of operating the fluxmeter was produced by rebuilding the coil current-control and measurement system as shown in fig. 30. This rebuilt system incorporates facilities for using a Hewlett-Packard Model 425A Microvoltammeter in a feedback loop to lock the coil current to the value corresponding to the setting of the Rubicon Type B potentiometer. The system is thereby made very nearly free of drift save for that of the battery supplying the potentiometer slidewire. As this battery draws a constant and relatively small current, the system equilibrium is rapidly reached and

easily maintained.

The fluxmeter coil current passing through the 20-ohm standard resistor produces a voltage which is measured by the Type B potentiometer. The error signal from the potentiometer is amplified by the microvoltammeter, passed through a transistor phase inverter and buffer amplifier, and the resulting signal added to the output of the manual current controls. The inverter and buffer contain gain and balance controls, and the necessary frequency-response limitation to prevent oscillation of the feedback loop.

The manual current controls were constructed from Helipot Type A 10-turn potentiometers to reduce the number of knobs required to attain the necessary current resolution. Connecting the fine control in the current-divider configuration permitted the use of a reasonably large value of resistance in the winding, and considerably eased the problem of slider contact resistance, as the contact is in series with 20 kΩ. However, contact noise is still troublesome with these potentiometers, particularly the coarse control; better quality controls would probably be advisable.

The system is completed by the two six-volt storage batteries and a charger system.

After the installation of the improvements above, an attempt was made to determine a temperature coefficient for the spectrometer calibration constant. Figure 31 shows the circuit of a modified Kelvin bridge which was used as a resistance thermometer to measure variations in the temperature of the fluxmeter coil. A Kelvin bridge was necessary because of the relatively large and temperature-dependent

resistance of the flexible leads to the coil. In this particular bridge, the two sets of ratio arms labeled AXD and BYC are used to compare the coil resistance with the 20-ohm standard resistor. Power is supplied by the regular coil-current supply, and the usual functions of the fluxmeter circuitry are not interfered with as long as the bridge is reasonably near balance. The balance point is strictly independent of the resistances of the leads carrying the main coil current only when the ratios of the two sets of ratio arms are equal, and a true Kelvin bridge would have a second variable tap at point Y moving in synchronism with that at point X. However, the values are chosen so that the ratios are never sufficiently far from equal to cause significant difficulty.

Tests of the stability of the spectrometer calibration were made by following the position of the 6.05-Mev α-particle line from Bi^{212} produced in a Pb^{212} (Th B) source. After the spectrometer was turned on, it generally showed a slow drift over a range of the order of 0.05% in field distributed over several hours. This drift was very poorly correlated with the readings of the Kelvin bridge and of a thermometer inserted in a hole in the side of the magnet, and the correlation was entirely destroyed by turning the field off for an hour or so, which was necessary every few hours to avoid overheating at the required magnet current. Once thoroughly warmed, the spectrometer maintained calibration to about $\pm$ 0.015%, wandering within that range in a very complicated fashion.

It is presumed that this behavior indicates the presence of

several different temperature dependences of similar magnitudes but having different responses to the time history of the power input to the spectrometer. This is consistent with the picture of the spectrometer as a thermal system having many different normal modes of thermal fluctuation, each of which may be coupled (e.g., by thermal expansion of the magnet) to the calibration. The presence of other effects, such as slow magnetic relaxation of the iron, is also possible. One can only conclude that the temperature of the fluxmeter coil itself does not play a large role in the drift.

APPENDIX B

The Nuclear Reaction Yield from a Thick Target

Introduction. The nuclear reaction or scattering yield from a thick target is usually observed by some form of particle spectrometer with well-defined resolutions in both energy and angle. When plotted as a function of either beam energy or spectrometer energy setting, the yield from reactions leading to well-defined states of the residual nucleus traces out a profile in the general form of a step, consisting of a steeply rising face followed by a plateau having relatively slow variation with energy. This distinction in profile shape may of course be obscured by the presence of structure in either target or cross section; the two regions of the profile are therefore formally characterized by the relationship between the spectrometer resolution window and the highest energy particles emerging from interactions in the surface layers of the target. If the beam energy is raised from a value low in relation to the spectrometer energy setting, these particles are the first to appear in the spectrometer window, giving rise to the face of the profile as an increasing fraction of the window is filled. The plateau of the profile is reached when the window is completely filled.

It has been evident for some time that the treatment of thick-target yields by Brown, Snyder, Fowler, and Lauritsen (27), while capable of predicting the yield as extrapolated to the surface of the target, is inadequate in two respects in its prediction of the actual shape of the profile. In the first place, no attempt was made in this earlier treatment to calculate the effects on the shape of the initial rise of the

profile of either the angular resolution of the spectrometer or the presence of appreciable variation of the yield with energy or angle. Secondly, the usual prescription for applying this treatment to the calculation of the slope of the plateau following the initial rise does not agree particularly well with experimental profile shapes. To take a well-known example, the yield from Rutherford scattering with a uniform thick target shows a characteristic decrease of the yield as the spectrometer field is lowered to values corresponding to scattering from laminae deeper inside the target, the bombarding energy being held fixed. If we use the atomic stopping cross sections corresponding to the average energies of the entering and emerging particles over their ranges of energy loss in the target, which has been the usual practice, the treatment of Brown, et al. (27), accounts for only about half the decrease in yield.

A better understanding of these phenomena is also desirable because of the possible existence of corrections to Q-values derived from thick-target measurements due to the details of the shape of the profile. One such correction is in fact given by the earlier treatment (27).

Fundamental Relations. The differential yield per incident particle from a thin lamina in the interior of a thick target may be written

$$dY = \sigma(E_1, \theta)\, W(E_{20}, \theta, \phi) n' \, ds \, d\Omega / \cos \theta_1 , \qquad (1)$$

where $\sigma(E_1, \theta)$ is the differential cross section for the reaction in question in the laboratory system with coordinates E_1 and θ, E_1 being the

energy of the entering particle at the lamina in question, and $W(E_{20}, \theta, \phi)$ is the resolution function or the fractional transmission of the spectrometer at the energy E_{20} of the emergent particle as it leaves the surface of the target, and at angular position θ, ϕ; i.e., $W(E_{20}, \theta, \phi)$ is the probability that a particle of energy E_{20} incident on the spectrometer at angular position θ, ϕ will pass through the spectrometer and be counted. W is, of course, a function of spectrometer setting in both energy and angle. In addition, n' is the number density of reacting nuclei in the lamina; ds is the normal thickness of the lamina at normal depth s in the target; θ_1 is the angle between the incident beam and the target normal; and $d\Omega$ is the element of solid angle. Other quantities of interest (see fig. 32(a)) are E_{1B}, the incident beam energy, E_2, the emergent particle energy immediately after the reaction, and θ_2, the angle between the emergent particle momentum and the target normal. Obviously,

$$\theta_1 + \theta_2 = \pi - \theta, \tag{2}$$

and we may make use of the usual reaction kinematics to write

$$E_2 = E_2(E_1, \theta) \tag{3}$$

The usual definition of the atomic stopping cross section is

$$\epsilon(E) = -\frac{1}{n}\frac{dE}{dx}, \tag{4}$$

where n is the total density of stopping atoms in the lamina, and x is the distance traveled by the particle. If we assume that n and $\epsilon(E)$ are independent of x (i.e., the target is of uniform composition with

depth), the variables in this equation are separable, and the solutions for the entering and emerging particles are given by

$$\left.\begin{aligned} \int_{E_{1B}}^{E_1} dE/n\epsilon_1(E) &= -\, s/\cos\theta_1 \qquad (5a) \\ \int_{E_2}^{E_{20}} dE/n\epsilon_2(E) &= -s/\cos\theta_2 \qquad (5b) \end{aligned}\right\} \; s \geq 0$$

where ϵ_1 and ϵ_2 refer to the entering and emerging particles, respectively.

We now choose as independent variables E_{20}, θ, and ϕ, and integrate equation 1 over the region of acceptance of the spectrometer:

$$Y = \int_{s\geq 0} dE_{20} d\Omega \sigma(E_1, \theta)\, W(E_{20}, \theta, \phi) n' (\partial s/\partial E_{20})_{\theta,\phi}/\cos\theta_1 \qquad (1a)$$

The requirement $s \geq 0$ in the integral generates the rising face of the profile, illustrating the relation between the face of the profile and the limit $s = 0$ defining the target surface. An obvious generalization at this point is the inclusion of targets of finite thickness t by requiring $t \geq s \geq 0$ in the integral.

We must now use equations 2 through 5 to eliminate the dependent variables from equation 1a. The values of E_1 and E_2 are functions of the detailed behavior of the stopping powers and of the reaction kinematics, but as they may usually be calculated for a particular case by quite straightforward approximation techniques applied to the integrals in equations 5, their calculation will be carried no further in the present general treatment. The value of $(\partial s/\partial E_{20})_{\theta,\phi}$, however,

may be more profitably pursued.

Since the integrals on the left in equations 5 are independent of s as a result of the separation of variables in the solution of equation 4, we may differentiate equations 5 with respect to E_{20} at constant θ and ϕ to give

$$\left(\frac{\partial s}{\partial E_{20}}\right)_\theta = - \frac{\cos \theta_1}{n\epsilon_1(E_1)} \left(\frac{\partial E_1}{\partial E_{20}}\right)_\theta \tag{7}$$

$$\left(\frac{\partial s}{\partial E_{20}}\right)_\theta = - \frac{\cos \theta_2}{n} \left[\frac{1}{\epsilon_2(E_{20})} - \frac{1}{\epsilon_2(E_2)} \left(\frac{\partial E_2}{\partial E_{20}}\right)_\theta \right] \tag{8}$$

Since from equation 3 we have

$$\left(\frac{\partial E_2}{\partial E_{20}}\right)_\theta = \left(\frac{\partial E_2}{\partial E_1}\right)_\theta \left(\frac{\partial E_1}{\partial E_{20}}\right)_\theta \tag{9}$$

we may combine the last three equations to find

$$\left(\frac{\partial E_1}{\partial E_{20}}\right)_\theta = \left[\frac{\epsilon_2(E_{20})}{\epsilon_2(E_2)} \left(\frac{\partial E_2}{\partial E_1}\right)_\theta + \frac{\epsilon_2(E_{20})}{\epsilon_1(E_1)} \frac{\cos \theta_1}{\cos \theta_2} \right]^{-1} \tag{10}$$

$$\left(\frac{\partial s}{\partial E_{20}}\right)_\theta = - \frac{\cos \theta_1}{n\epsilon_2(E_{20})} \left[\frac{\cos \theta_1}{\cos \theta_2} + \frac{\epsilon_1(E_1)}{\epsilon_2(E_2)} \left(\frac{\partial E_2}{\partial E_1}\right)_\theta \right]^{-1} \tag{11}$$

Inserting equation 11 in equation 1a, we obtain the result

$$Y = \int_{s \geq 0} \frac{dE_{20}\, d\Omega\, n' \sigma(E_1, \theta)\, W(E_{20}, \theta, \phi)}{n\epsilon_2(E_{20}) \left[\frac{\cos \theta_1}{\cos \theta_2} + \frac{\epsilon_1(E_1)}{\epsilon_2(E_2)} \left(\frac{\partial E_2}{\partial E_1}\right)_\theta \right]} . \tag{12}$$

The sign of the result is not significant and has been dropped. Note that

equations 9 and 10 give convenient first-order solutions for E_1 and E_2.

It would, of course, be possible to integrate the above result over a distribution of incoming particle energies and angles, thus including the effects of beam resolution. The effects of straggling, however, are not included so easily in this exact treatment.*

Extension to Non-uniform Targets. In the case of a non-uniform target, equations 5 are no longer solutions of equation 4, as both ϵ and n are in general functions of x, and the variables are no longer separable. The problem then is to eliminate s between two different solutions of equation 4 with boundary conditions and stopping powers for incident and emergent particles, respectively. The special case of a target made up of a number of finite, uniform layers, however, may be treated simply by breaking up equations 5 into the same number of separate integrals, and then differentiating as before. Algebraic manipulation will then lead to results analogous to equations 10, 11, and 12, but involving in addition the stopping powers for the emergent particle on either side of each discontinuity in composition. If the discontinuities through which the emerging particle must pass after the reaction are numbered from 1 to m from the target surface inward, the resulting equations are in fact identical to equations 10, 11, and 12, provided one makes the substitution

$$\epsilon_2(E_{20}) \rightarrow \epsilon_2(E_{20}) \prod_{i=1}^{i=m} \frac{\epsilon_{i+}}{\epsilon_{i-}} \qquad (12a)$$

*A general approach to the straggling problem has been given by K. R. Symon, quoted by Bruno Rossi (44).

wherever $\epsilon_2(E_{20})$ appears. The quantities ϵ_{i+} and ϵ_{i-} are the atomic stopping cross sections for the emergent particle evaluated at the energy of the particle at the ith discontinuity and for the homogeneous target material between the ith discontinuity and the (i + 1)th or (i - 1)th discontinuity, respectively.

The variation with energy of the quotient of ϵ_{i+} and ϵ_{i-} is very slow; for many cases it can be treated as a constant. At energies high enough that the usual theoretical treatment of stopping powers is applicable (see, e.g., the review by Bethe and Ashkin (45)), this variation comes only from the ratio of two logarithmic terms. As an example, using data summarized by Whaling (46), the stopping power ratio for protons at 1 Mev incident on a transition from aluminum to copper is about 1.59 and increases by 1.4 per cent of this value when the energy is raised to 1.1 Mev.

Where the terms of the product in the substitution 12a can be treated as independent of energy, they can all be evaluated at E_{20}, the emergent particle energy at the surface of the target. The substitution 12a then reduces to

$$\epsilon_2(E_{20}) \rightarrow \epsilon_{m+}(E_{20}) \tag{12b}$$

In other words, to this approximation, the result above for a uniform target is also valid for a step-wise uniform target, provided that $\epsilon_2(E_{20})$ is interpreted as the stopping power function evaluated for the material of the target lamina in which the reaction actually takes place, but at the energy with which the emergent particle leaves the surface of the target.

As this result is independent of the number of laminae involved, one would expect it to be also valid in the limit of a target of continuously varying composition. This is in fact the case; the approximation leading to the substitution 12b is equivalent to the assumption that the stopping powers in equation 4 may be written in the form $\epsilon(E,x) = e(E)f(x)$. If this approximation is used, equation 4 again becomes separable, and the calculation may be carried through essentially as before. The result confirms the conclusion above; in place of $\epsilon_2(E_{20})$ in equation 12 there appears $e(E_{20})f(s) = \epsilon_2(E_{20}, s)$. (The ratio $\epsilon_1(E_1)/\epsilon_2(E_2)$ must of course be interpreted as $\epsilon_1(E_1, s)/\epsilon_2(E_2, s)$.) As the atomic number densities involved appear in the form $n'(s)/n(s)$ even in an exact treatment, we see that the approximate yield depends on the composition of the target only at the lamina where the reaction takes place, the surface layers of the target serving only to modify the energies which must be inserted into the stopping power functions and the relation between the entering and emerging particle energies.

The Calculation of Profile Shapes. The yield calculated in equation 12 contains as free variables both the beam energy and the spectrometer setting in energy and angle. In the following calculations of profile shapes for various simple cases, we have a choice of either beam energy or spectrometer energy as the independent variable; which alternative is chosen generally depends on experimental conditions. Both cases will be illustrated and the general relations connecting the two modes of taking data will be derived.

To illustrate the effects of including finite spectrometer resolution

in angle as well as energy, we will now calculate the profile shape for the simple case where the variations of the cross section and the stopping-power terms in equation 12 are negligible, and the spectrometer has a simple rectangular resolution window in energy and angle. If we work sufficiently far from the poles, the $\sin\theta$ term in $d\Omega$ may be treated as a constant and equation 12 may be reduced to the form

$$Y = y_o \int_R dE_{20}\, d\theta \tag{13}$$

where the region of integration R is given by

$$R: \{ |\theta - \theta_o| \leq \delta\theta/2;\ |E_{20} - E_f| \leq \delta E/2;\ s \geq 0\} \tag{14}$$

The spectrometer window is centered at $E_{20} = E_f$ and $\theta = \theta_o$ with widths δE and $\delta\theta$, respectively. Figures 32(b) and (c) illustrate the region R in the spectrometer window, and the resultant yield as a function of $\Delta E_{1B} = E_{1B} - E_1(E_f, \theta_o)$, the difference between the actual bombarding energy and the spectrometer setting referred to the corresponding incoming particle energy by use of the inverse of equation 3. Other quantities of use are defined by $E_{2B} = E_2(E_{1B}, \theta_o)$, $\Delta\theta = \theta - \theta_o$, and $\Delta E_{20} = E_{20} - E_f$. The yield is just proportional to the area of the region R, giving a trapezoidally rising step with parabolically rounded corners. To calculate the dimensions a and b characterizing the shape as shown in fig. 32(c), we write the equation of the line $s = 0$ defining the target surface in the $\Delta E_{20} - \Delta\theta$ plane to first order:

$$\Delta E_{20} = \left(\frac{\partial E_2}{\partial E_1}\right)_\theta \Delta E_{1B} + \left(\frac{\partial E_2}{\partial \theta}\right)_{E_1} \Delta\theta \tag{15}$$

A simple calculation then shows that a and b are the larger and smaller,

respectively, of the two quantities

$$\left| \frac{\delta E}{\left(\frac{\partial E_2}{\partial E_1}\right)_\theta} \right| \quad \text{and} \quad \left| \frac{\left(\frac{\partial E_2}{\partial \theta}\right)_{E_1} \delta\theta}{\left(\frac{\partial E_2}{\partial E_1}\right)_\theta} \right| \tag{16}$$

For the data from the $C^{12}(He^3, p)N^{14*}$ experiment shown in fig. 22, δE is given by the spectrometer characteristics as $\delta E = E_f/231$ for the 1/8-inch collector slit used. From figs. 19 and 21, $\delta\theta$ is estimated at $(3.65 \pm 0.10)^\circ$. Using these data in equations 16 to calculate percentage resolutions in E_{1B}, we find 0.78 per cent and 1.39 per cent for the energy and angular contributions, respectively. The tangent line to the face of the profile drawn in fig. 22 rises in 1.35 per cent of the average incident energy. This agreement must be regarded as fortuitously good in view of the fact that the spectrometer window is not more than approximately square in either energy or angle, and the drawing of the tangent is subject to difficulties of both statistics and the vagaries of curve-drawing. Indeed, three similar profiles chosen at random yielded resolutions of 1.48 per cent, 1.44 per cent, and 1.48 per cent, indicating that the calculation is correct to about 5 per cent of the rise percentage.

We now wish to calculate the effects of the inclusion of variations of yield with energy and angle on this simple picture. If we retain the definition of the spectrometer resolution function given by equation 14, the functional dependences of the total yield Y and its differential $dY = y\, dE_{20} d\theta$ are given by the expressions

$$Y = Y(E_{1B}, E_f, \theta_o)$$

and

$$y = y(E_{1B}, E_{20}, \theta)$$

For the present purposes we treat θ_1 as a fixed parameter and the integral over ϕ as a multiplicative constant. In analogy to equation 13, we then have

$$Y = \int_R y \, dE_{20} \, d\theta \tag{17}$$

with equation 14 defining the region of integration as before.

The behavior of the plateau of the profile may be studied by formally removing the restriction $s \geq 0$ on region R, a procedure which permits calculation of the yield as extrapolated to the position of the step. If we now write y as a linear expansion about some given point, then a linear expansion also suffices for Y due to the symmetries of the limits of integration in equation 17:

$$y = y_o + y_1 \Delta E_{1B} + y_2 \Delta E_{20} + y_\theta \Delta\theta \tag{18a}$$

$$Y = Y_o + Y_1 \Delta E_{1B} + Y_2 \Delta E_f + Y_\theta \Delta\theta_o \, . \tag{18b}$$

With the relations

$$y_1 = (\partial y/\partial E_{1B})_{E_{20}, \theta} \qquad Y_1 = (\partial Y/\partial E_{1B})_{E_f, \theta_o}$$

$$y_2 = (\partial y/\partial E_{20})_{E_{1B}, \theta} \qquad Y_2 = (\partial Y/\partial E_f)_{E_{1B}, \theta_o}$$

$$y_\theta = (\partial y/\partial \theta)_{E_{1B}, E_{20}} \qquad Y_\theta = (\partial Y/\partial \theta_o)_{E_{1B}, E_f}$$

equation 17 and its derivatives may be used to connect the coefficients

of the two expansions in equation 18:

$$
\begin{aligned}
y_o &= Y_o/\delta E\delta\theta \\
y_1 &= Y_1/\delta E\delta\theta \\
y_2 &= (Y_2 - Y_o/E_f)/\delta E\delta\theta \\
y_\theta &= Y_\theta/\delta E\delta\theta
\end{aligned}
\tag{19}
$$

The term Y_o/E_f in y_2 arises from the fact that the δE in the limits of the E_{20} integral is assumed proportional to E_f, as is the case for most spectrometers. It is important to note here that Y and all its derivatives are simply proportional to $\delta E\delta\theta$ even in the presence of first-order variations of y, and hence that there is no correction to the yield at a point away from the step due to first-order variations of cross section or stopping powers across the spectrometer window.

An additional important and useful relation between the coefficients of these expansions results from the following considerations. As the cross section of the reaction $\sigma(E_1,\theta)$ is a function of only one energy, it is evident from an inspection of equation 12 that the second energy dependence of the integrand $y = y(E_{1B}, E_{20}, \theta)$ arises from the spectrometer transmission function $W(E_{20}, \theta)$ and the stopping cross section $\epsilon_2(E_{20})$. In the usual case where the energy dependences of these functions are either known or can be estimated, the additional information provided serves to eliminate one of the free coefficients in the expansion equation 18a.

The desired relation may be written in the general form

$$\left(\frac{\partial y}{\partial E_{20}}\right)_{E_1} = \left(\frac{\partial y}{\partial E_{1B}}\right)_{E_{20}} \left(\frac{\partial E_{1B}}{\partial E_{20}}\right)_{E_1} + \left(\frac{\partial y}{\partial E_{20}}\right)_{E_{1B}}$$

or

$$\left(\frac{\partial y}{\partial E_{20}}\right)_{E_1} = y_1 \left(\frac{\partial E_{1B}}{\partial E_{20}}\right)_{E_1} + y_2 \tag{20}$$

The quantity $(\partial E_{1B}/\partial E_{20})_{E_1}$ may be evaluated by differentiating equations 5a and 5b with respect to E_{20} with constant E_1 (and therefore constant E_2):

$$\left(\frac{\partial s}{\partial E_{20}}\right)_{E_1} = \frac{\cos \theta_1}{n\epsilon_1(E_{1B})} \left(\frac{\partial E_{1B}}{\partial E_{20}}\right)_{E_1}$$

$$\left(\frac{\partial s}{\partial E_{20}}\right)_{E_1} = -\frac{\cos \theta_2}{n\epsilon_2(E_{20})}$$

with the result

$$\left(\frac{\partial E_{1B}}{\partial E_{20}}\right)_{E_1} = -\frac{\epsilon_1(E_{1B})}{\epsilon_2(E_{20})} \frac{\cos \theta_2}{\cos \theta_1} \tag{21}$$

Under the assumption above that W is a constant out to the limits described by equation 14, the quantity $(\partial y/\partial E_{20})_{E_1}$ takes on a particularly simple form, which may be evaluated from equation 12:

$$\left(\frac{\partial y}{\partial E_{20}}\right)_{E_1} = -\frac{y}{\epsilon_2(E_{20})} \frac{d\epsilon_2(E_{20})}{dE_{20}} \tag{22}$$

Combining equations 20, 21, and 22, we may write the final result

$$y_2 = \frac{\epsilon_1(E_{1B})}{\epsilon_2(E_{20})} \frac{\cos \theta_2}{\cos \theta_1} y_1 - \frac{y_o}{\epsilon_2(E_{20})} \frac{d\epsilon_2(E_{20})}{dE_{20}} \tag{23}$$

or, by application of equations 19:

$$Y_2 = \frac{\epsilon_1(E_{1B})}{\epsilon_2(E_f)} \frac{\cos\theta_2}{\cos\theta_1} Y_1 + \left[\frac{1}{E_f} - \frac{d\epsilon_2(E_f)}{\epsilon_2(E_f)dE_f} \right] Y_o \qquad (24)$$

These equations justify the assumption used above that either the spectrometer setting E_f or the beam energy E_{1B} is an acceptable independent variable for a yield profile, and provide the explicit connection between the two modes of taking such profiles.

We are led to an additional convenient relation by our inspection of equation 12, which also shows that the calculation of $Y_1 = (\partial Y/\partial E_{1B})_{E_f}$ may be facilitated by treating the yield Y as a function of E_1 and E_f, giving

$$Y_1 = \left(\frac{\partial Y}{\partial E_1}\right)_{E_f} \left(\frac{\partial E_1}{\partial E_{1B}}\right)_{E_{20}} \qquad (25)$$

It is expected that $(\partial Y/\partial E_1)_{E_f}$ may be calculated with convenient directness from equation 12, while the value of the factor $(\partial E_1/\partial E_{1B})_{E_{20}}$ may be obtained from the relation

$$\left(\frac{\partial E_1}{\partial E_{20}}\right)_{E_{1B}} = - \left(\frac{\partial E_{1B}}{\partial E_{20}}\right)_{E_1} \left(\frac{\partial E_1}{\partial E_{1B}}\right)_{E_{20}}$$

This last relation is a consequence of the functional dependence of E_1 on E_{1B} and E_{20}. Combining equations 10 and 21 with this expression, we have

$$\left(\frac{\partial E_1}{\partial E_{1B}}\right)_{E_{20}} = \frac{\epsilon_2(E_2)}{\epsilon_1(E_{1B})} \left[\frac{\epsilon_2(E_2)}{\epsilon_1(E_1)} + \frac{\cos\theta_2}{\cos\theta_1} \left(\frac{\partial E_2}{\partial E_1}\right)_\theta \right]^{-1} \qquad (26)$$

Additional similar relations may be obtained as desired from the remaining partial derivatives of equations 5. It should be noted, however, that the θ derivatives of equations 5 will involve terms linear in the target depth parameter s.

An interesting case in which the θ derivatives arise is that of the yield from a narrow resonance in the cross section. If the cross section is approximated by a delta function, and all other variations with energy and angle in the integrand are considered negligible, equation 12 may be reduced to

$$Y = y_o \int_R dE_{20}\, d\theta\, \delta(E_1 - E_R)$$

where E_R is the resonance energy, and the region of integration R is defined by equation 14 as before. The effect of the delta function is to restrict contributions to the yield to the intersection of region R with the line in the ΔE_{20}- $\Delta\theta$ plane which is defined for any given value of E_{1B} and E_f by the requirement $E_1 = E_R$. In analogy to equation 15 for the line $s = 0$, we may write the first order equation of the line $E_1 = E_R$ as

$$\Delta E_{20} = \left(\frac{\partial E_{20}}{\partial E_1}\right)_{E_{1B},\theta} \Delta E_R + \left(\frac{\partial E_{20}}{\partial E_{1B}}\right)_{E_1,\theta} \Delta E_{1B} + \left(\frac{\partial E_{20}}{\partial \theta}\right)_{E_1, E_{1B}} \Delta\theta$$

by making use of the functional relationship between E_{20}, E_{1B}, E_1 and θ. The origin of this expansion is the point $E_{1B} = E_1(E_f, \theta_o)$, $E_{20} = E_f$, $\theta = \theta_o$, as before, and the quantity $\Delta E_R = E_R - E_1(E_f, \theta_o)$ is the resonance energy referred to the same origin. The first two partial derivatives in the expansion are the reciprocals of those given in equa-

tions 10 and 21, respectively, and the third may be obtained by differentiating equations 5 with respect to θ with constant E_1 and E_{1B}, giving

$$\left(\frac{\partial E_{20}}{\partial \theta}\right)_{E_1, E_{1B}} = ns\epsilon_2(E_{20}) \frac{\tan \theta_2}{\cos \theta_2} + \frac{\epsilon_2(E_{20})}{\epsilon_2(E_2)} \left(\frac{\partial E_2}{\partial \theta}\right)_{E_1}$$

As $s = 0$ at the origin of the present expansion, the term proportional to s is of course to be neglected; it is important only at considerable depths in the target.

It is obvious that if the beam energy equals the resonance energy, $E_{1B} = E_R$, the yield from the reaction comes only from the surface of the target, and hence the line $E_1 = E_R$ must coincide with the line $s = 0$ under these conditions. A comparison of the above relations with equation 15 shows that this is indeed the case for $\Delta E_{1B} = \Delta E_R$. It is now easy to show that the yield as a function of E_{1B} takes the form of a symmetrical trapezoid modified by an abrupt cutoff as the beam energy falls below the resonance energy. The width of the trapezoid at half-maximum and the width of its rising or falling sections are given by the larger and smaller, respectively, of the two quantities

$$\left|\left(\frac{\partial E_{1B}}{\partial E_{20}}\right)_{E_1, \theta} \delta E\right| \quad \text{and} \quad \left|\left(\frac{\partial E_{1B}}{\partial E_{20}}\right)_{E_1, \theta} \left(\frac{\partial E_{20}}{\partial \theta}\right)_{E_1, E_{1B}} \delta\theta\right|$$

These resolutions should be compared with the resolutions obtained in equation 16 for the face of the yield profile when the cross section is constant.

Typical Yield Variations on the Plateau. It is of interest for orientation purposes to examine typical behaviors for the functions in equation 24. The second term on the right in this equation may be written in the form $(1 + \xi)Y_o/E_f$, where the parameter ξ is independent of the cross section for the reaction and can be shown to have very slow variation with energy for energies which are not too low. A survey of the stopping power curves given by Whaling (46) shows that the increase of ξ over the energy range from 1 Mev to 5 Mev for protons is of the order of 0.1 to 0.2 for a wide selection of targets, while the average values of ξ over the same energy range vary from about 0.8 for He targets to 0.5 for Au targets. Hence the behavior of this term of equation 24 is expected to be quite stable over a very wide variety of cases.

The first term on the right in equation 24 depends in a more complicated way on both the cross section of the reaction and the stopping powers. However, some insight is produced by a discussion of the particularly simple form which results for the case of elastic scattering. Under the assumption above that the energy is not too low, an investigation of the term in the square brackets in the denominator of equation 12 shows that its variation with E_1 is very slow for elastic scattering, and hence the variation of the yield with beam energy is almost entirely due to the variation of the scattering cross section with energy. If we take the Rutherford cross section as an example, set $\theta_1 = \theta_2$ and $(\partial E_2/\partial E_1)_\theta = E_2/E_1 = \alpha^2$, and take $\xi = -E\, d\epsilon/\epsilon(E)\, dE$ as a constant characterizing the stopping power functions $\epsilon_1(E) = \epsilon_2(E)$, equation 24 may be reduced to

$$\frac{Y_2 E_f}{Y_o} = -\frac{2}{1+\alpha^{-2(1+\xi)}} + (1+\xi) \qquad (27)$$

Here we have used the relations $\partial\sigma/\partial E_1 = -2\sigma/E_1$ and $\epsilon(E_2)/\epsilon(E_1) = \alpha^{-2\xi}$. As is proper for use in the expansions of equations 18, we have also set $E_2 = E_f$ and $E_{1B} = E_1$. The result is written so that the two terms shown in equation 27 correspond directly to the two terms of equation 24.

As the magnitude of the first of these terms cannot be greater than one, it is evident that the second term must dominate. In fact, an expansion of equation 27 for $\alpha \to 1$ yields $Y_2 E_f / Y_o \cong \xi + (1-\alpha)(1+\xi)$, with the interesting result that the typical slope of the plateau for Rutherford scattering plotted versus spectrometer energy setting is only slightly greater than the variation of the stopping cross section with energy, and is in fact primarily determined by that variation.

It is of interest to compare this calculation with the corresponding results for the slope of the profile versus the beam energy. In a similar fashion to the above, we obtain

$$\frac{Y_1 E_{1B}}{Y_o} = -\frac{2}{1+\alpha^{2(1+\xi)}}$$

In contrast to the slope versus spectrometer setting, this quantity is negative and somewhat greater than one in magnitude, and its dependence on the stopping power is quite weak.

Profile Face Curvatures and Corrections to Energy Measurements.

The above calculations are all concerned with the plateau of the yield

profile, and result from the removal of the restriction $s \geq 0$ in equation 12. If we now return to our consideration of the shape of the profile face, this restriction is once more necessary. The expansion for y assumed in equation 18a is of course unaffected, but now linear variations in y require terms up to cubic for the expansion of Y in equation 18b. A sketch illustrating features which may be expected in the resulting profile is shown in fig. 32(d). Relations similar to equations 19 applicable to the region of the step may, of course, be calculated to display the cubic terms appearing in the shape of the profile face. However, this is rather tedious and not particularly illuminating, so we will confine ourselves to calculating the value of the yield when the spectrometer energy E_f is centered on E_{2B}, which is the critical setting for the measurement of nuclear reaction energies.

In order to perform this calculation, we choose the origin of the expansion of y in equation 18a in accord with the earlier definitions of the variables, so that $\Delta E_{1B} = \Delta E_{20} = 0$ at $E_{20} = E_{2B} = E_f$, and $\Delta\theta = 0$ at $\theta = \theta_o$. We may obtain values for y and its derivatives at this origin either by direct calculation from the explicit form of y from equations 12 and 17, using known or assumed values for the dependences of cross section and stopping powers on energy and angle, or by extrapolation of measurements of the total yield Y and its derivatives from outside the region of the step, where equations 19 are valid. We will take the latter course for the present treatment.

Since $\Delta E_{1B} = 0$ when $E_f = E_{2B}$, equation 15 for the line $s = 0$ becomes

$$\Delta E_{20} = \left(\frac{\partial E_2}{\partial \theta}\right)_{E_1} \Delta\theta \qquad (15a)$$

If we define

$$\nu = -\left(\frac{\partial E_2}{\partial \theta}\right)_{E_1} \frac{\delta\theta}{\delta E} = \frac{1}{\mu}$$

for the case $0 \leq \mu \leq 1$ the integral in equation 17 may be written

$$Y_\mu = \int_{-\delta E/2}^{\delta E/2} d\Delta E_{20} \int_{-\delta\theta/2}^{-\mu\Delta E_{20}\delta\theta/\delta E} d\Delta\theta (y_o + y_\theta \Delta\theta + y_2 \Delta E_{20}) \qquad (17a)$$

or

$$Y_\mu = \frac{\delta\theta\delta E}{2}\left[y_o \mp \frac{1}{4}\left(1 - \frac{\mu^2}{3}\right) y_\theta \delta\theta \mp \frac{\mu}{6} y_2 \delta E \right] \quad 0 \leq \pm\mu \leq 1 \qquad (28)$$

where the case $-1 \leq \mu \leq 0$ has been included by means of the lower signs. Inserting the values of y and its derivatives obtained by extrapolation of observations made away from the step (equations 19), we have

$$Y_\mu = \frac{1}{2}\left[Y_o \mp \frac{1}{4}\left(1 - \frac{\mu^2}{3}\right) Y_\theta \delta\theta \mp \frac{\mu}{6}\left(Y_2 - \frac{Y_o}{E_f} \right) \delta E \right] \quad 0 \leq \pm\mu \leq 1 \qquad (29)$$

Note the presence of the extra terms in δE and $\delta\theta$ in the last two equations. It is evident that these terms represent corrections to the usual assumption that $\Delta E_{1B} = 0$ where the yield reaches $Y = Y_o/2$, half the value extrapolated from the plateau.

Similar calculations for the case $|\nu| \leq 1$ give the result

$$Y_\nu = \frac{1}{2}\left[Y_o - \frac{1}{4}\left(1 - \frac{\nu^2}{3}\right)\left(Y_2 - \frac{Y_o}{E_f} \right) \delta E - \frac{\nu}{6} Y_\theta \delta\theta \right] \quad |\nu| \leq 1 \qquad (29a)$$

If $\nu = 0$, this last result is seen to be similar to the correction derived

by Brown, et al. (27).

For the conditions under which the $C^{12}(He^3, p)N^{14*}$ Q-value was measured, $\delta\theta = 3.65^o$, $\delta E = E_f/231$, and measurements showed that $Y_2 E_f \cong -6.1\, Y_o$, with Y_θ estimated at about the order of $-0.007\, Y_o$ per degree. Combining this information with the kinematics of the reaction, we find that $\mu = 0.745$. Then from equation 29, $Y_\mu = 1.0088\, Y_o/2$, indicating that the choice of the half-way point on the rise of the profile is just slightly in error. When converted to an error in E_{1B} by use of the measured rate of rise of the profile, this corresponds to an error of 0.006 per cent, or about 170 ev. In this case, the correction is trivial, but one may expect sizeable corrections whenever either $Y_\theta \delta\theta$ or $Y_2 \delta E$ becomes significant in comparison to Y_o. Such rapid variations in yield as may result from the presence of resonances or stripping patterns, for example, should therefore be avoided in Q-value measurements.

The accuracy of the above estimate is seriously reduced by the fact that $Y_\theta = (\partial Y/\partial\theta_o)_{\theta_1}$ had to be computed from the measured value of $(\partial Y/\partial\theta_o)_{\theta_2}$, which was $-0.039\, Y_o$ per degree. From equation 12 we find

$$\frac{1}{Y}\left(\frac{\partial Y}{\partial \theta_2}\right)_{\theta_o} = -\left[\frac{\cos\theta_1}{\cos\theta_2} + \frac{\epsilon_1(E_1)}{\epsilon_2(E_2)}\left(\frac{\partial E_2}{\partial E_1}\right)_\theta\right]\left[\frac{\sin\theta_1}{\cos\theta_2} + \frac{\cos\theta_1 \sin\theta_2}{\cos^2\theta_2}\right]$$

$$\cong -0.032 \text{ per degree,}$$

and hence

$$Y_\theta = \left(\frac{\partial Y}{\partial \theta_o}\right)_{\theta_1} = \left(\frac{\partial Y}{\partial \theta_o}\right)_{\theta_2} - \left(\frac{\partial Y}{\partial \theta_2}\right)_{\theta_o} \approx -0.007\, Y_o/\text{degree.}$$

The ratio of the stopping powers was estimated using the usual theoretical formula for higher energies (45).

Comparison With Experiment. The goodness of fit of the present theory to the rising face of the profile was shown above and in fig. 22. Figure 33 shows a comparison of the theoretical curves for the plateau with experiment. The experimental points are the yield of Rutherford scattering for protons on copper as taken by J. A. McCray. The two theoretical curves shown were calculated from the present treatment and from the formula of Brown, Snyder, Fowler, and Lauritsen (27). As is shown, the newer theory predicts the Rutherford yield within 5 per cent even after proton energy losses of more than a factor of two in the target. It is possible that neglected effects, such as straggling or multiple scattering, may contribute to the residual error. On the other hand, the approximations used in the calculations may have introduced errors of the order of 2 per cent, and the assignment of the whole discrepancy to the stopping power curve (46) would not be unreasonable in view of the scatter of experimental points around this curve. It would be interesting to try to pin down the error with more refined calculations and better data.

Conclusions. The theory of thick target yields has been developed in a form permitting precise calculations of yields over wide ranges of experimental conditions. Present limitations on the accuracy of the calculated yields appear to lie principally in the accuracy of our knowledge of stopping cross sections.

APPENDIX C

Q-Value Formulas and Corrections

The usual simple analysis of electrostatic and magnetic deflection systems indicates that the energies of particles passing through the electrostatic analyzer and magnetic spectrometer should be given by the equations

$$E_e = k_e Z V_e (1 + E_e/2Mc^2) \tag{1}$$

$$E_m = \frac{k_m Z^2 M_p}{V_m^2 M} (1 - E_m/2Mc^2) \tag{2}$$

respectively, where Z and M refer to the actual charge and mass of the particle or ion passing through the field of the instrument in question, V_e and V_m are the respective readings of the measuring potentiometers, the $E/2Mc^2$ terms are the first order relativistic corrections, and k_e and k_m are the calibration constants.

Unfortunately, one must in general expect the equipment to be afflicted with various instrumental nonlinearities, which ideally would appear in the above equations as Taylor series expansions of the constants k in the variables E, Z, and M of the particle, the coefficients of the series being experimentally determined. Practically, one is forced to make assumptions as to the probable forms of the corrections in order to limit the number and accuracy of the required experiments. In the present case, one presumes that since the magnetic spectrometer is operated here at constant field, no corrections to equation 2 need be considered. In the case of the electrostatic analyzer,

the two obvious possibilities for nonlinearity are the presence of magnetic field in the analyzer, assumed small because of the surrounding magnetic shielding, and the presence of thermal drifts proportional to V^2/R in the measuring voltage dividers on the power supply. As the behavior of the analyzer before the installation of the power supply box heat exchanger was in fact suggestive of thermal drifts, a correction of the form $(1 + CV_e^2) \equiv (1 + \gamma E_e^2/Z^2)$ will be included in equation 1, with the coefficient γ determined from experiment. Hence we have

$$E_e \equiv k_e Z V_e (1 + E_e/2Mc^2 + \gamma E_e^2/Z^2) \tag{1a}$$

We now wish to calculate explicit formulas for the Q-values of the $C^{12}(He^3, p)N^{14*}$ and $C^{12}(He^3, n)O^{14}$ experiments in terms of the various experimentally found values of V_e and V_m, including all the small corrections for such effects as the target potential V_t and the energy of extra electrons, etc., in ionic or molecular-ion beams.

The equations of the kinematics of nuclear reactions are given in the paper of Brown, et al. (27):

$$Q \equiv \frac{M_3 + M_2}{M_3} E_2 - \frac{M_3 - M_1}{M_3} E_1 - \frac{2(M_1 M_2)^{1/2}}{M_3} \cos\theta (E_1 E_2)^{1/2} \tag{3}$$

and, for elastic scattering:

$$E_2 \equiv a^2 E_1$$

$$a \equiv \frac{(M_1 M_2)^{1/2}}{M_2 + M_3} \cos\theta + \left[\frac{M_3 - M_1}{M_2 + M_3} + \frac{M_1 M_2 \cos^2\theta}{(M_2 + M_3)^2} \right]^{1/2} \tag{4}$$

$$\frac{1}{E_1}\frac{\partial E_2}{\partial \theta} = 2a\frac{\partial a}{\partial \theta} = -\frac{2a(M_1M_2)^{1/2}\sin\theta}{M_2 + M_3 - a(M_1M_2)^{1/2}\cos\theta} \qquad (5)$$

Throughout these equations, relativistic corrections are made by using effective masses of the form $M_{eff} = M_o + E/2c^2$. In accordance with the conclusions of R. F. Christy (47), nuclear masses are used in the calculations below for all particles, except in the case of $Au^{197}(d, d)$ scattering, where the inner electrons are tightly enough bound to follow the gold nucleus as it recoils from the collision. Here the mass of the $Au^{197}(20+)$ ion was used on the basis of a crude estimate of the proper degree of ionization.

The experimental determination of Q_p for the $C^{12}(He^3, p)N^{14*}$ reaction involves the reactions (a) $Li^7(p, n)Be^7$ (threshold determination), (b) $Au^{197}(d, d)Au^{197}$ elastic scattering, and (c) $C^{12}(He^3, p)N^{14*}$. The electrostatic analyzer readings V_e arrived at in the three reactions will be denoted by T_1, T_2, and T_3, respectively, the common value of V_m used in reactions (b) and (c) will be called A, and the common laboratory angle of observation in (b) and (c) will be denoted by θ or θ^o in radians or degrees, respectively. We further define R_1, R_2, and R_3 such that the true value of the $Li^7(p, n)Be^7$ threshold energy is $1.8807\,R_1$ Mev, $R_2 = T_2/T_1$, and $R_3 = T_3/T_1$. The experimental conditions are then such that $\theta^o \cong 150^o$, $R_2 \cong 1$, and $R_3 \cong 1.42$. The present best value (24) for R_1 is 1.0000, and it will be shown that R_1 is an approximate factor in all results obtained, indicating that corrections for future revisions of the Li^7 calibration point may be made by simple multiplicative scaling of the results.

Reaction (a) is used as the primary calibration of the electrostatic analyzer. Solving equation 1 for k_e, we have to first order in the correction terms:

$$k_e = (E/V_e)(1 - E/2M_pc^2 - \gamma E^2) \qquad (6)$$

into which we may put the energy of the protons passing through the analyzer at the threshold $E = 1.8807R_1 + V_t$, $V_e = T_1$, and the target potential $V_t = +300$ ev. The result is

$$k_e \cong 1.87912(R_1/T_1)(1 - 3.537\gamma) \qquad (6a)$$

The elastic scattering (b) is now used to obtain the value of k_m/A^2 from the above calibration. The energy of the deuterons immediately after scattering is $E_2 = \alpha^2 E_1$, where α^2 may be written in the form of an expansion to first order around $\theta^o = 150^o$ with the aid of equations 4 and 5 and the appropriate effective masses:

$$\alpha^2 \cong 0.962545 - 0.009817(\theta - 5\pi/6)$$

E_1 is of the form

$$E_1 = k_e T_2(1 + E_1/2M_dc^2 + \gamma E_1^2) - V_t$$

$$E_1 \cong 1.87975 R_1R_2$$

Hence, near $\theta = 5\pi/6$,

$$E_2 \cong (1.80934 - 0.01851(\theta - 5\pi/6))R_1R_2$$

Note that the correction term in γ vanishes in these last two relations due to the fact that $T_1 \cong T_2$. Equation 2 now gives

$$k_m/A^2 = (M_d E_2'/M_p)(1 + E_2'/2M_d c^2)$$

with $E_2' = E_2 + V_t$, or

$$k_m/A^2 \cong (3.61923 - 0.03702(\theta - 5\pi/6))R_1 R_2$$

The values of E_1 and E_2 for the $C^{12}(He^3, p)N^{14*}$ reaction are now given by

$$E_1 = [k_e T_3(1 + E_1/2M_+ c^2 + \gamma E_1^2) - V_t] M_{++}/M_+ \qquad (7)$$

$$E_1 \cong 1.87945 R_1 R_3(1 + 3.623\gamma)$$

$$E_2 = (k_m/A^2)(1 - E_2/2M_p c^2) - V_t$$

$$E_2 \cong 3.61197 R_1 R_2(1 - 0.010198(\theta - 5\pi/6))$$

where M_+ and M_{++} are the masses of He^{3+} and He^{3++}, respectively. Inserting these results in equation 3, we have the desired Q-value equation for the $C^{12}(He^3, p)N^{14*}$ reaction including all corrections:

$$Q_p/R_1 \cong 3.87230 R_2 - 1.47459 R_3 + 0.56231(R_2 R_3)^{1/2}$$

$$+ 0.00603(\theta^o - 150^o) - 6.366\gamma$$

For the $C^{12}(He^3, n)O^{14}$ threshold and Q-value, we define in addition to the above quantities the electrostatic analyzer setting corresponding to the threshold energy E_{th} as $V_e = T_4$, and $R_4 = T_4/T_1$. The Q-value equation now appears in somewhat different form from equation 3:

$$Q_n = - M_0 E_{th}/(M_0 + M_1 - Q_n/2c^2)$$

This form results from the insertion in equation 3 of the correct expression for the energy of the emerging neutrons at threshold and rearranging the resulting expression. The relativistic correction term $Q_n/2c^2$ is shown explicitly in this expression by making use of the relation $M_0 + M_1 = M_2 + M_3 + Q/c^2$; the masses used should therefore be the true nuclear masses rather than the effective masses used above. Inserting values gives the result

$$Q_n \cong - 0.799128\, E_{th}$$

In analogy to equation 7, we have

$$E_{th} = [k_e T_4(1 + E_{th}/2M_+c^2 + \gamma E_{th}^2) - V_t]\, M_{++}/M_+$$

Applying the calibration (equation 6a), and inserting values,

$$E_{th} \cong 1.878829\, R_1 R_4(1 - 1.469\,\gamma)$$

$$Q_n \cong -1.501425\, R_1 R_4(1 - 1.469\,\gamma)$$

which is the desired result.

The constant γ, representing a temperature coefficient of the electrostatic-analyzer voltage-measuring dividers as described above, was evaluated from the results of the $Al^{27}(p, \gamma)Si^{28}$ linearity check experiment discussed in Part III D. Within the experimental errors, and under the assumption put forth concerning the molecular-ion effect in that discussion, γ was found to be zero after the instal-

lation of the heat exchanger on the analyzer power-supply box; hence no correction was applied to the $C^{12}(He^3, n)O^{14}$ data or to Set II of the $C^{12}(He^3, p)N^{14*}$ data. Previous to the heat-exchanger installation, the value of γ was found to be rather erratic due to the presence of long-term thermal drifts. An estimated average value $\gamma = (1.1 \pm 1.2) \times 10^{-4}/Mev^2$ was therefore used in the analysis of Set I of the $C^{12}(He^3, p)N^{14*}$ data.

Figure 1: Schematic diagram of the four-way gas-handling system in the terminal of the 3-Mev accelerator. The Pirani gauge for monitoring the ion-source pressure is indicated by the letter V, and the gas-supply Bourdon gauges are indicated by P. The details of the four-way selector valve and the needle valve are shown in figs. 2 and 3. See text p. 6.

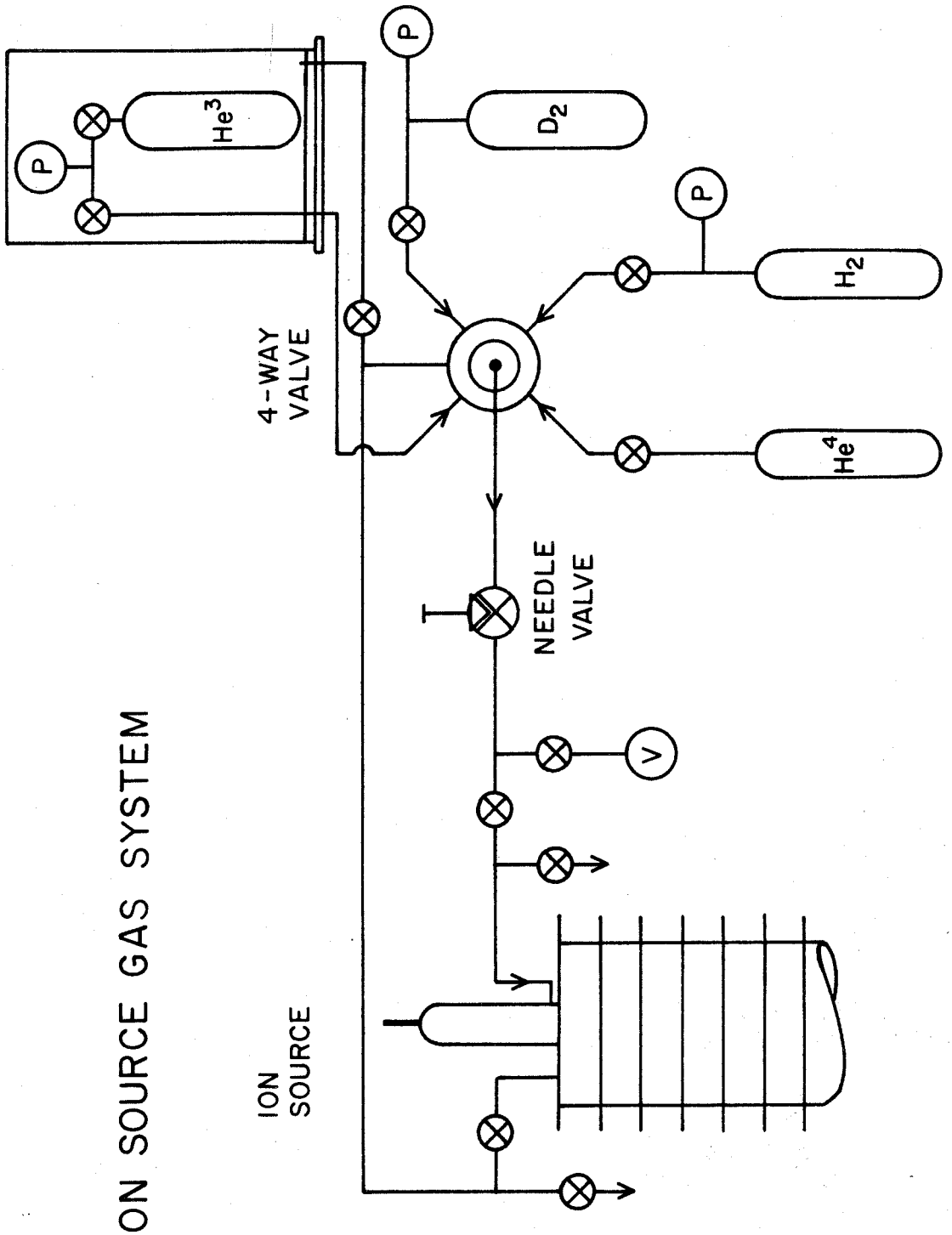
ION SOURCE GAS SYSTEM
ION SOURCE
NEEDLE VALVE
4-WAY VALVE
P
V
He^3
D_2
H_2
He^4

Figure 2: The four-way gas selector valve. The scavenging line connected to the space between valve rotor and stator eliminates the possibility of leakage between the gas supplies and disposes of the gas remaining in the output line when switching gases. See fig. 1 and text p. 6.

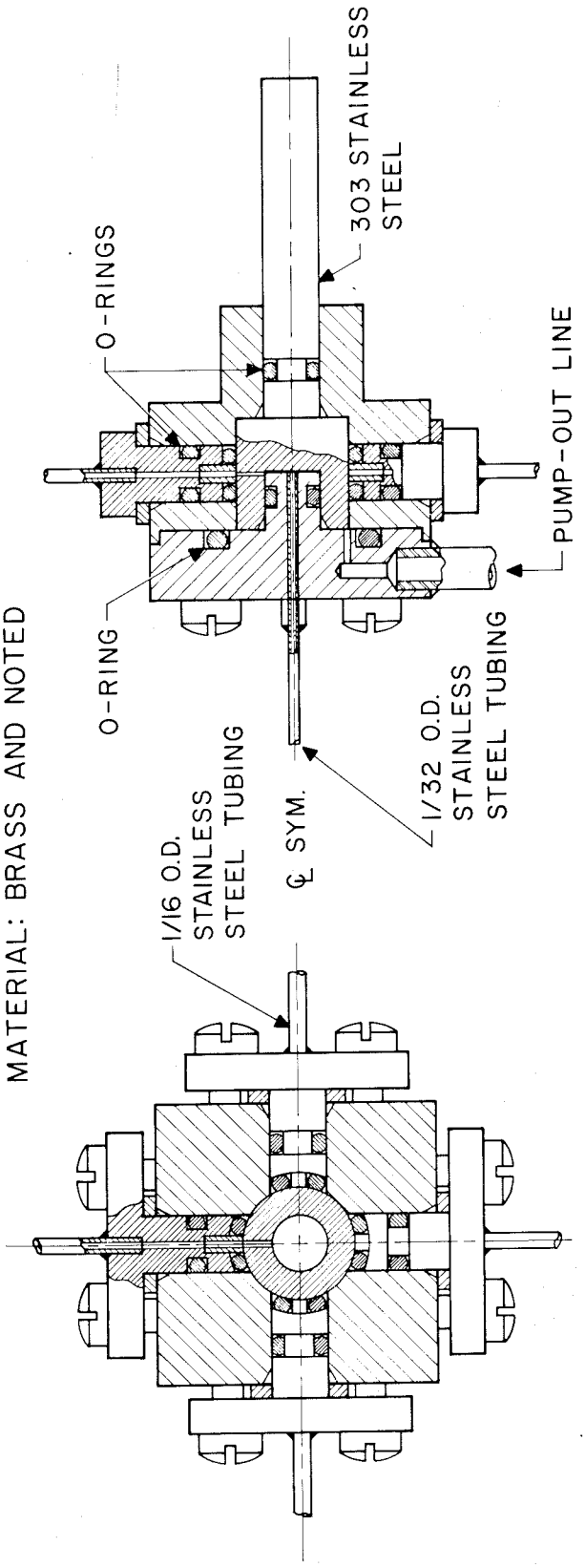

4-WAY GAS VALVE

Figure 3: The differential-screw needle valve. The keyed nut at the shaft end of the differential screw protects the needle and valve seat against excessive tightening; a fixed maximum closure pressure is provided by the spring. See text p. 6.

Figure 4: Schematic diagram of the regulator circuit for the electrostatic-analyzer voltage. The shielding indicated by the dotted lines was installed to prevent saturation of the differential DC amplifier by AC pickup from the main power transformer. See text pp. 8-9 .

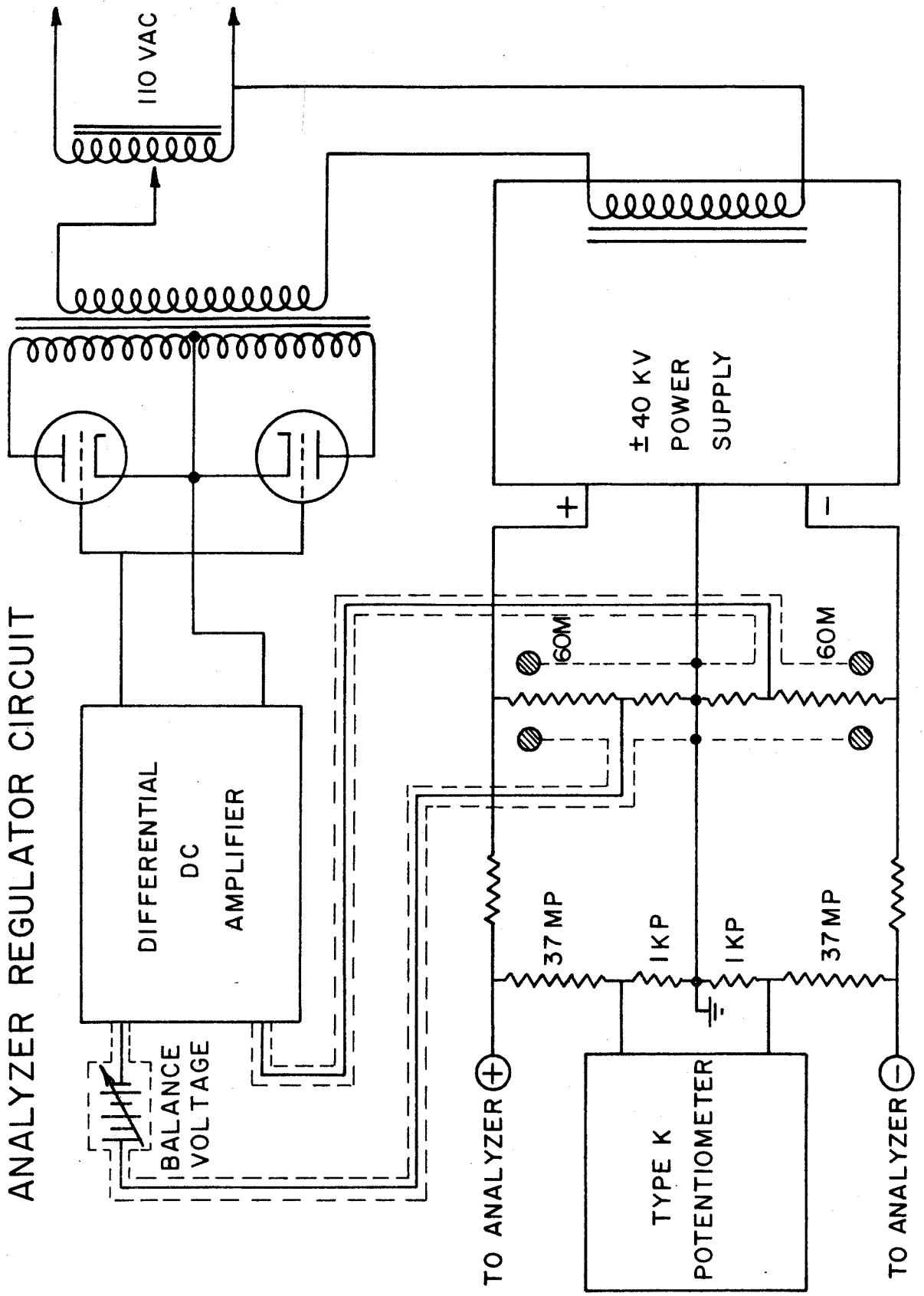
ANALYZER REGULATOR CIRCUIT
110 VAC
± 40 KV POWER SUPPLY
+
-
60M
60M
DIFFERENTIAL DC AMPLIFIER
BALANCE VOLTAGE
37 MP
1 KP
1 KP
37 MP
TO ANALYZER
TYPE K POTENTIOMETER
TO ANALYZER

Figure 5: Sectional schematic of the 16-inch magnetic spectrometer showing the positions of target and detector, and also the location of the fluxmeter coil on the central ray of the spectrometer. The details of the fluxmeter are shown in figs. 27 and 28. See text p. 10.

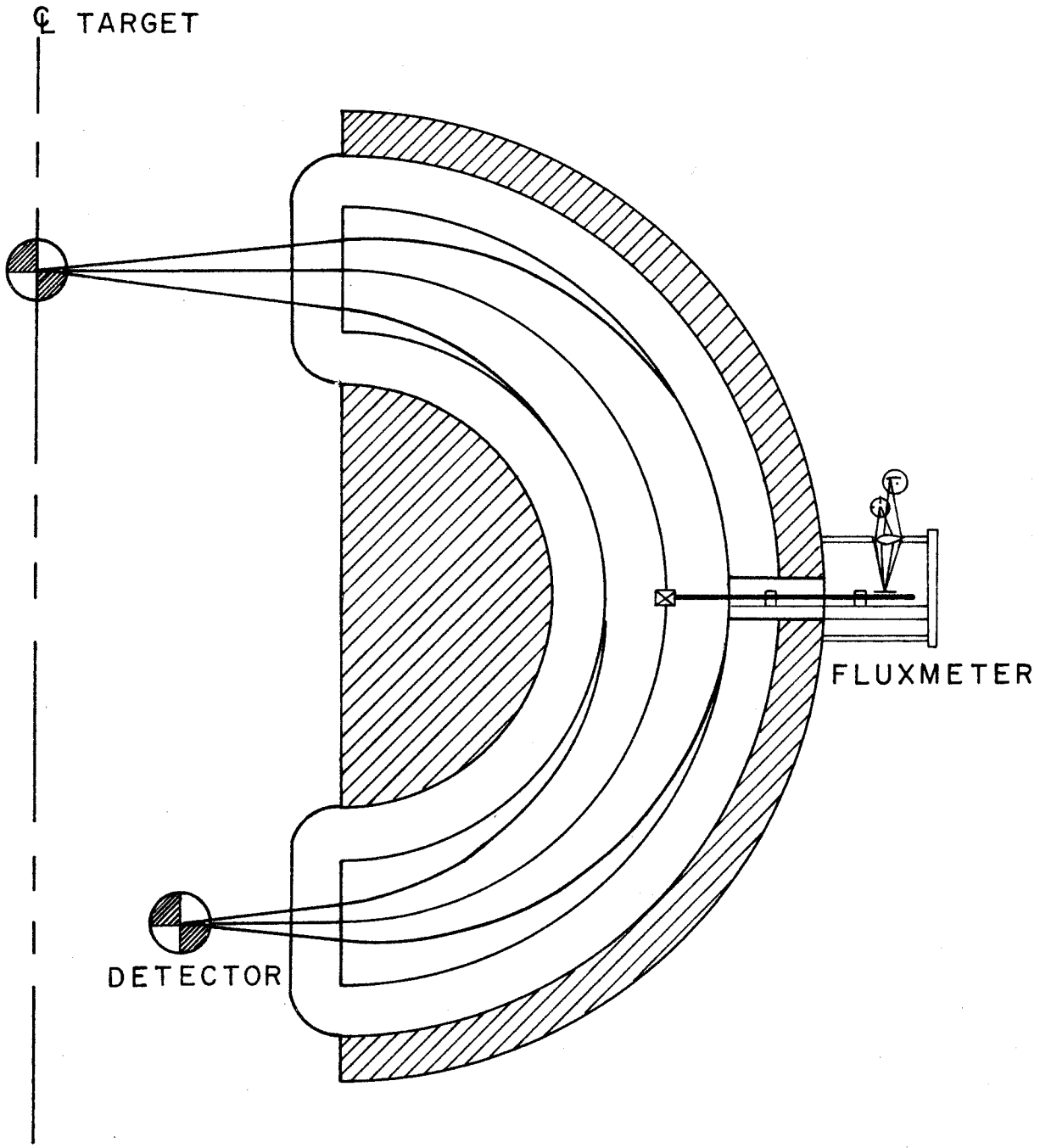

SPECTROMETER AND FLUXMETER
SCHEMATIC

Figure 6(a), (b): Schematic of the original type of fluxmeter viewed in section along the axis of rotation, showing the variation of the effective radius arm R with position of the needle in the bearing cup. (c), (d): Sectional view of the new type fluxmeter bearing, illustrating the independence of the radius arm of the position of the stylus on the bearing plate. (e): Illustration of the method of rocking the fluxmeter arm to center the stylus in its fences. See text pp. 11 and 54 ff.

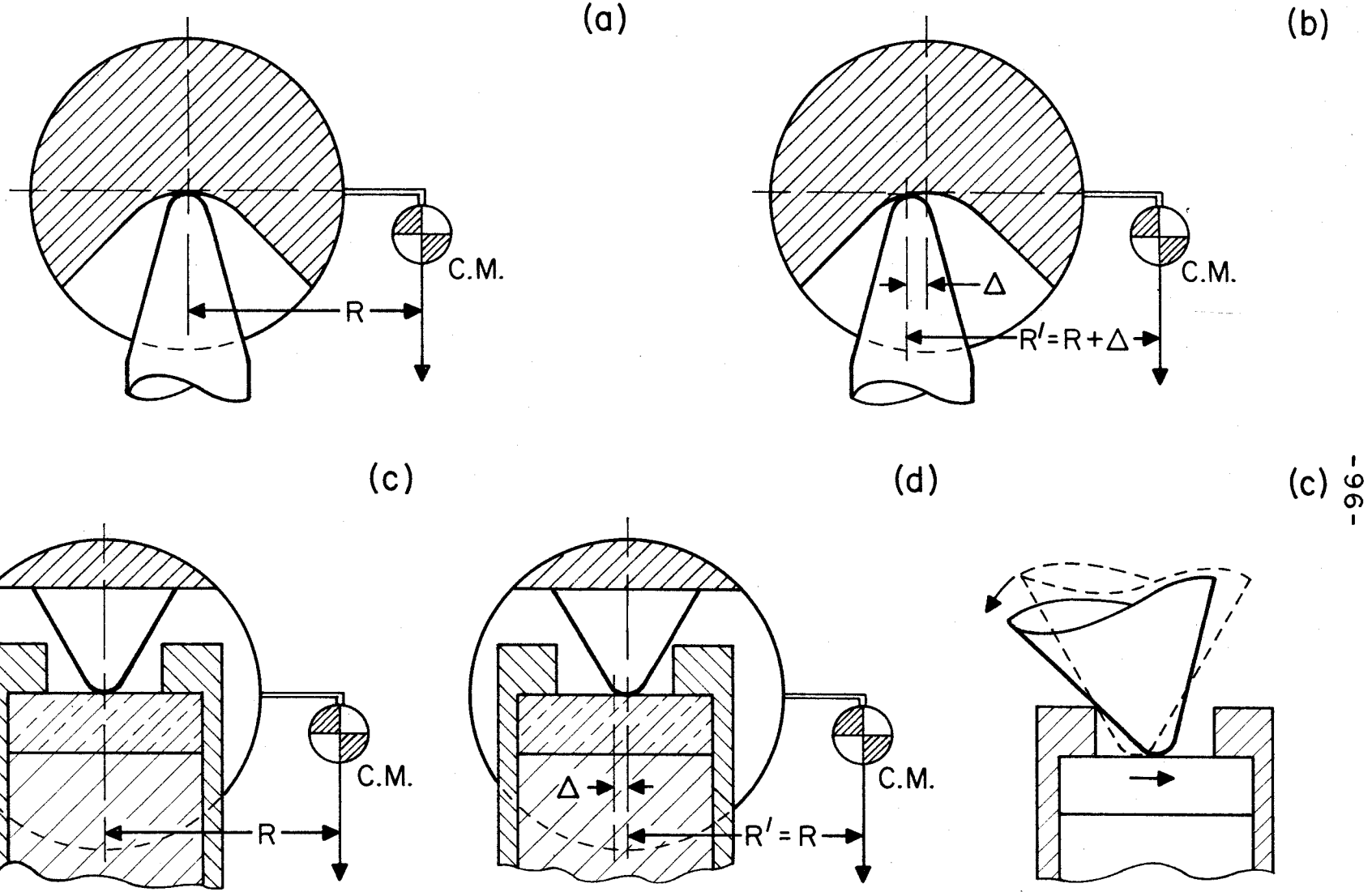

FLUXMETER BEARING OPERATION

Figure 7: The magnetic spectrometer setting in terms of effective proton energy versus the incident beam energy for the $C^{12}(He^3, p)N^{14*}$ (2.311-Mev state) reaction and various scattering processes, illustrating the use of the known kinematics of $Au^{197}(d, d)Au^{197}$ elastic scattering to transfer the 1.88-Mev Li^7 calibration point of the electrostatic analyzer to the spectrometer at 3.62 Mev proton energy. See text p. 12.

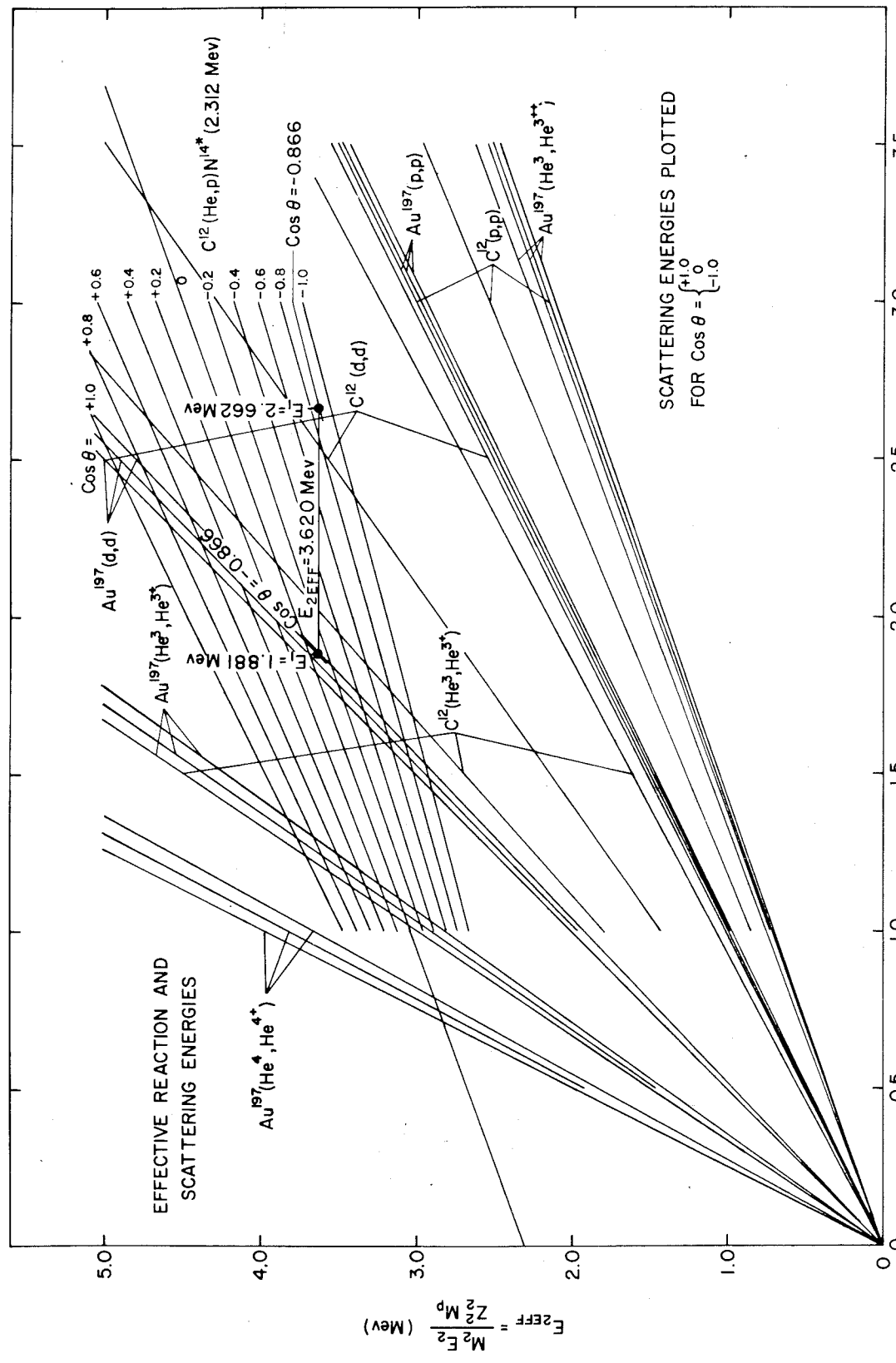
EFFECTIVE REACTION AND
SCATTERING ENERGIES
SCATTERING ENERGIES PLOTTED
FOR Cos θ = {+1.0 0 -1.0
Au197(d,d)
Au197(He3,He3+)
Au197(He4,He4+)
C12(d,d)
C12(He3,He3+)
C12(He,p)N14* (2.312 Mev)
Au197(p,p)
C12(p,p)
Au197(He3,He3+)
Cos θ =
+1.0
+0.8
+0.6
+0.4
+0.2
0
-0.2
-0.4
-0.6
-0.8
-1.0
Cos θ = -0.866
E1 = 2.662 Mev
E1 = 1.881 Mev
E2EFF = 3.620 Mev
E2EFF = M2 E2 / Z2 M1 (Mev)
E1 (Mev)
0
0.5
1.0
1.5
2.0
2.5
3.0
3.5
1.0
2.0
3.0
4.0
5.0

Figure 8: The arrangement of the neutron scintillator assembly showing the geometry of the target, moderator and scintillator as mounted in the continuously-variable-angle target chamber. This arrangement was used for checking the characteristics of the scintillator, and would be the normal experimental arrangement of the scintillator for precise neutron threshold work in the absence of such special considerations as the present restriction on spectrometer angle setting. See text pp. 13 f and 27 ff.

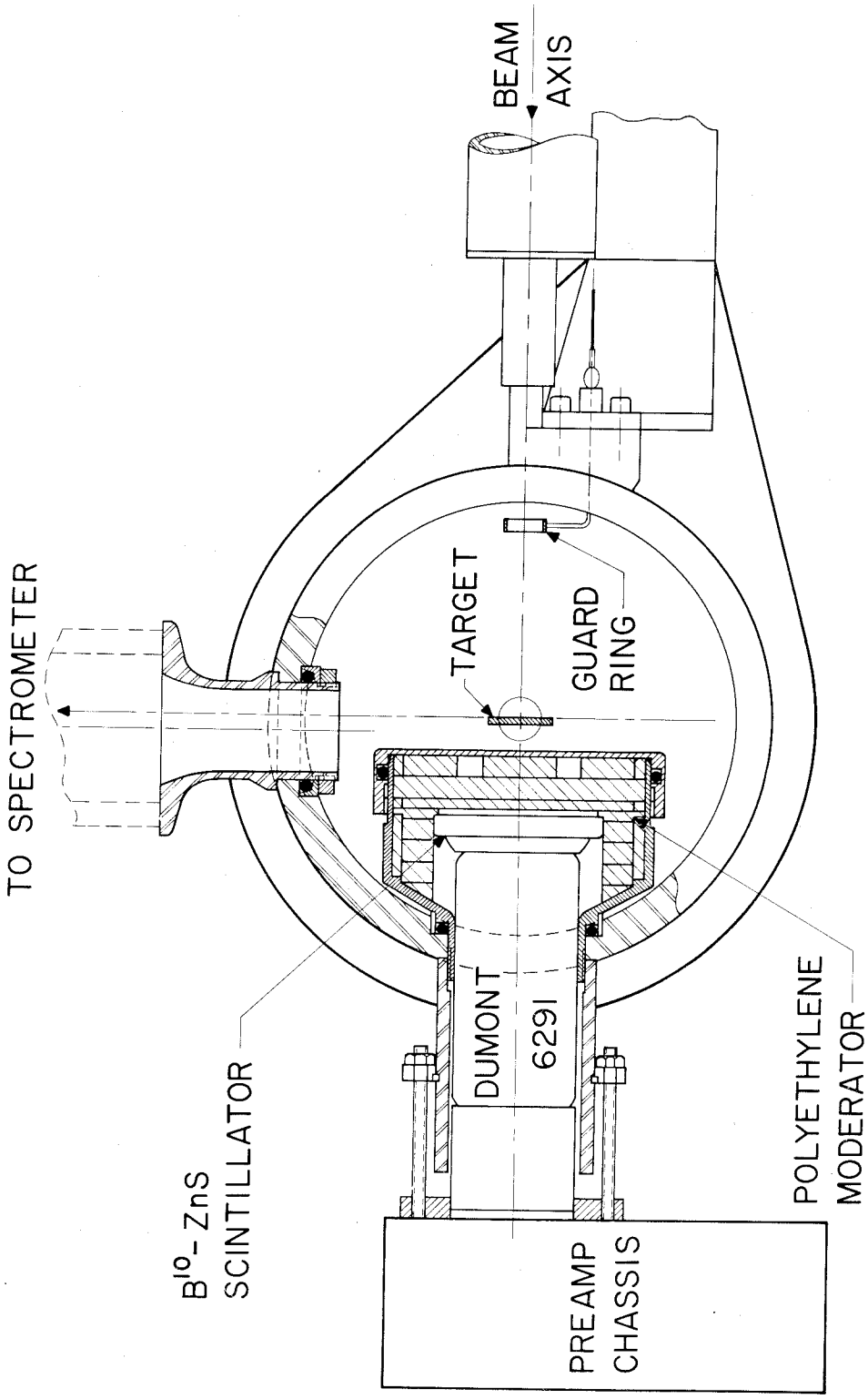

NEUTRON SCINTILLATOR LAYOUT

Figure 9: The experimental arrangement for the measurement of Q_p. The central target rod was used to hold the cracked carbon or graphite targets and the gold scattering targets, while LiF calibration targets in the auxiliary target holder permitted placing the neutron scintillator in reasonably good geometry just outside the chamber without disturbing the 150^o spectrometer angle setting. The auxiliary target rod is arranged to allow the emergent neutrons to pass through the beam entrance slot in the target chamber wall and out through the spring steel band that provides the sliding vacuum seal for the rotation of the chamber. A side view of the chamber and main target holder is shown in fig. 18. See text p. 14.

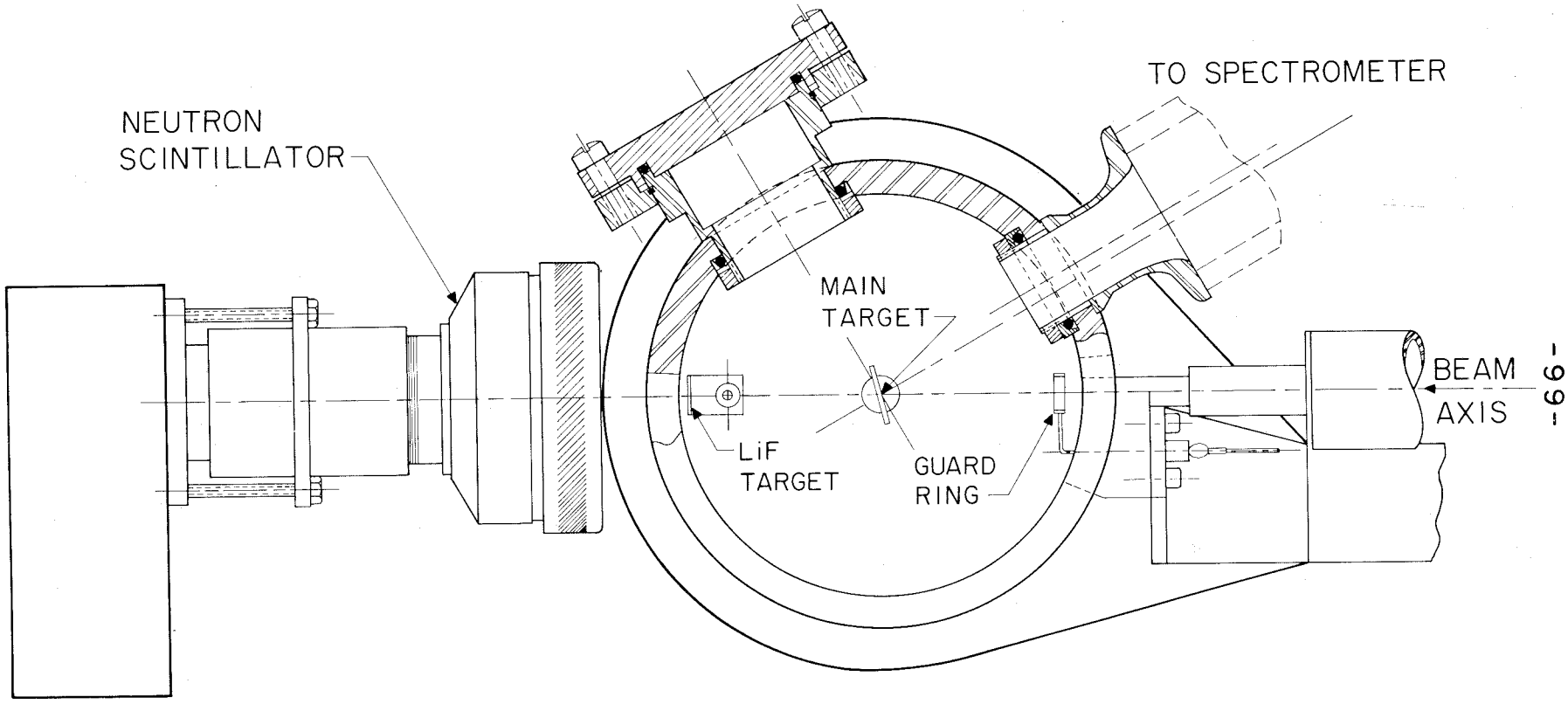

TARGET CHAMBER LAYOUT, $C^{12}(He^3, p)N^{14*}$ EXPERIMENT

Figure 10: The energy-level diagram of O^{14}, showing the beta transition to the 2.31-Mev, 0^+, T = 1 first excited state of N^{14}. See text p. 15.

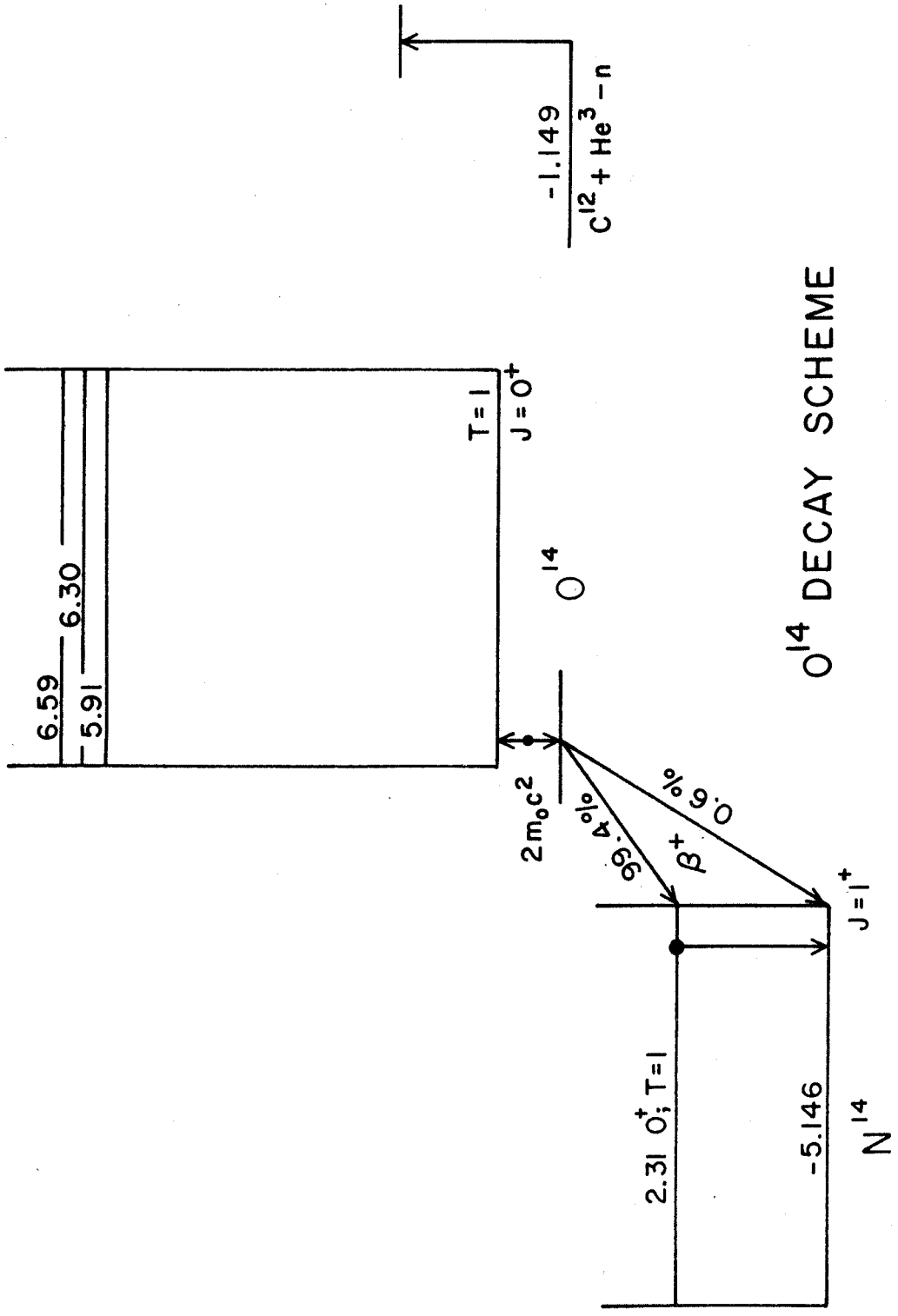

O^{14} DECAY SCHEME

Figure 11: The experimental arrangement for the O^{14} threshold measurement, showing a top view of the glass extension target chamber and the lucite beam tube containing the auxiliary regulating slits and viewing quartz. The fitting labeled "guard" was maintained at -300 v. as an electron suppressor. A side view of the same arrangement is shown in fig. 12. See text p. 15 f.

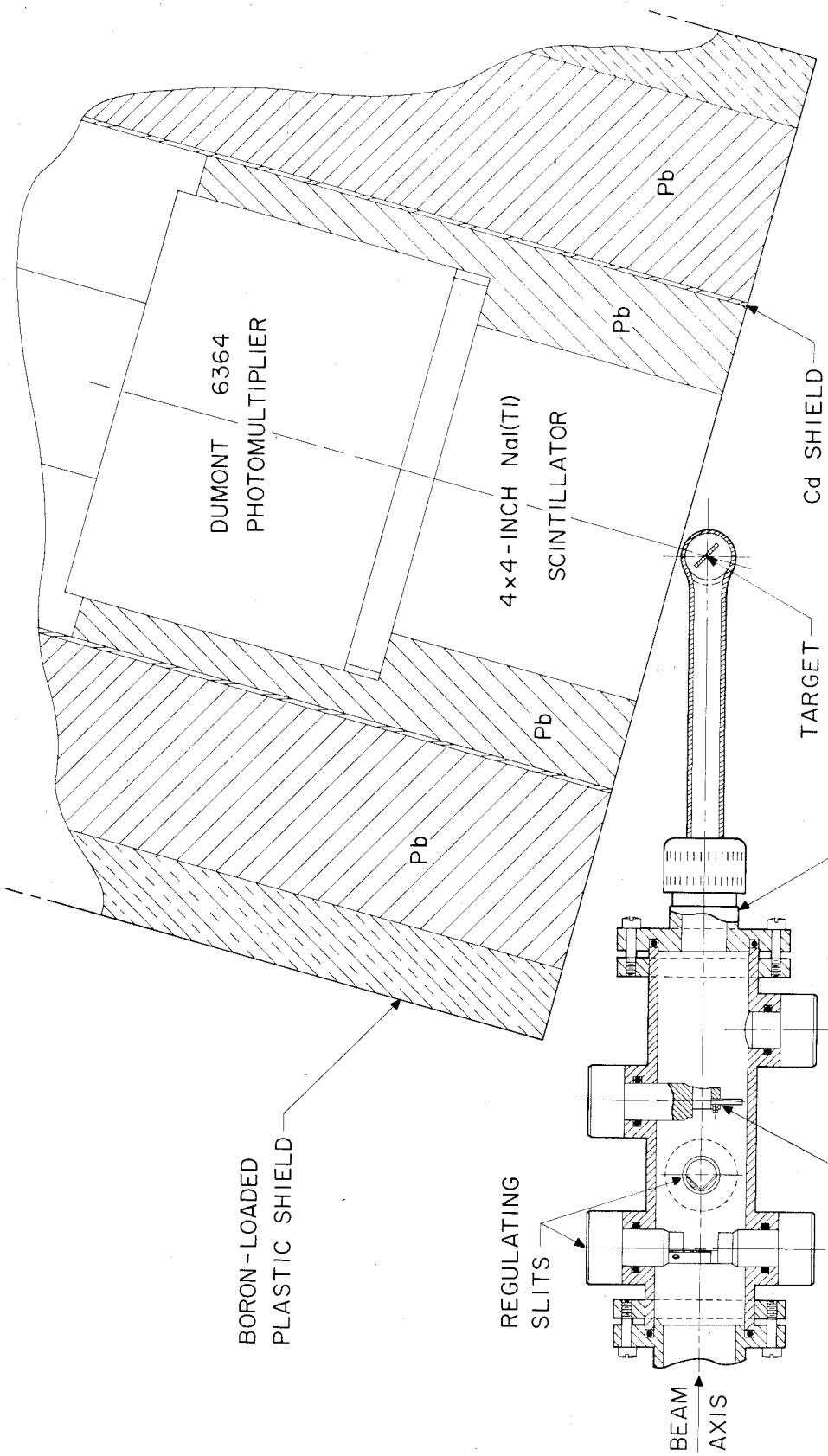

TARGET CHAMBER LAYOUT, $C^{12}(He^3, n)O^{14}$ EXPERIMENT

Figure 12. The arrangement of the neutron scintillator for calibration during the O^{14} threshold measurement. The fitting labeled "guard" was used as an electron suppressor ring. See fig. 11 for a top view of the target chamber and beam tube. See text p. 16.

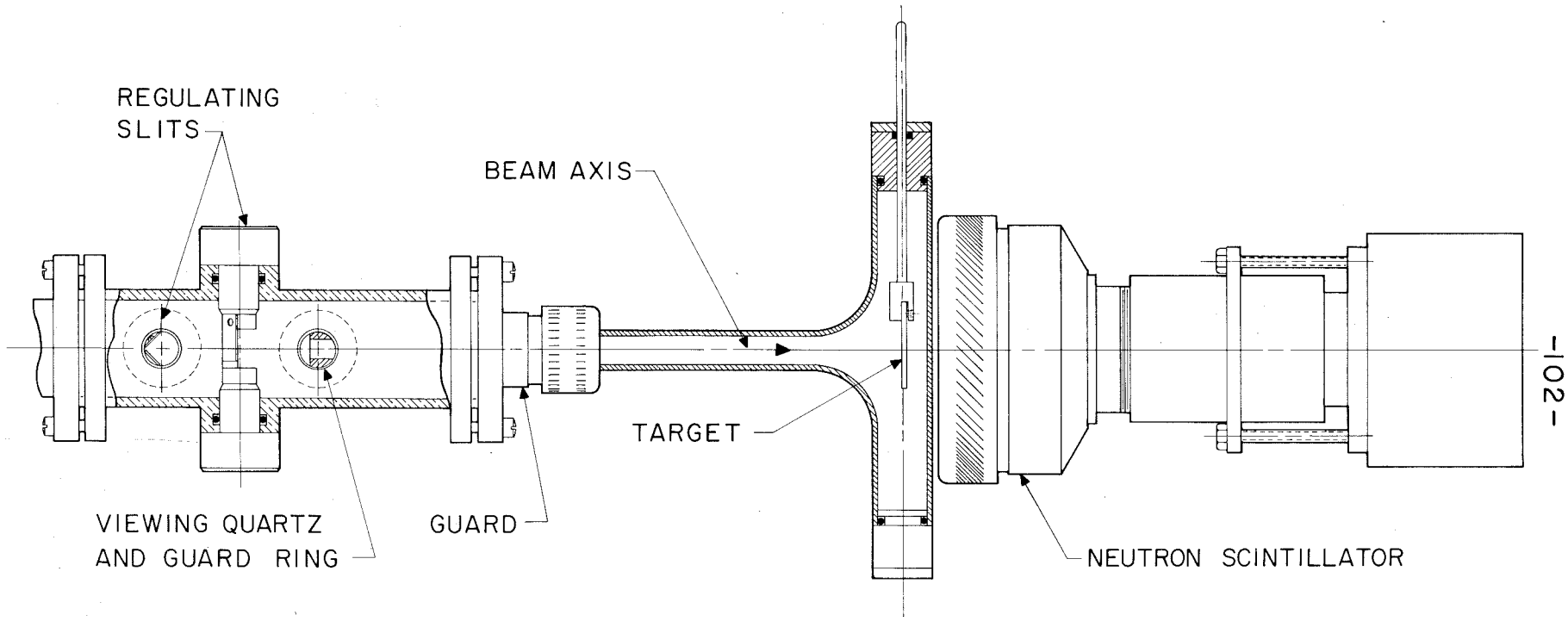

EXPERIMENTAL LAYOUT, $Li^{7}(p, n)Be^{7}$ CALIBRATION, $C^{12}(He^{3}, n)O^{14}$ EXPERIMENT

Figure 13. Block diagram of the counting circuits for the O^{14} threshold experiment. A check on the 20-sec mechanical timer was furnished by counting 120 cps from the power lines in the secondary channels of the double scalers. See text pp. 16 f.

O^{14} THRESHOLD EXPERMENT
BLOCK DIAGRAM OF COUNTING CIRCUITS

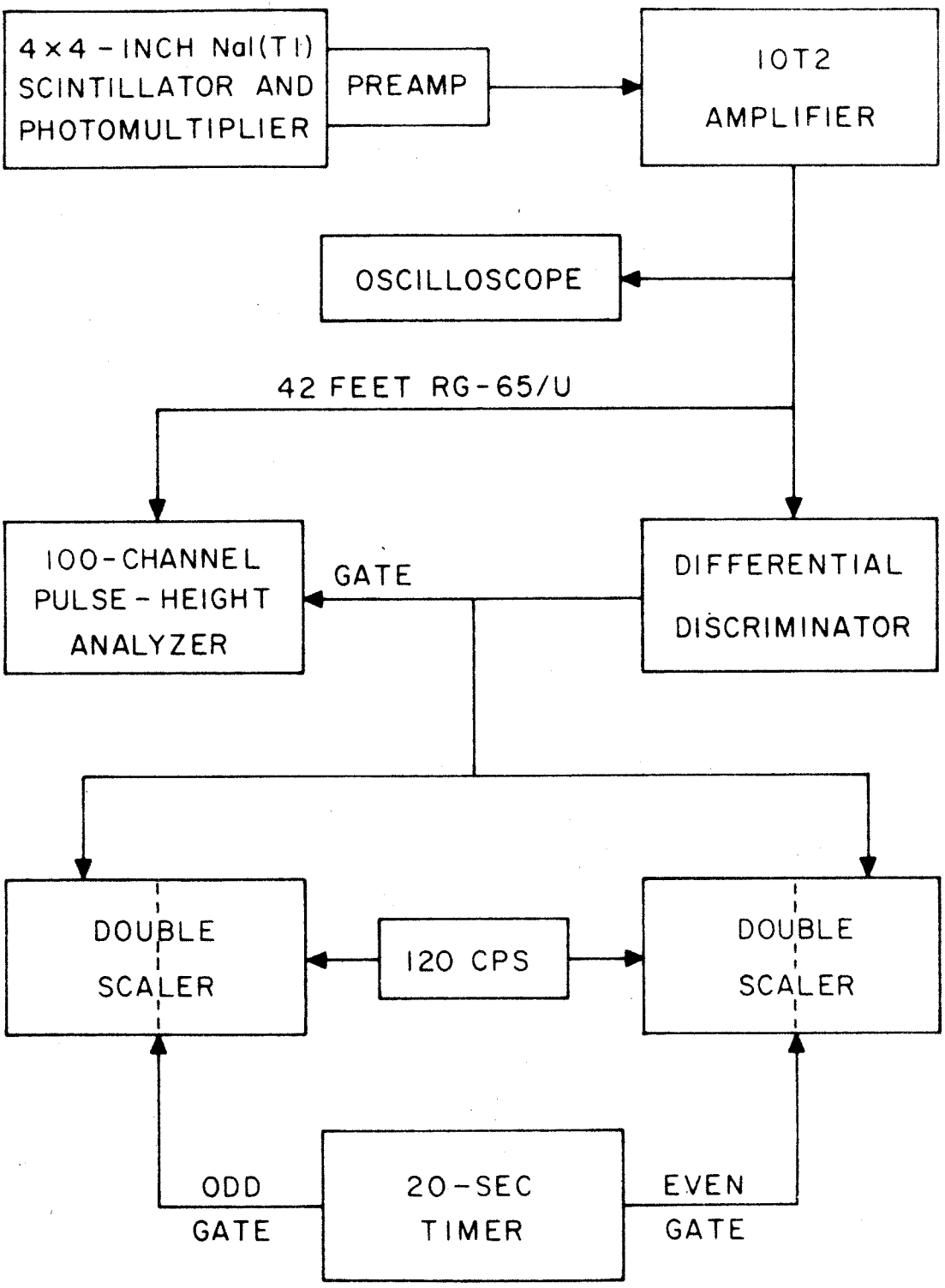

Figure 14: Block Diagram of the counting circuits for the O^{14} half-life experiment. A fast-recovery amplifier and fast pre-scalers were used in this experiment to meet the requirement of low dead time. See text pp. 19 f.

O^{14} HALF-LIFE EXPERIMENT
BLOCK DIAGRAM OF COUNTING CIRCUITS

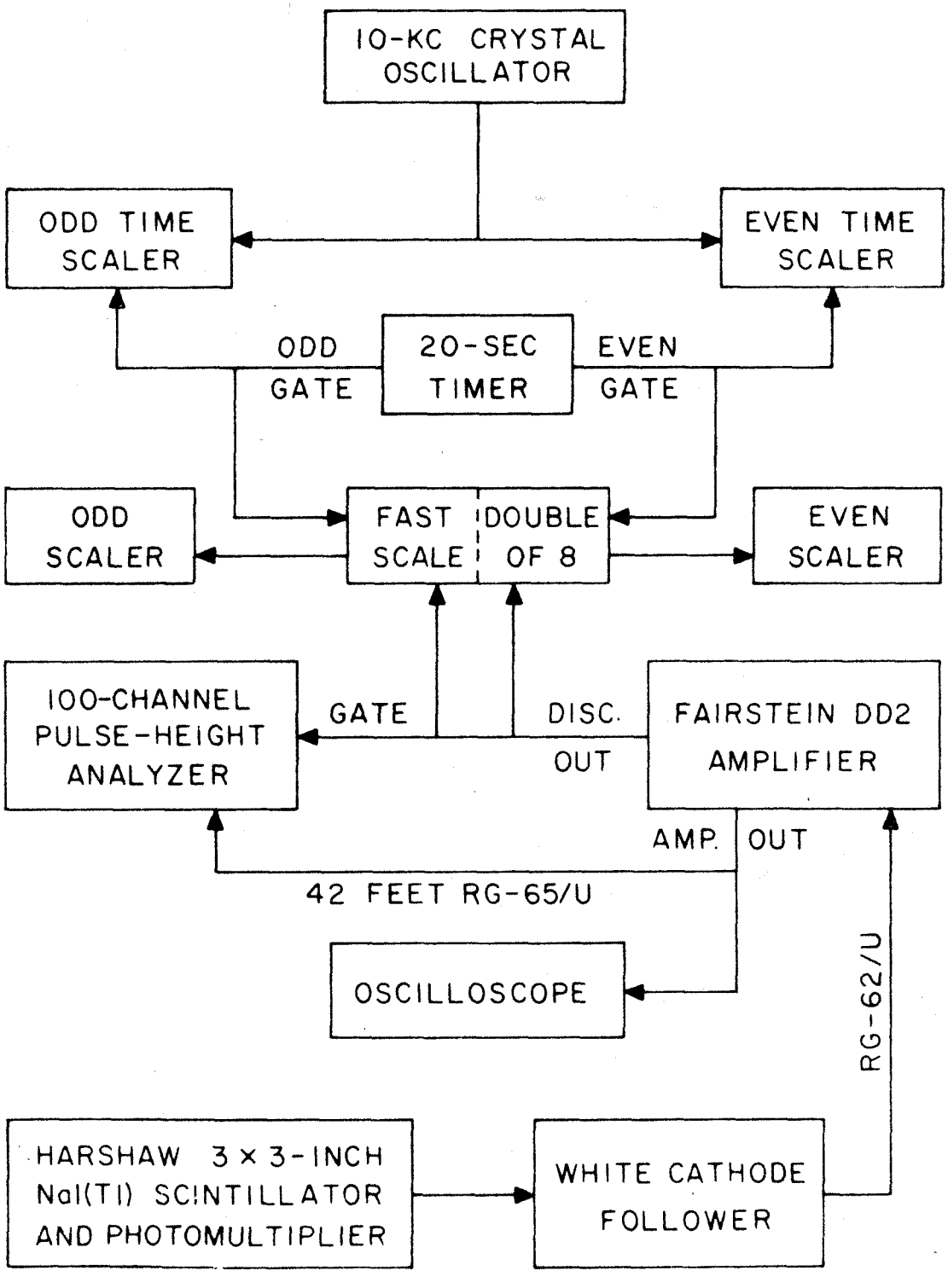

Figure 15: The $Al^{27}(p, \gamma)Si^{28}$ yield versus electrostatic-analyzer setting near the 990-kev resonance for proton and HH^+ molecular-ion beams. Note the width and asymmetry of the HH^+ step. See text pp. 22 ff.

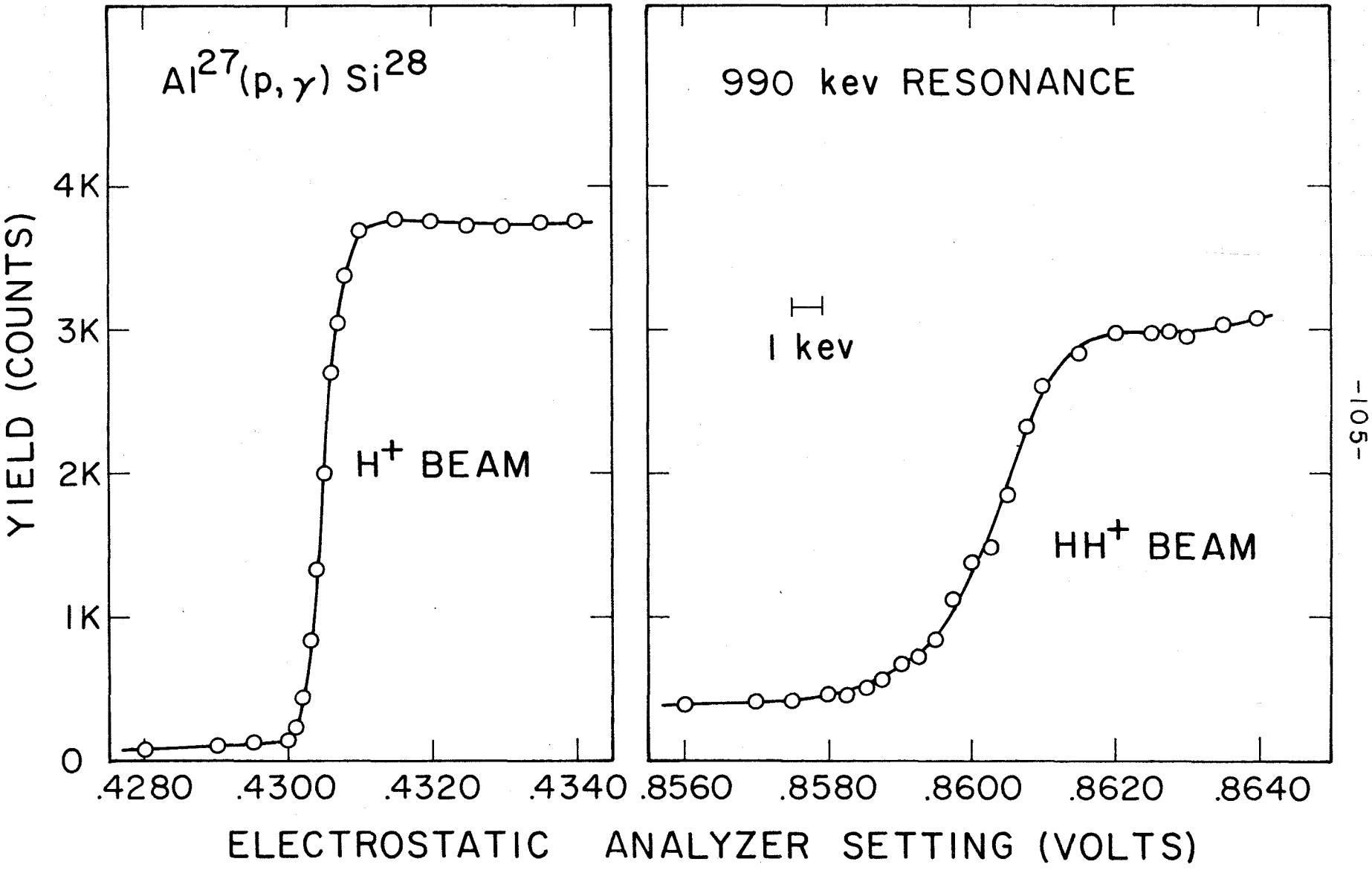
$Al^{27}(p,\gamma)\,Si^{28}$
990 kev RESONANCE
YIELD (COUNTS)
4K
3K
2K
1K
0
1 kev
H^+ BEAM
HH^+ BEAM
.4280
.4300
.4320
.4340
.8560
.8580
.8600
.8620
.8640
ELECTROSTATIC ANALYZER SETTING (VOLTS)

Figure 16: The thick-target HH^+ molecular-ion effect. The difference between the energy of the thick-target HH^+-beam yield step as measured and as calculated from the observed position of the H^+-beam yield step is plotted versus proton resonance energy for several $Al^{27}(p, \gamma)Si^{28}$ resonances. The sources of the data are (a) Andersen, et al. (30), (b) Bondelid and Kennedy (29), (c) the present experiment, and (d) Dahl, et al. (31). See text pp. 23 ff.

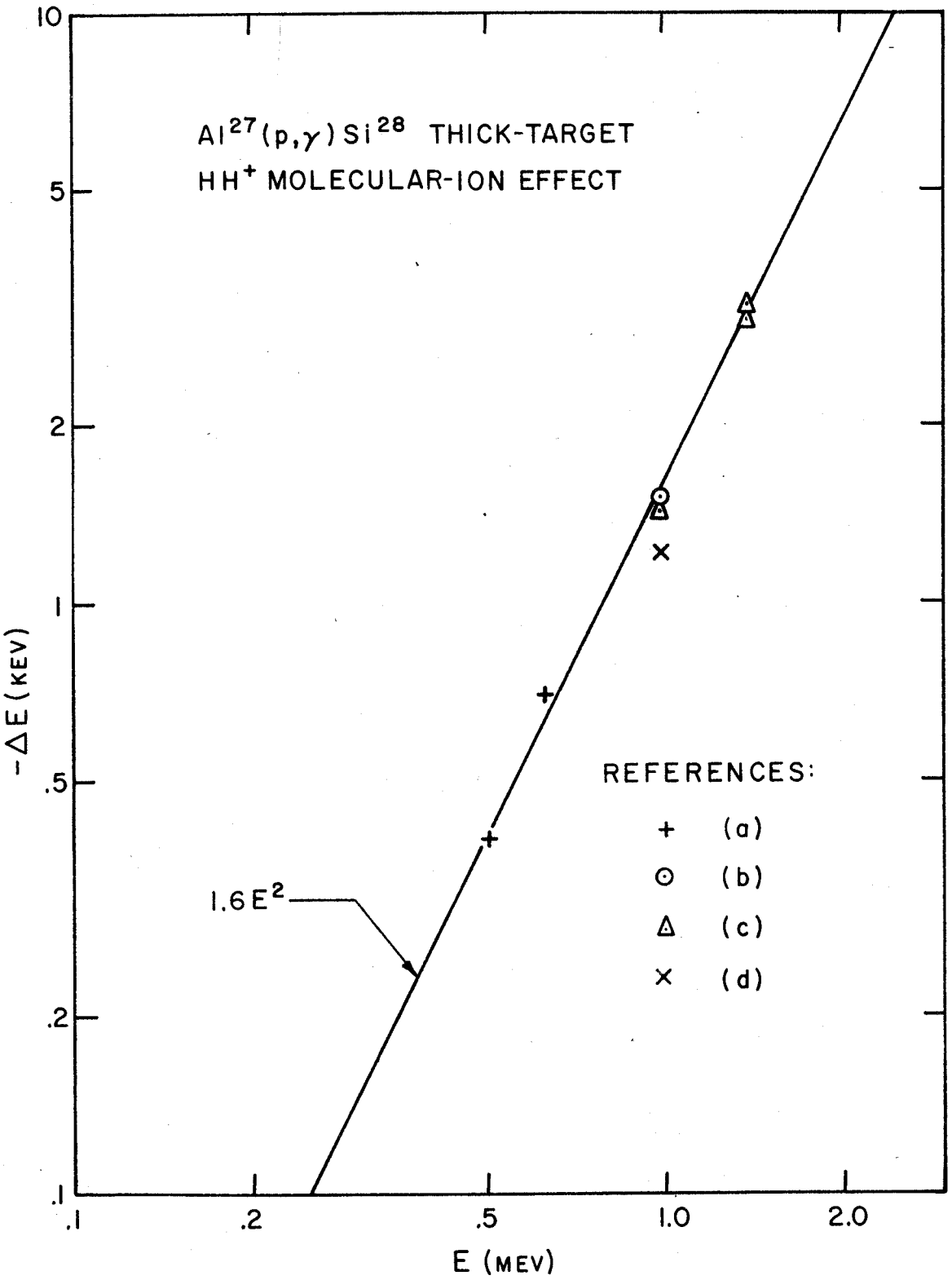
$Al^{27}(p,\gamma)Si^{28}$ THICK-TARGET
HH^+ MOLECULAR-ION EFFECT
$1.6E^2$
REFERENCES:
+ (a)
⊙ (b)
△ (c)
× (d)
$-\Delta E$ (KEV)
E (MEV)
10
5
2
1
.5
.2
.1
.1
.2
.5
1.0
2.0

Figure 17: The 2/3 power of the $Li^7(p, n)Be^7$ threshold yield versus electrostatic-analyzer setting as taken with the B^{10} neutron scintillator in the arrangements of (a) fig. 8, (b) fig. 9, and (c) fig. 12. Profile (a) was taken before the electrostatic-analyzer voltage dividers were repaired, and has been normalized to the analyzer calibration resulting from the new divider ratio. See text pp. 28 f. and 34.

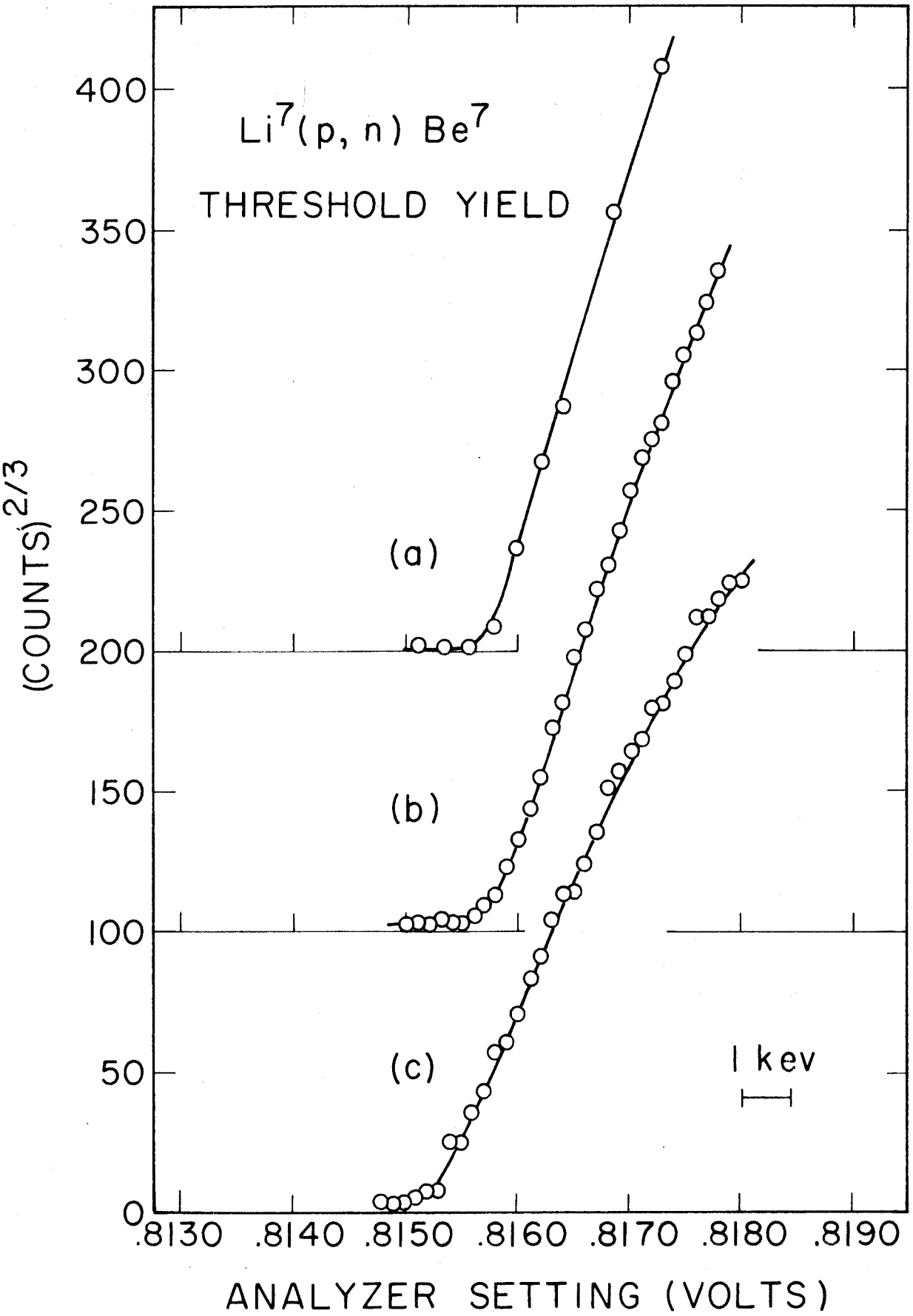
Li7(p, n) Be7
THRESHOLD YIELD
(a)
(b)
(c)
1 kev
(COUNTS)2/3
0
50
100
150
200
250
300
350
400
.8130
.8140
.8150
.8160
.8170
.8180
.8190
ANALYZER SETTING (VOLTS)

Figure 18: The experimental arrangement used to measure the angle of observation in the measurement of Q_p. The 0.040-inch vertical slit mask is shown in front of the spectrometer entrance aperture; together with the outer tube of the double target rod, its position may be set on the vertical scale and the 0.1° vernier protractor which measure the two independent adjustments of the main target holder assembly. The angular position of the target and inner rod is set using the auxiliary index shown. The auxiliary target-rod support bearing shown was found to be necessary to reduce target eccentricity error. Also shown are a sectional view of the sliding band vacuum seal of the chamber and a view of the quartz beam-viewer, which is mounted on a ring gear driven by a pinion and thumb wheel. See text p. 29.

TARGET CHAMBER LAYOUT, SPECTROMETER ANGLE MEASUREMENT

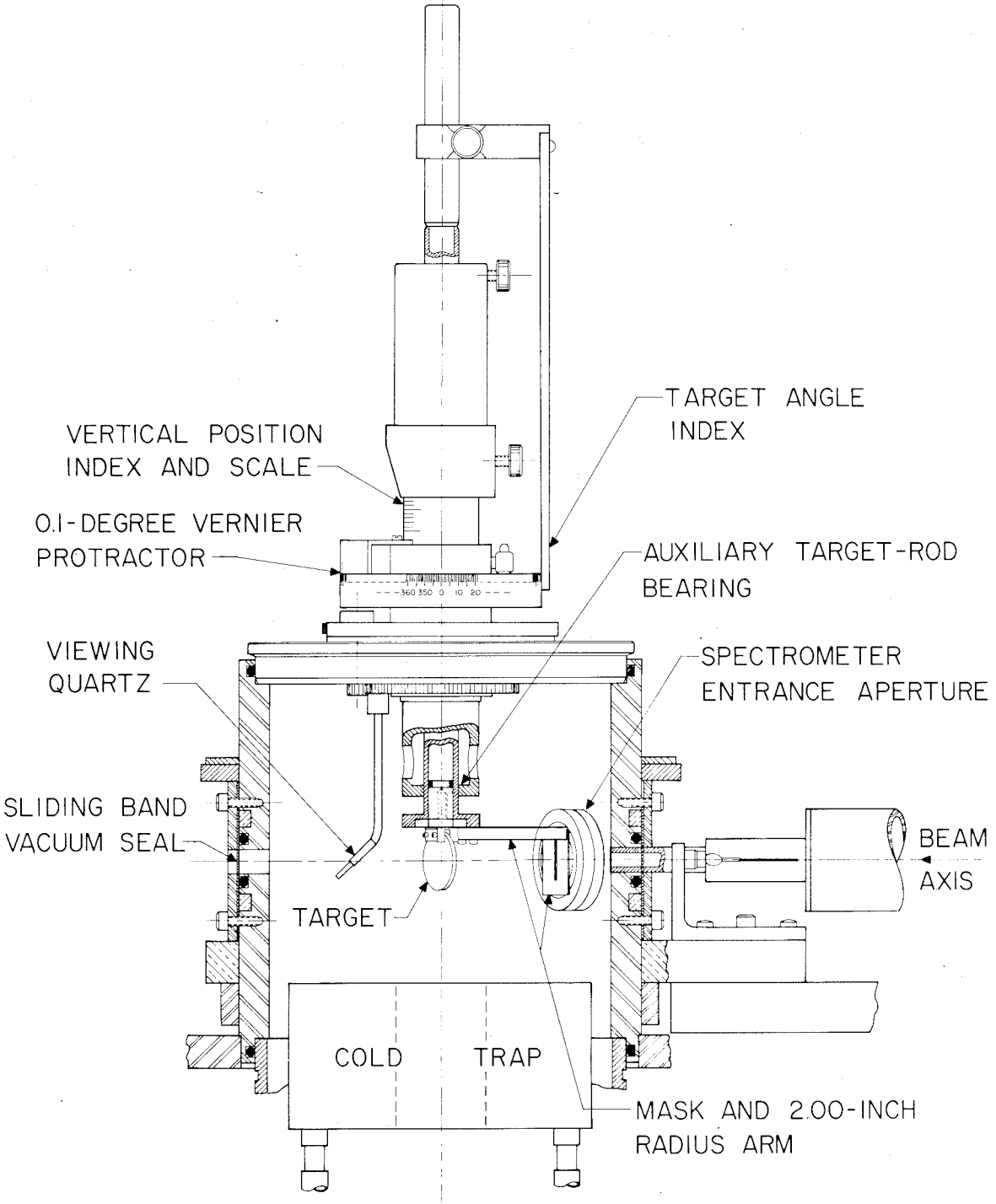

Figure 19: The yields of $Au^{197}(p, p)Au^{197}$ and $Au^{197}(He^{4+}, He^{4++})Au^{197}$ elastic scattering versus angular position of the 0.040-inch vertical slit mask as the mask is swept across the beam and the spectrometer aperture. See text p. 30.

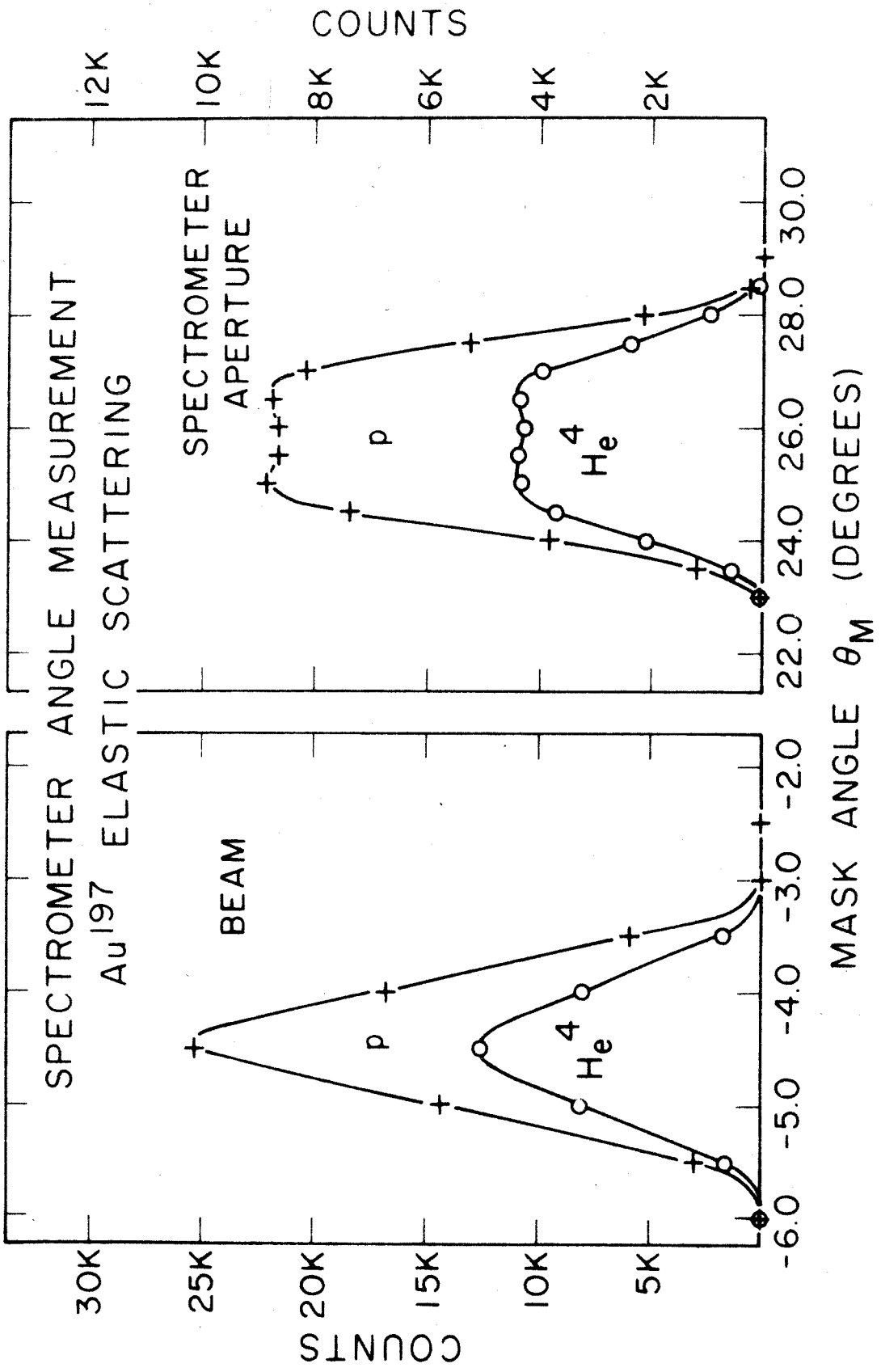
SPECTROMETER ANGLE MEASUREMENT
Au197 ELASTIC SCATTERING
BEAM
SPECTROMETER APERTURE
p
4He
COUNTS
30K
25K
20K
15K
10K
5K
12K
10K
8K
6K
4K
2K
-6.0
-5.0
-4.0
-3.0
-2.0
22.0
24.0
26.0
28.0
30.0
MASK ANGLE θM (DEGREES)

Figure 20: Illustration of sources of error in the measurement of the angle of observation in the $C^{12}(He^3, p)N^{14*}$ reaction. (a) The error due to failure of the beam to pass through the axis of rotation of the mask; this error vanishes in first order. (b) The error due to failure of the target to lie on the axis of rotation of the mask. See text pp. 30 f.

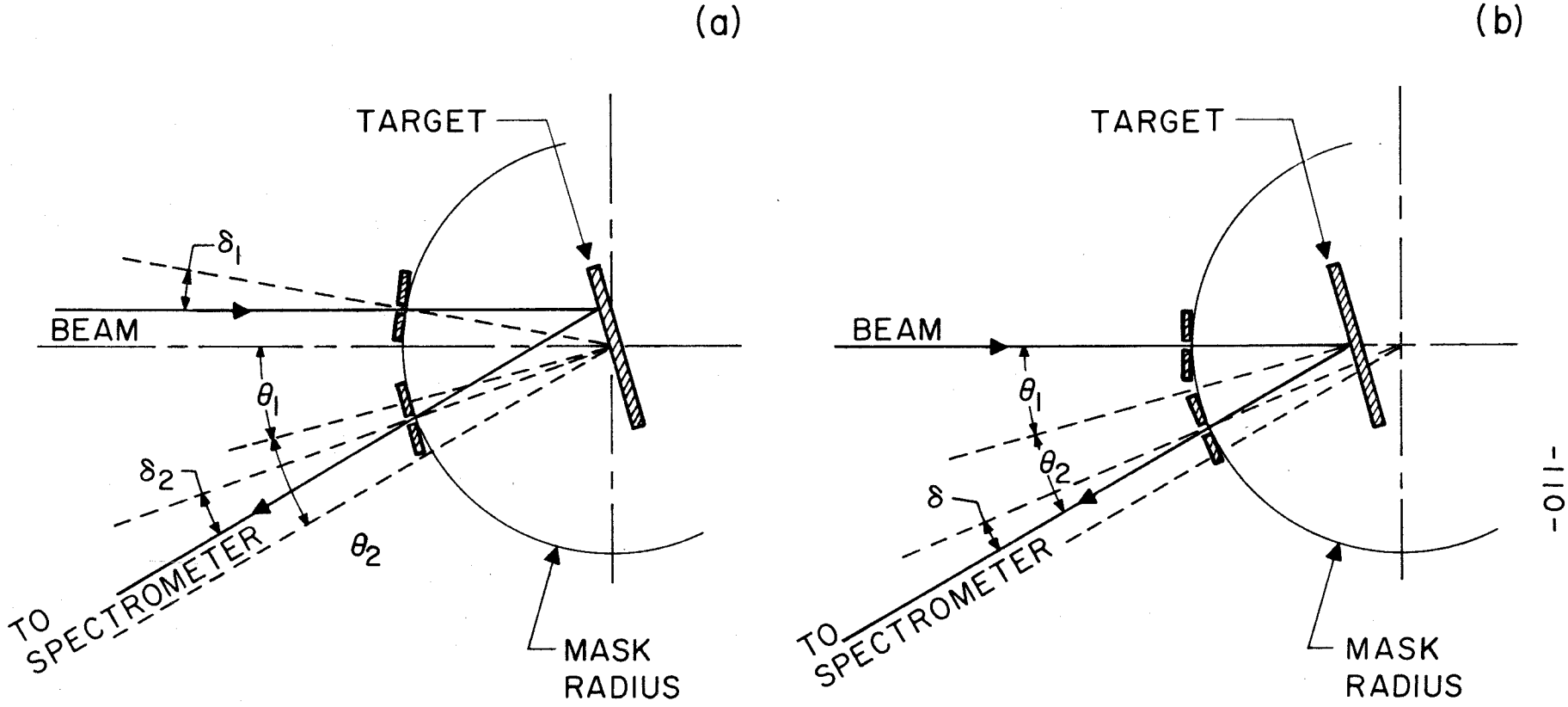

SOURCES OF ERROR IN MEASURING ANGLE OF OBSERVATION

Figure 21: Contour map of the transmission of the magnetic-spectrometer entrance aperture as measured with $Au^{197}(p, p)Au^{197}$ elastic scattering near 1.88 Mev proton energy and 90^{o} laboratory angle. The angular size of the mask aperture used to define the scattered beam is indicated by the circle in the upper left corner of the figure. See text p. 31.

SPECTROMETER TRANSMISSION FUNCTION

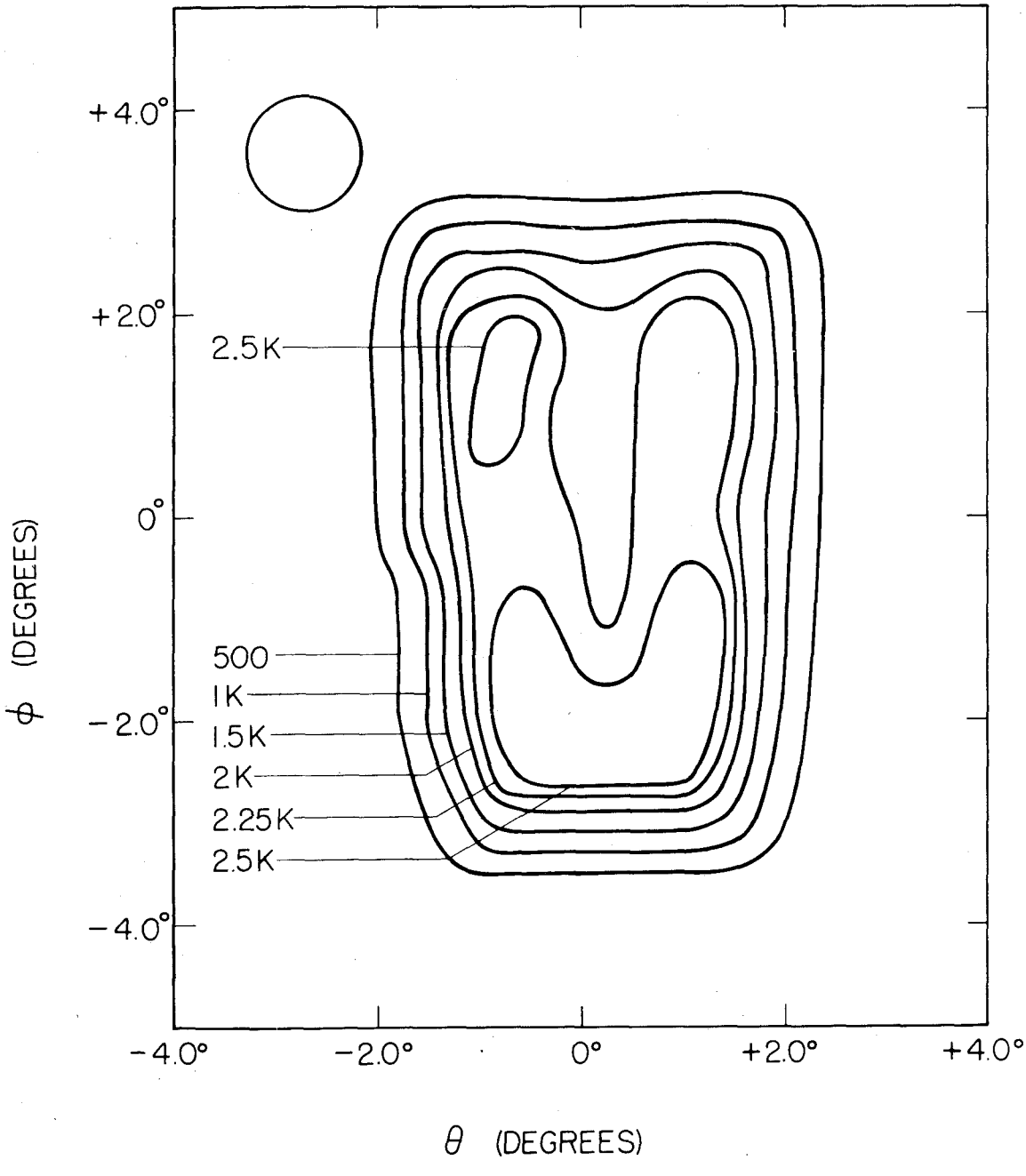

Figure 22: The yield of the reaction $C^{12}(He^3, p)N^{14*}$ (2.311-Mev state) versus incident He^3 energy near 2.69 Mev with the magnetic spectrometer set to accept protons of energy 3.633 Mev at laboratory angle 150°. The tangent line to the face of the profile rises in 1.35% of the average incident energy, which is to be compared with the theoretical value 1.39% calculated in Appendix B, pp. 70 f. See also text p. 34.

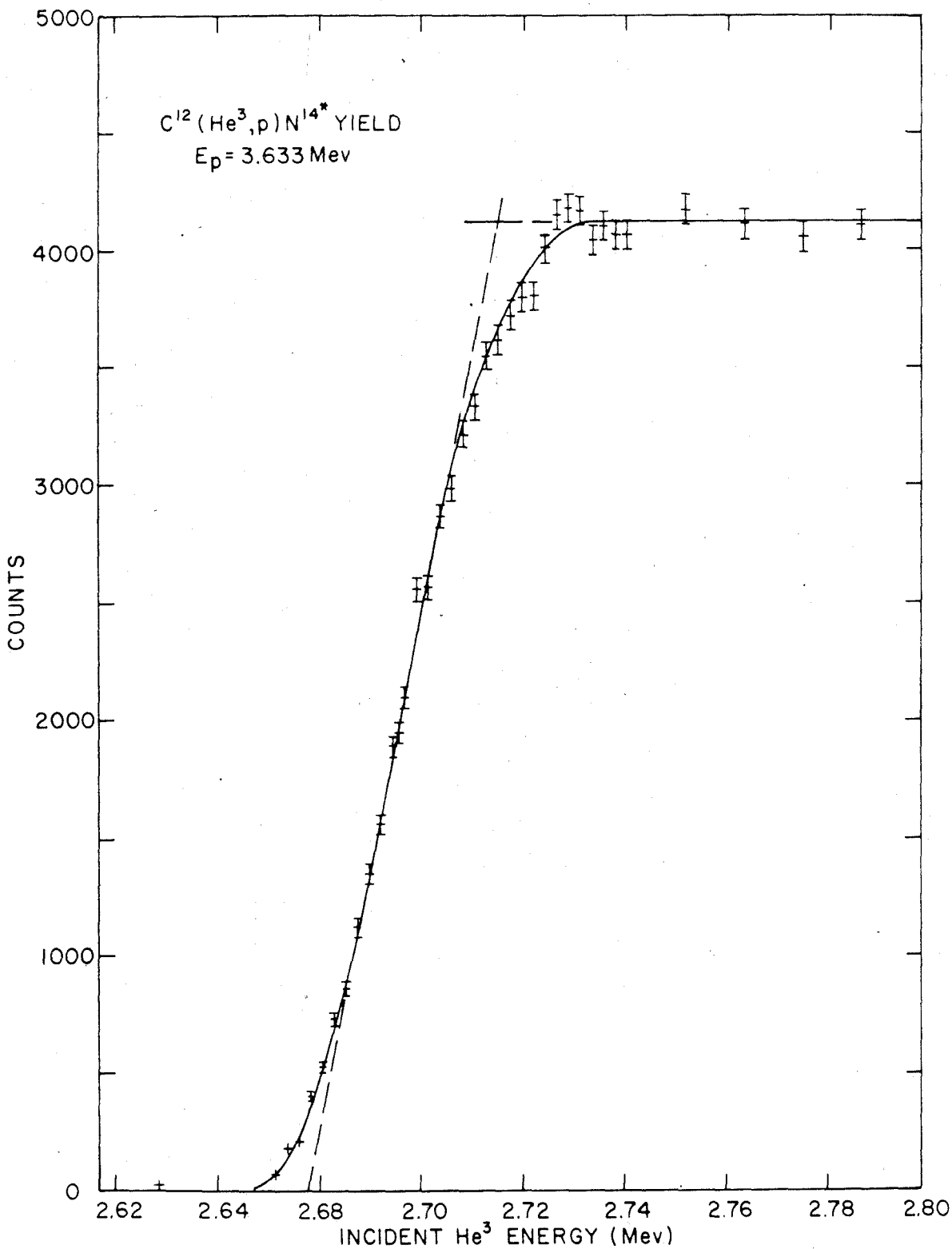
$C^{12}(He^3,p)N^{14*}$ YIELD
E_p = 3.633 Mev
COUNTS
INCIDENT He^3 ENERGY (Mev)
0
1000
2000
3000
4000
5000
2.62
2.64
2.68
2.70
2.72
2.74
2.76
2.78
2.80

Figure 23: The yield versus incident deuteron energy of the $Au^{197}(d, d)Au^{197}$ elastic scattering used for spectrometer calibration in the measurement of Q_p. The spectrometer field and angle were left undisturbed for each complete run of the $C^{12}(He^3, p)N^{14*}$ reaction and its associated calibrations. See text p. 34.

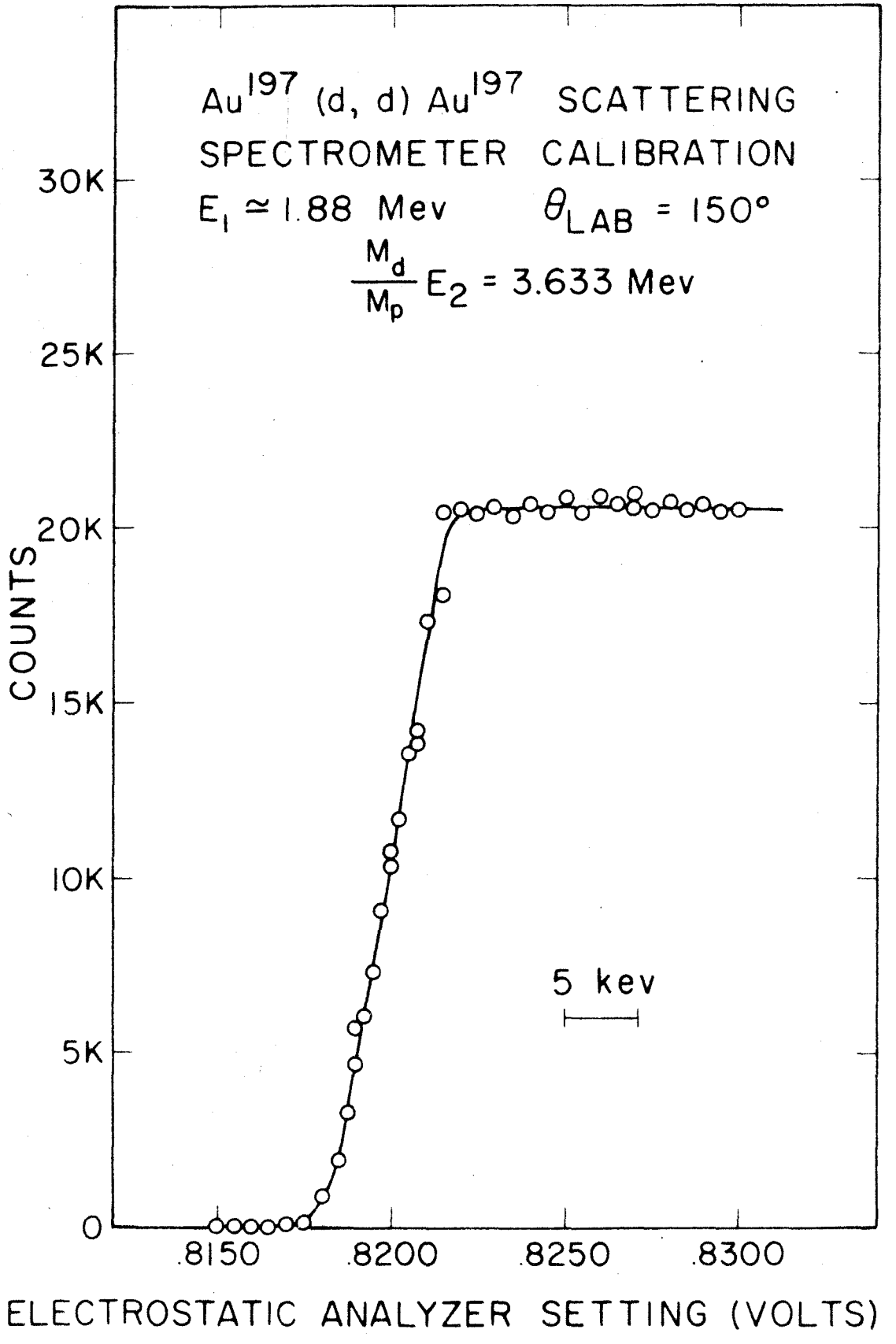
Au^{197} (d, d) Au^{197} SCATTERING
SPECTROMETER CALIBRATION
$E_1 \simeq 1.88$ Mev
$\theta_{LAB} = 150°$
$\frac{M_d}{M_p} E_2 = 3.633$ Mev
30K
25K
20K
15K
10K
5K
0
COUNTS
5 kev
.8150
.8200
.8250
.8300
ELECTROSTATIC ANALYZER SETTING (VOLTS)

Figure 24: The 2/3 power of the $C^{12}(He^3, n)O^{14}$ threshold yield versus incident He^3 energy. The yield shown is the integrated counting rate of delayed 2.31-Mev gamma rays from the reaction $C^{12}(He^3, n)O^{14}(\beta^+ \nu)N^{14*}(\gamma)N^{14}$ over the first two minutes following an activation, corrected for background and for the remaining activity from previous runs. The line shown is a least-squares fit to the threshold. See text pp. 38 f.

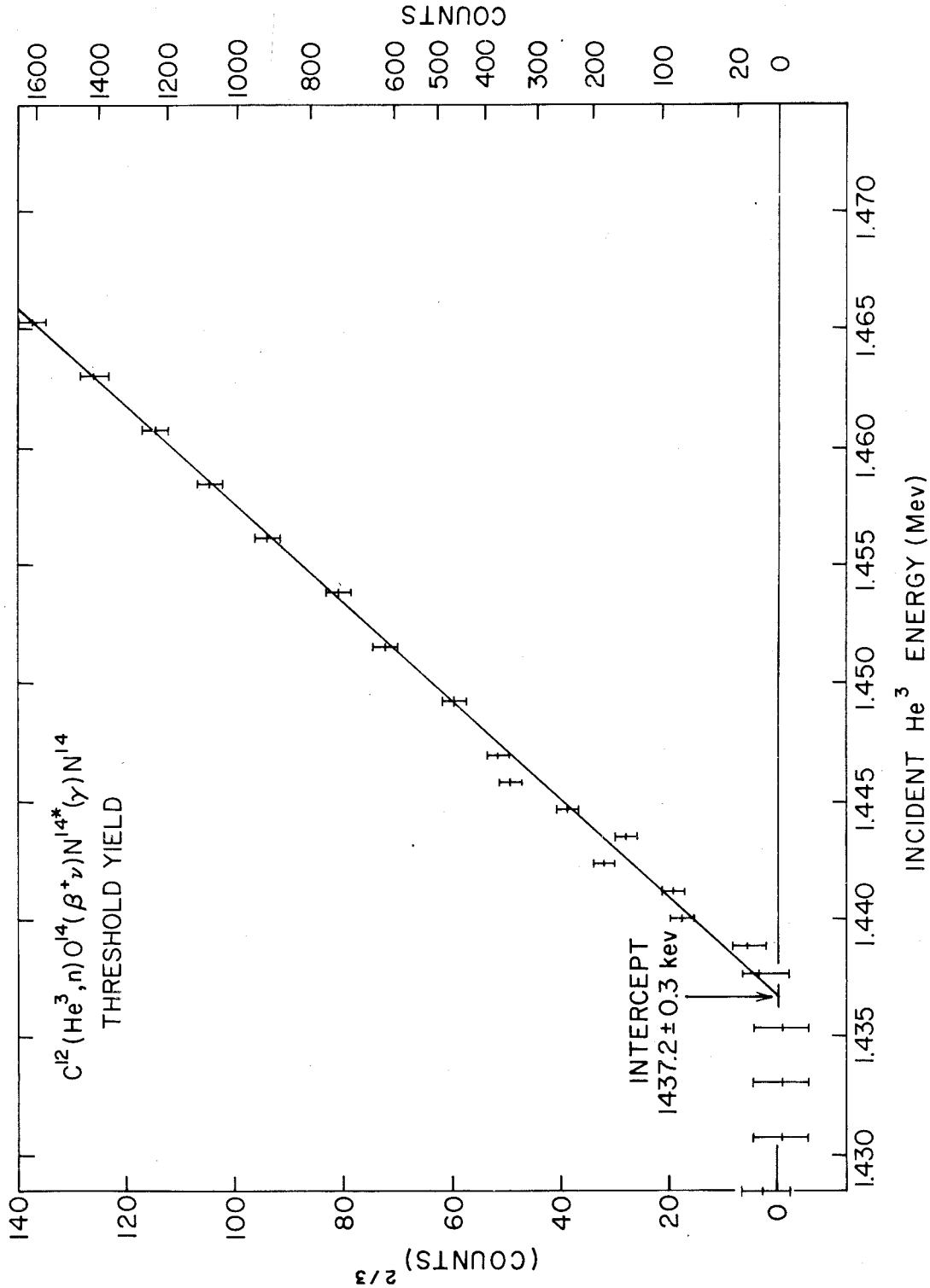
$C^{12}(He^3,n)O^{14}(\beta^+\nu)N^{14*}(\gamma)N^{14}$
THRESHOLD YIELD
INTERCEPT
1437.2 ± 0.3 kev
(COUNTS)$^{2/3}$
COUNTS
INCIDENT He^3 ENERGY (Mev)
0
20
40
60
80
100
120
140
20
100
200
300
400
500
600
800
1000
1200
1400
1600
1.430
1.435
1.440
1.445
1.450
1.455
1.460
1.465
1.470

Figure 25: Spectra of delayed gamma rays from $C^{12} + He^{3}$ taken during the O^{14} half-life measurement. The spectra of pulses coincident with the output of the differential discriminator, multiplied by ten, are superimposed on the total spectrum for the case (a) with no absorber between source and scintillator, and (b) with a 2-cm Pb absorber. Note that the peak at A is the double annihilation-radiation peak due to pile-up; the single annihilation-radiation peak was cut out by the lower-level discriminator of the pulse-height analyzer to minimize analyzer dead time. For the case without absorber, single and double annihilation-radiation pileup on the 2.31-Mev N^{14} gamma ray are visible at B and C, respectively. This should be compared with the single pileup visible at D when the absorber was used. See text pp. 39 f.

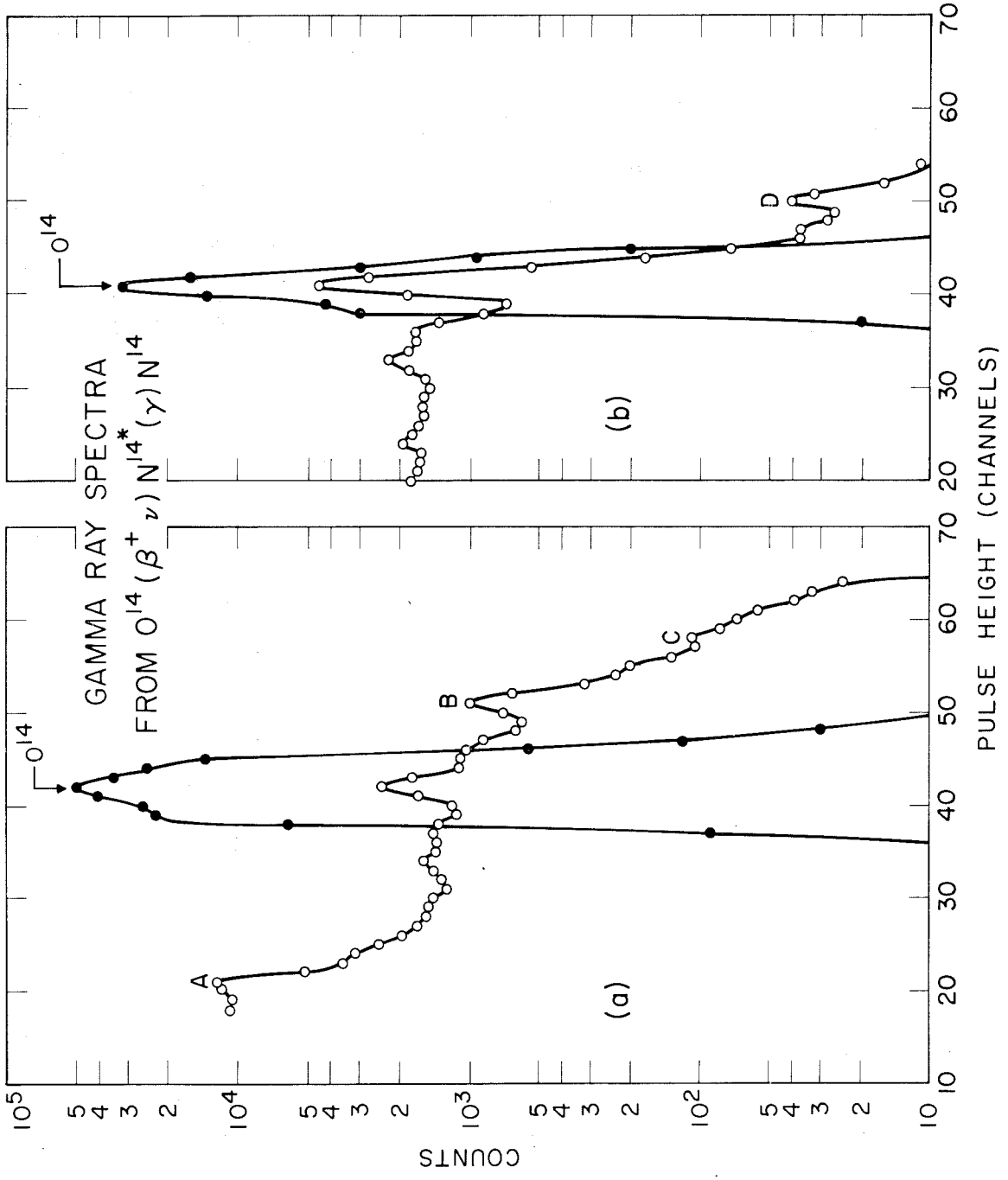
GAMMA RAY SPECTRA
FROM $O^{14}(\beta^+\nu)N^{14*}(\gamma)N^{14}$
O^{14}
A
B
C
D
(a)
(b)
COUNTS
PULSE HEIGHT (CHANNELS)

Figure 26: The delayed 2.31-Mev gamma-ray yield from the O^{14} half-life measurement versus time in 20-sec channels. Correction for dead time has been made for all points, and the crosses show the effects of subtracting a constant background of 10 counts per channel. The line shown is a least-squares fit to the decay curve. See text pp. 38 ff.

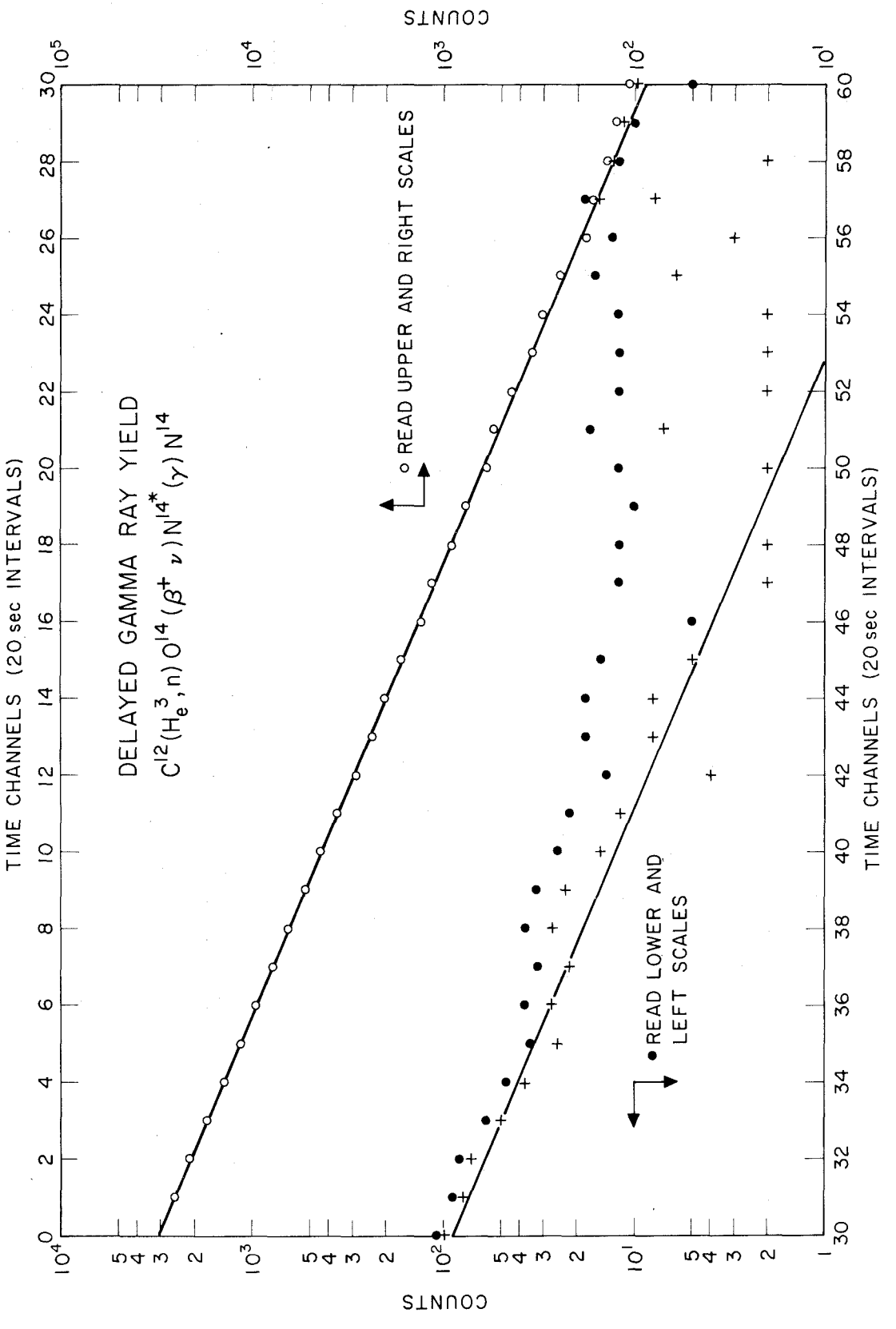
DELAYED GAMMA RAY YIELD
$C^{12}(H_e^3, n)O^{14}(\beta^+ \nu)N^{14*}(\gamma)N^{14}$
○ READ UPPER AND RIGHT SCALES
● READ LOWER AND LEFT SCALES
TIME CHANNELS (20 sec INTERVALS)
TIME CHANNELS (20 sec INTERVALS)
COUNTS
COUNTS

Figure 27: Overall view of the rebuilt fluxmeter assembly. The position of the assembly as installed in the spectrometer is shown in fig. 5, and the detailed construction of the bearings is shown in fig. 28. See text pp. 53 f.

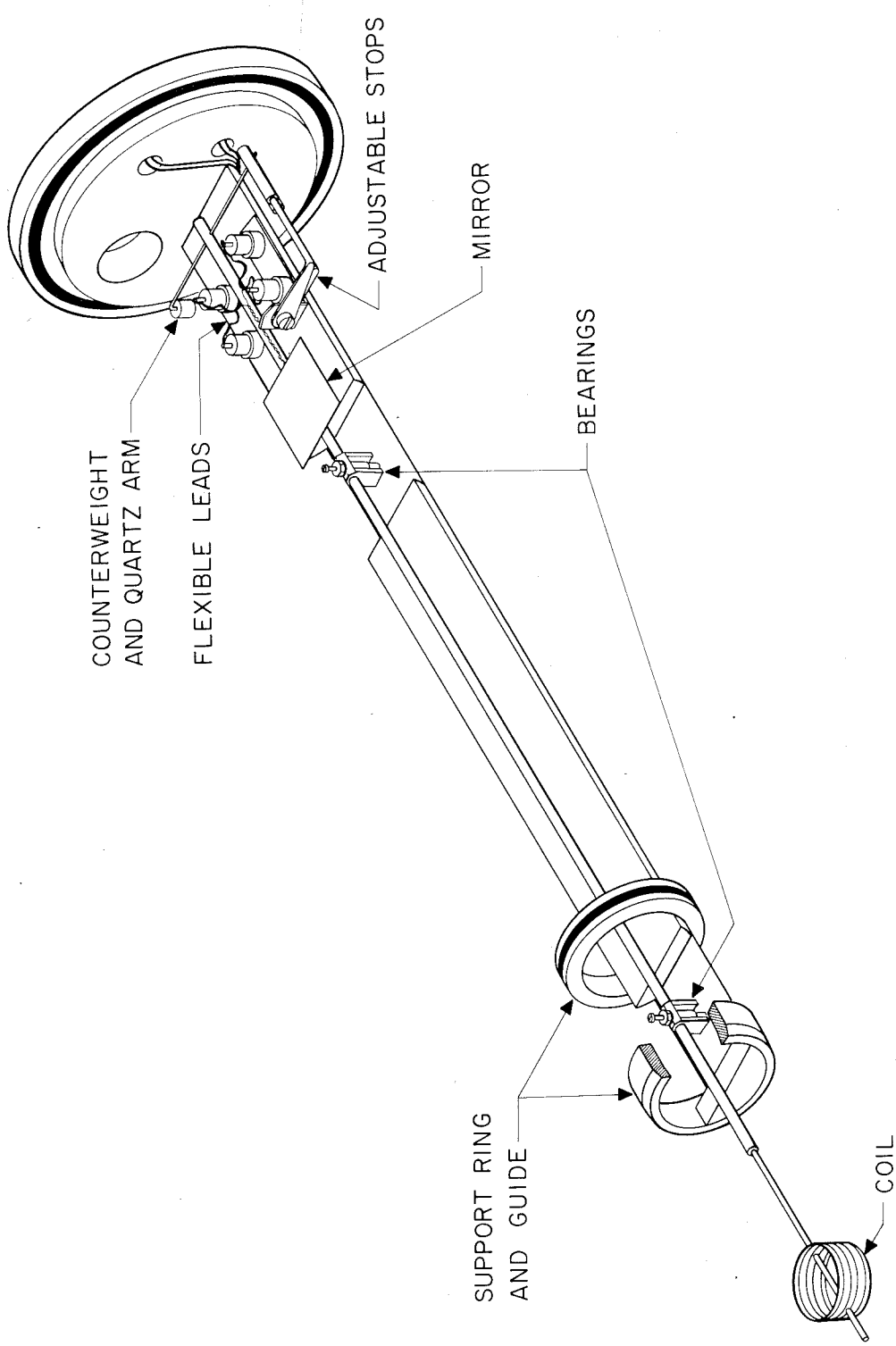

FLUXMETER ASSEMBLY, 16-INCH MAGNETIC SPECTOMETER

Figure 28: Detail of fluxmeter bearing construction.

See fig. 27 and text p. 55.

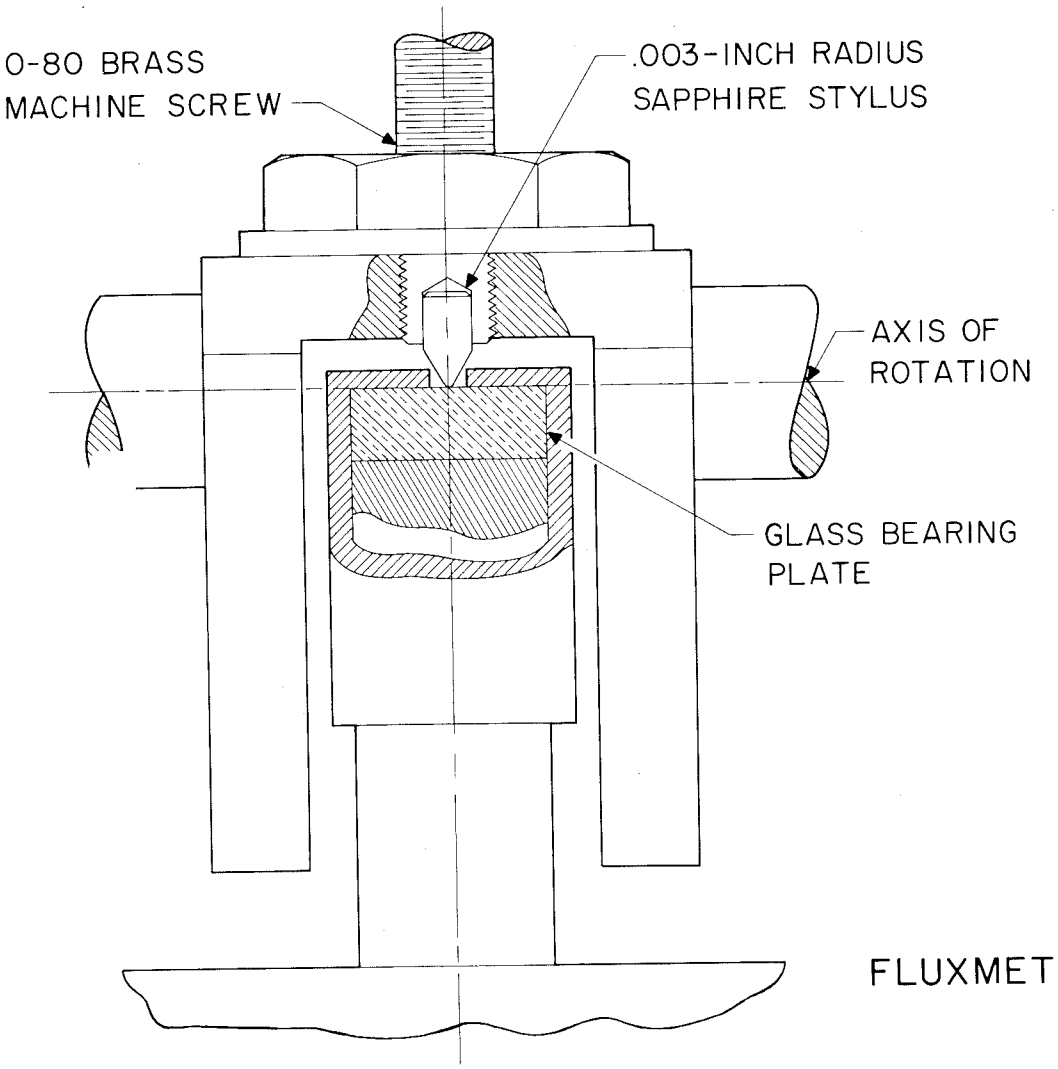

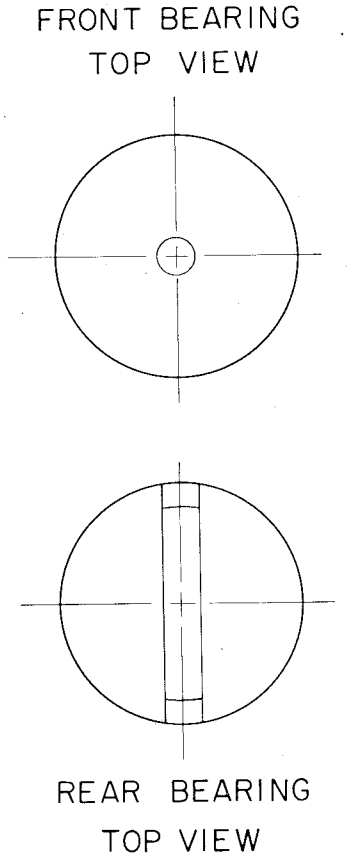

FLUXMETER BEARING DETAILS

Figure 29: Schematic of the photoelectric fluxmeter indicator circuit. See text pp. 57 f.

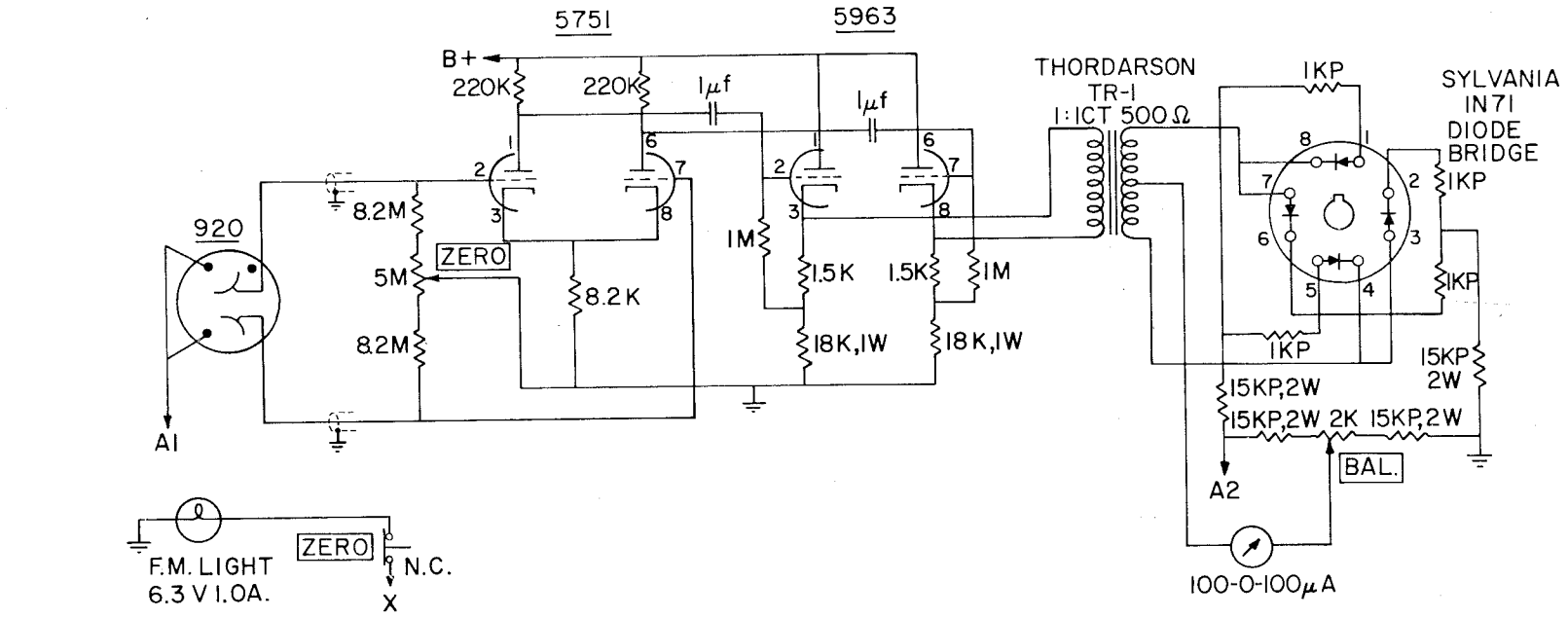

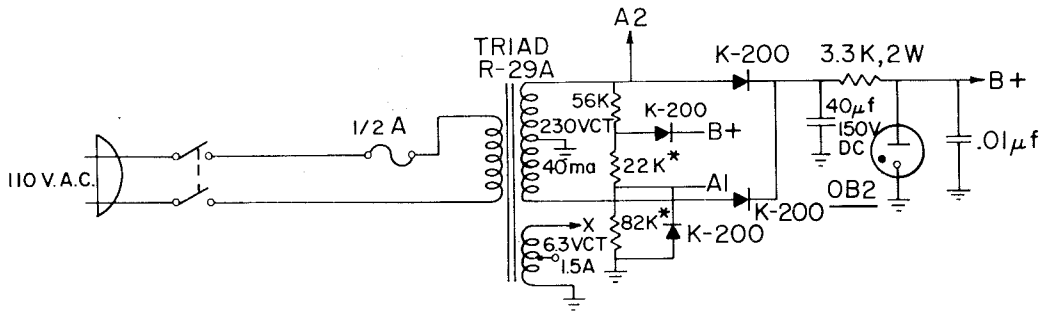

*CHOOSE FOR 90 V. PK
AT POINT A1

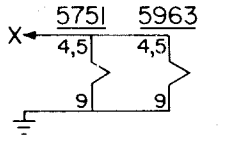

FILAMENT WIRING

Figure 30: Schematic of the fluxmeter current-control circuit. The connections indicated as leading to the Kelvin bridge circuit are designed to permit the measurement of the coil resistance in order to determine its temperature. See fig. 31 and text pp. 58 f.

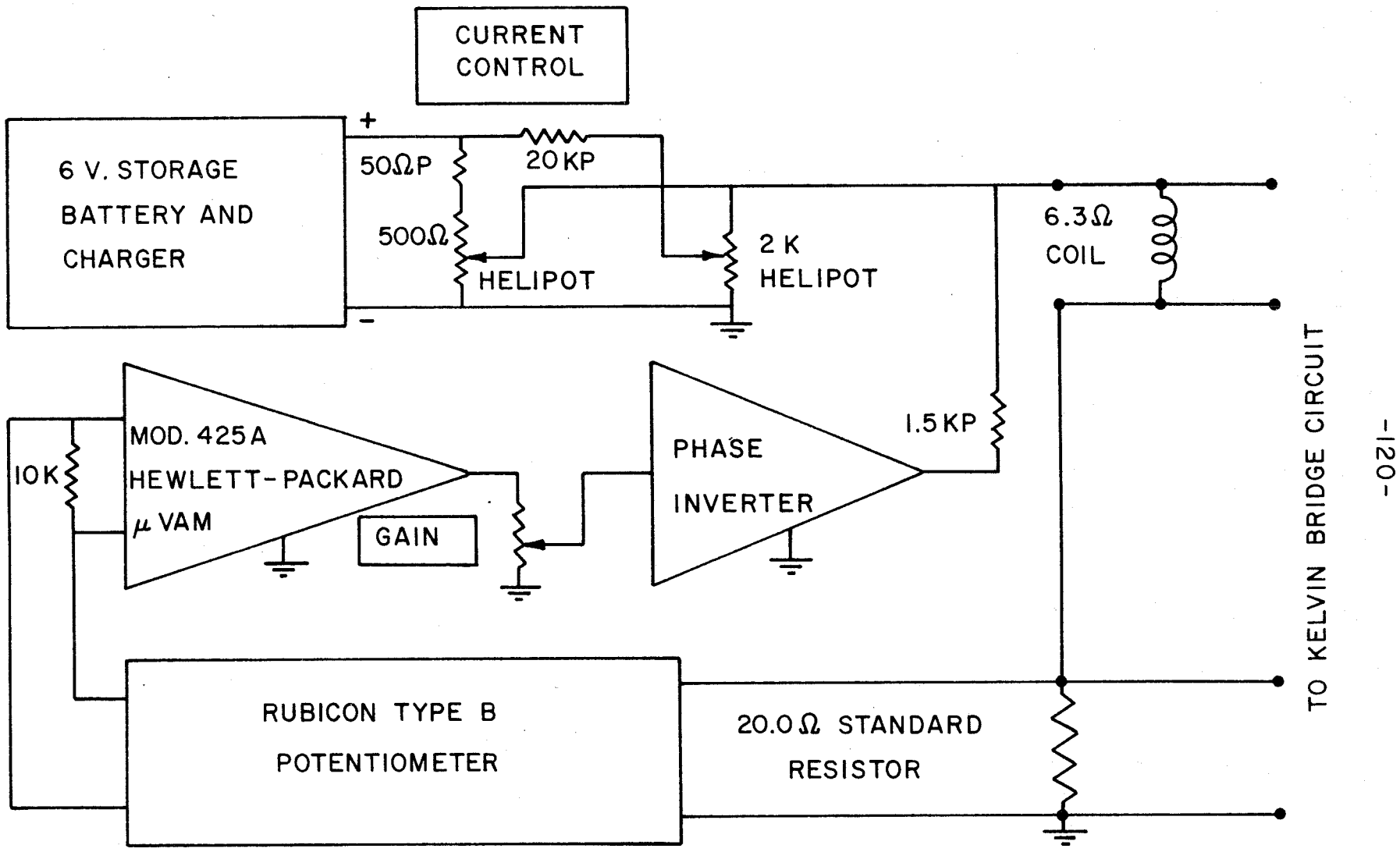

SIMPLIFIED SCHEMATIC, FLUXMETER CURRENT CONTROL

Figure 31: Schematic of the modified Kelvin bridge circuit used to measure the temperature of the fluxmeter coil by the variations in its resistance. See text pp. 59 f.

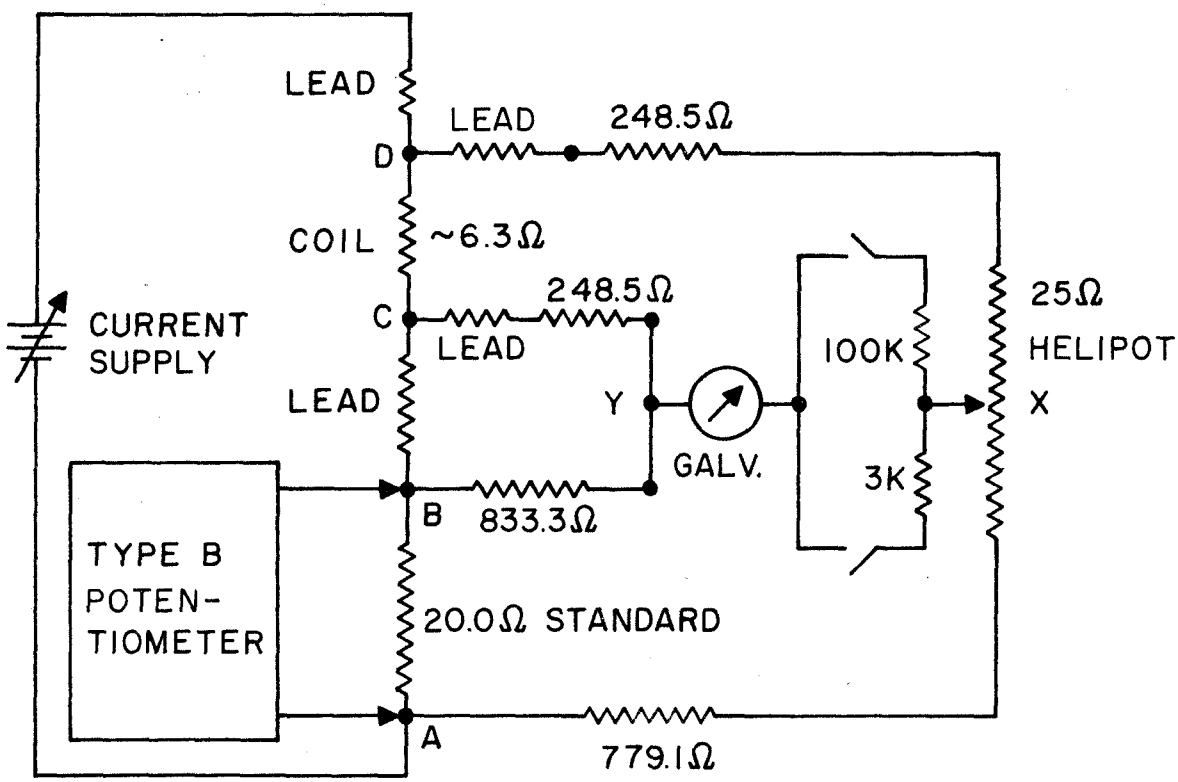

KELVIN BRIDGE CIRCUIT

Figure 32(a): Illustration of the definitions of the various energies and geometrical quantities involved in the passage of reacting particles into and out of a thick target. See text pp. 63 f. (b): The region of integration R in the spectrometer resolution window in the case where the spectrometer transmission function W is a simple rectangular window in E_{20} and θ. The line $s = 0$ corresponds to the target surface. (c): The yield resulting from the assumption of a rectangular spectrometer resolution window and negligible variation of reaction cross section and effective stopping power with energy and angle. The yield is shown for the case where the spectrometer energy E_f is held fixed and the bombarding energy E_{1B} is varied. The resolutions a and b are determined by the spectrometer constants and the reaction kinematics. See text pp. 70 f. (d): The yield resulting from the inclusion of first order variations of cross section and stopping powers with energy. Note that the curve passes below the $Y_o/2$ point on the Y axis; this is due to the correction terms derived in the text. This profile is drawn for the case where the beam energy E_{1B} is fixed and the spectrometer setting E_f varied. See text p. 80.

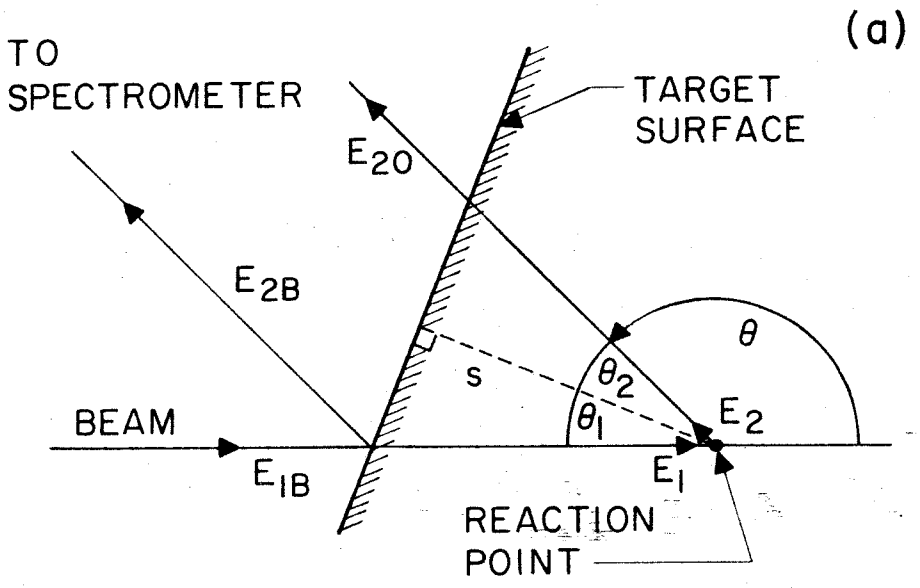
(a)
TO
SPECTROMETER
TARGET
SURFACE
E_{20}
E_{2B}
θ
s
θ_2
θ_1
BEAM
E_2
E_{1B}
E_1
REACTION
POINT

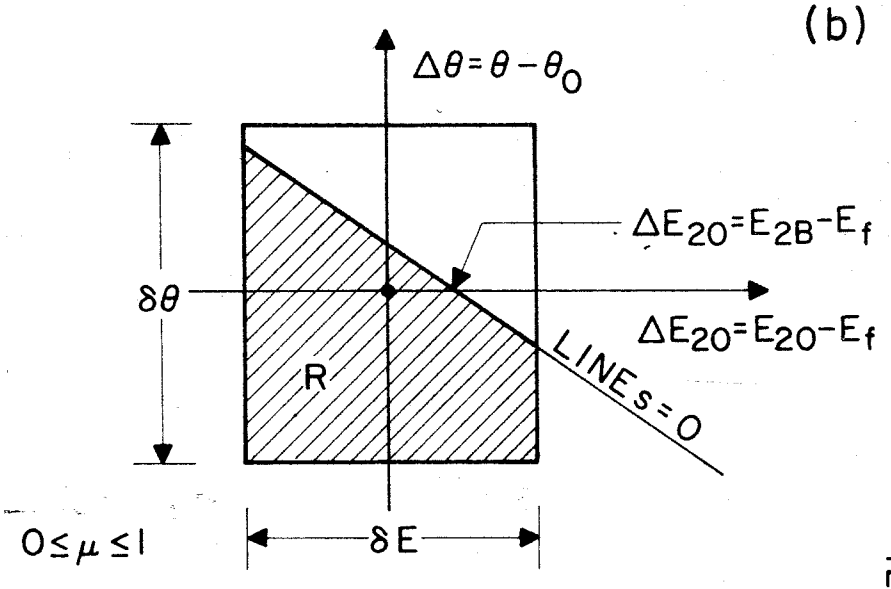
(b)
$\Delta\theta = \theta - \theta_0$
$\Delta E_{20} = E_{2B} - E_f$
$\delta\theta$
$\Delta E_{20} = E_{20} - E_f$
R
LINES = O
$0 \le \mu \le 1$
δE

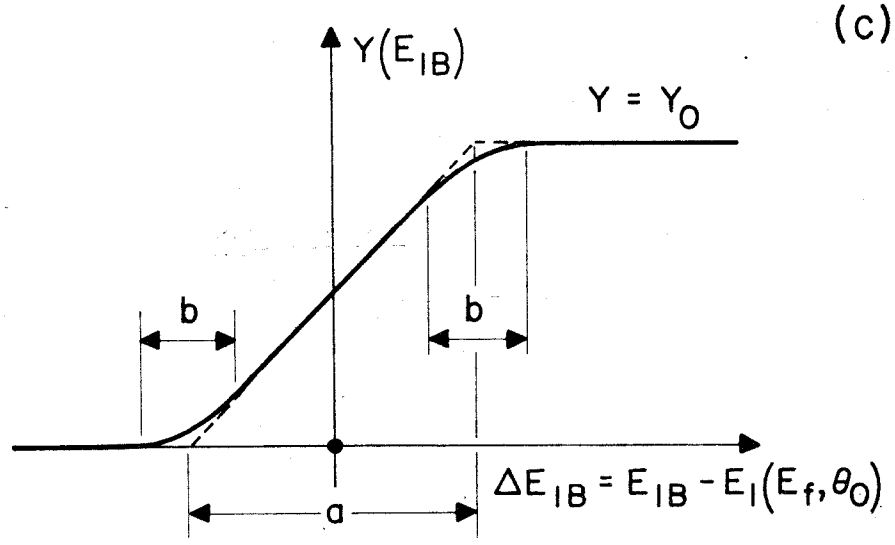
(c)
$Y(E_{1B})$
$Y = Y_0$
b
b
a
$\Delta E_{1B} = E_{1B} - E_1(E_f, \theta_0)$

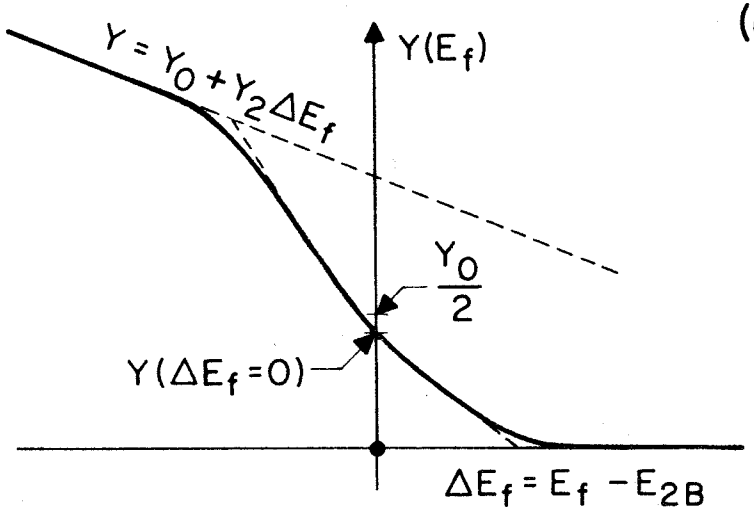
(d)
$Y = Y_0 + Y_2 \Delta E_f$
$Y(E_f)$
$\frac{Y_0}{2}$
$Y(\Delta E_f = 0)$
$\Delta E_f = E_f - E_{2B}$

Figure 33: The Rutherford scattering yield for protons on Cu at bombarding energy E_{1B} = 800 kev and laboratory angle $\theta_o = 156^o52'$, showing the theoretical fit to the plateau given by the treatment of Brown, et al. (27), (dashed curve) and by the present theory (full curve). Both curves are normalized to the point indicated by a cross. See text pp. 82 f.

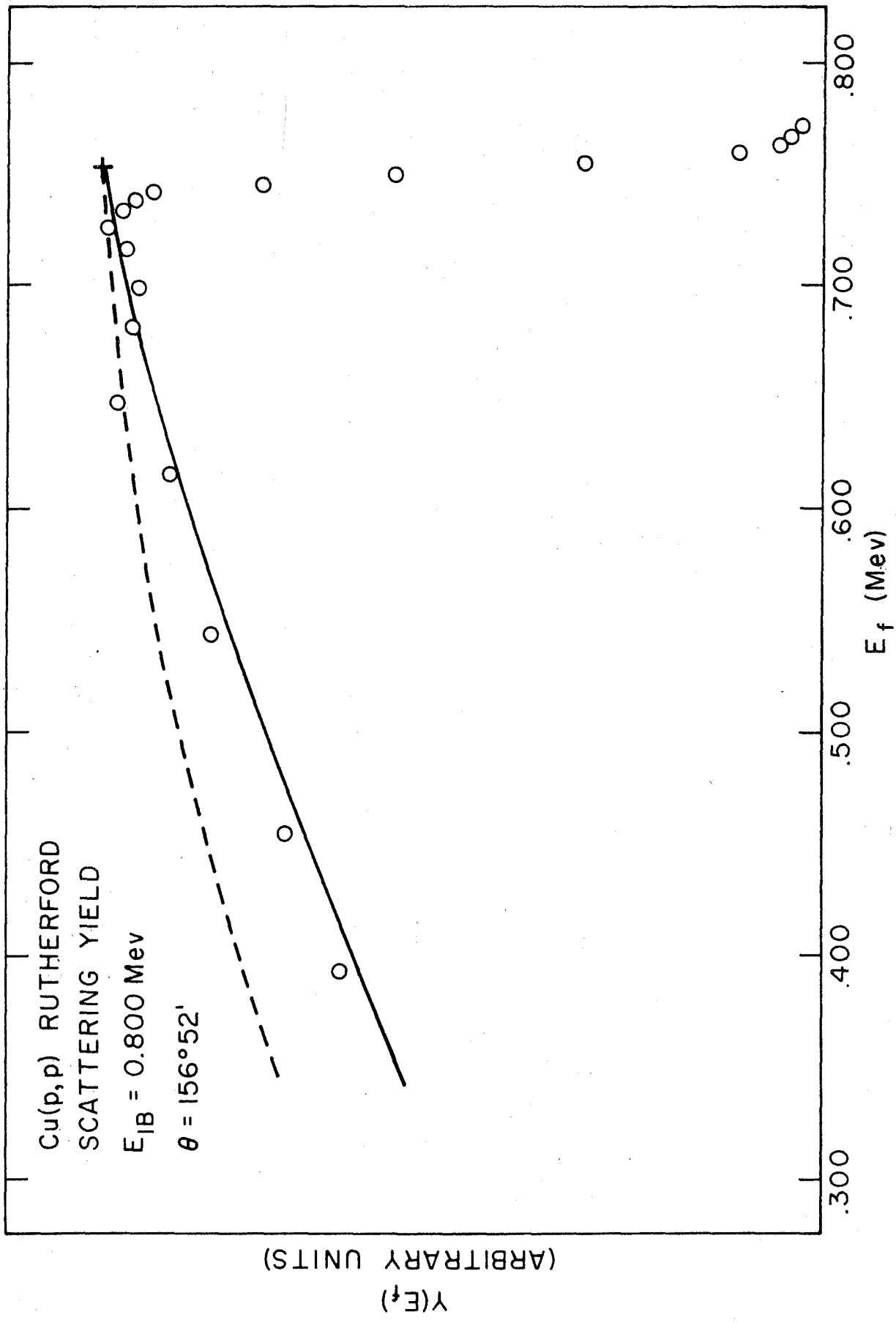
Cu(p,p) RUTHERFORD
SCATTERING YIELD
E_{IB} = 0.800 Mev
θ = 156°52'
.300
.400
.500
.600
.700
.800
E_f (Mev)
Y(E_f)
(ARBITRARY UNITS)

REFERENCES

1. R. P. Feynman and M. Gell-Man, Phys. Rev. 109, 193 (1958).

2. M. Gell-Mann, Phys. Rev. 111, 362 (1958).

3. R. E. Behrends, R. J. Finkelstein, and A. Sirlin, Phys. Rev. 101, 866 (1956).

4. S. M. Berman, Phys. Rev. 112, 267 (1958).

5. T. Kinoshita and A. Sirlin, Phys. Rev. 113, 1652 (1959).

6. L. Durand, III, L. F. Landowitz, and R. B. Marr, Phys. Rev. Letters 4, 620 (1960).

7. R. A. Reiter, T. A. Romanowski, R. B. Sutton, and B. G. Chidley, Phys. Rev. Letters 5, 22 (1960).

8. V. L. Telegdi, R. A. Swanson, R. A. Lundy, and D. D. Yovanovitch, quoted in references 6 and 7 above.

9. The three recent muon mass measurements are as follows:

   J. Lathrop, R. A. Lundy, S. Penman, V. L. Telegdi, R. Winston, D. D. Yovanovitch, and A. J. Bearden, Nuovo cimento 17, 114 (1960), giving $m_\mu = (206.76 \pm 0.03) m_e$;

   S. Devons, G. Gidal, L. M. Lederman, and G. Shapiro, Phys. Rev. Letters 5, 330 (1960), giving $m_\mu = (206.78 \pm 0.03) m_e$; and

   G. Charpak, F. J. M. Farley, R. L. Garwin, T. Muller, J. C. Sens, V. L. Telegdi, and A. Zichichi, Phys. Rev. Letters 6, 128 (1961), giving $m_\mu = (206.77 \pm 0.01) m_e$.

   The first two experiments are critical μ-mesic X-ray absorption experiments of the type described by S. Koslov, V. Fitch, and J. Rainwater, Phys. Rev. 95, 291 (1954). The third value results from a verification of the quantum electrodynamic g-factor for the muon by a technique similar to the recent electron experiment of A. A. Schupp, R. W. Pidd, and H. R. Crane, Phys. Rev. 121, 1 (1961). This result was combined with the muon magnetic moment measurement of R. L. Garwin, D. P. Hutchinson, S. Penman, and G. Shapiro, Phys. Rev. 118, 271 (1960), to get the muon mass. It is worth noting that the relations governing the various types of magnetic moment and g-factor experiments are derived from the classical covariant equations of motion in a brief but comprehensive note by V. Bargmann, L. Michel, and V. L. Telegdi, Phys. Rev. Letters 2, 435 (1959).

10. J. B. Gerhart, Phys. Rev. 95, 288 (1954).

11. J. R. Penning and F. H. Schmidt, Phys. Rev. 94, 779A (1954).

12. D. A. Bromley, E. Almqvist, H. E. Gove, A. E. Litherland, E. B. Paul, and A. J. Ferguson, Phys. Rev. 105, 957 (1957).

13. J. Mattauch, L. Waldmann, R. Bieri, and F. Everling, Z. Naturforsch. 11a, 525 (1956).

14. C. K. Bockelman, C. P. Browne, W. W. Buechner, and A. Sperduto, Phys. Rev. 92, 665 (1953).

15. J. W. Butler, Bull. Am. Phys. Soc. 1, 94 (1956).

16. R. O. Bondelid, J. W. Butler, C. A. Kennedy, and A. del Callar, NRL Quarterly on Nuclear Science and Technology, January, 1960 (unpublished), p. 7.

17. J. W. Butler and R. O. Bondelid, Phys. Rev. 121, 1770 (1961).

18. F. Ajzenberg-Selove and T. Lauritsen, Nuclear Phys. 11, 1 (1959).

19. R. K. Bardin, C. A. Barnes, W. A. Fowler, and P. A. Seeger, Phys. Rev. Letters 5, 323 (1960).

20. F. Everling, L. A. König, J. H. E. Mattauch, and A. H. Wapstra, Nuclear Phys. 18, 529 (1960).

21. E. R. Cohen, J. W. M. DuMond, T. W. Layton, and J. S. Rollett, Revs. Modern Phys. 27, 363 (1955).

22. R. O. Bondelid, J. W. Butler, C. A. Kennedy, and A. del Callar, Phys. Rev. 120, 887 (1960).

23. R. Sherr, J. B. Gerhart, H. Horie, and W. F. Hornyak, Phys. Rev. 100, 945 (1955).

24. J. B. Marion, University of Maryland Physics Department Technical Report 184, July 1960 (unpublished).

25. W. A. Fowler, C. C. Lauritsen, and T. Lauritsen, Rev. Sci. Inst. 18, 818 (1947).

26. C. W. Li, thesis, California Institute of Technology, 1951 (unpublished).

27. A. B. Brown, C. W. Snyder, W. A. Fowler, and C. C. Lauritsen, Phys. Rev. 82, 159 (1951).

28. See, e. g., D. F. Herring, R. A. Douglas, E. A. Silverstein, and R. Chiba, Phys. Rev. 100, 1239A (1955).

29. R. O. Bondelid, J. W. Butler, and C. A. Kennedy, Bull. Am. Phys. Soc. 2, 381 (1957) See also R. O. Bondelid and C. A. Kennedy, U. S. Naval Research Laboratory Report 5083 (1958) (unpublished).

30. S. L. Andersen, K. Gjötterud, T. Holtebekk, and O. Lönsjö, Nuclear Phys. 7, 384 (1958).

31. P. F. Dahl, D. G. Costello, and W. L. Walters, Nuclear Phys. 21, 106 (1960). See also D. G. Costello, W. L. Walters, and R. G. Herb, Bull. Am. Phys. Soc. 6, 250 (1961).

32. K. H. Sun, P. R. Malmberg, and F. A. Pecjak, Nucleonics 14, 46 (July 1956).

33. H. W. Newson, R. M. Williamson, K. W. Jones, J. H. Gibbons, and H. Marshak, Phys. Rev. 108, 1294 (1957).

34. R. L. Macklin and J. H. Gibbons, Phys. Rev. 109, 105 (1958).

35. W. A. Fowler, C. C. Lauritsen, and T. Lauritsen, Revs. Modern Phys. 20, 236 (1948).

36. Tables for the Analysis of Beta Spectra, National Bureau of Standards Applied Mathematics Series No. 13 (U. S. Government Printing Office, Washington, D. C., 1952).

37. D. L. Hendrie and J. B. Gerhart, Phys. Rev. 121, 846 (1961).

38. R. M. Sanders, Phys. Rev. 104, 1434 (1956).

39. R. Sherr, H. R. Muether, and M. G. White, Phys. Rev. 75, 282 (1949).

40. W. M. MacDonald, Phys. Rev. 110, 1420 (1958).

41. E. J. Konopinski, Ann. Rev. Nuclear Science 9, 99 (1959).

42. T. D. Lee, and C. N. Yang, Phys. Rev. 108, 1611 (1957). See also further references given in the review article by L. Okun', Ann. Rev. Nuclear Science 9, 61 (1959).

43. S. Oneda and J. C. Pati, Phys. Rev. Letters 2, 125 (1959).

44. K. R. Symon, quoted in: B. Rossi, High Energy Particles, pp. 29 ff., Prentice-Hall, New York (1952).

45. H. A. Bethe and Julius Ashkin, Passage of Heavy Particles Through Matter; in Experimental Nuclear Physics, E. Segre, ed., Vol. I, pp. 166-252. John Wiley and Sons, New York, (1953).

46. W. Whaling, The Energy Loss of Charged Particles in Matter; in Handbuch der Physik, S. Flügge, ed., Bd. XXXIV, pp. 193 ff., Springer Verlag, Berlin (1958).

47. R. F. Christy, Nuclear Phys. 22, 301 (1961).